Theoretical study for identifying unconventional superconductivity through vortex core bound states

Theoretical study for identifying unconventional superconductivity through vortex core bound states

Yoichi Higashi

February 2015

Doctoral Thesis at Osaka Prefecture University

Abstract

Superconductivity with the internal degree of freedom is called unconventional or exotic super-conductivity. The present dissertation discusses how to identify the unconventional pairing state through low energy excited states within a quantized vortex in superconductors. The following topics are focused on: (i) the phase structure of anisotropic Cooper pairing states and (ii) the effect of the spin-orbit coupling on the electronic structure of a vortex core.

The phase structure of the Cooper pair comes from remaining its relative angular momentum. So it is crucial to probe the phase of the Cooper pair in order to discriminate unconventional superconductors from conventional ones. The flux-flow resistivity can be a potentially effective probe to identify the phase structure of the Cooper pair, since it is dominated by the phase-sensitive quantity. The flux-flow resistivity is estimated by measuring the microwave surface impedance, which is applicable for more various materials than the existing phase-sensitive test fabricating a Josephson junction. This is the great advantage of the phase-sensitive test proposed in the present dissertation. The flux-flow resistivity is calculated with use of the quasiclassical Green's function method and the Kramer-Pesch approximation. The in-plane field angle depen-dence of the flux-flow resistivity shows contrasting behavior between a line node s-wave pair and a d-wave one, directly reflecting the internal phase structure of the Cooper pairs. This findings clearly indicate that measuring the flux-flow resistivity with changing the magnetic field direction within the plane can be a new experimental probe to identify the pairing symmetry including the phase structure of the Cooper pair.

Exotic superconducting states arising in noncentrosymmetric systems are based on the anti-symmetric spin-orbit coupling. One of the notable features of noncentrosymmetric superconduc-tors is the mixing of the Cooper pair wave function with the different parity. The effect of the spin-orbit coupling on the vortex core structure is mainly investigated. The numerical calculation reveals that the impurity effect on the local density of states depends on the spin-orbit coupling strength α in the presence of the p-wave component, whereas it is independent of the spin-orbit coupling in the case of the s-wave pair. The key factor of α dependent impurity scattering is the interband impurity scattering between the Fermi surfaces split due to the anti-symmetric spin-orbit coupling.

The vortex core structure in locally noncentrosymmetric superconductors is also investigated numerically. Due to the spatially inhomogeneous anti-symmetric spin-orbit coupling reflecting the local noncentrosymmetricity, novel superconducting phases stabilize under a magnetic field. Especially, an inhomogeneous superconducting state called the pair-density wave (PDW) state in multilayered systems is focused on in the present dissertation. The self-consistent quasiclas-sical calculations clarify that the vortex core structure changes drastically in the vicinity of the BCS/PDW phase transition. The difference of the core structure comes from whether or not there is the phase difference of the order parameter between the layers.

Finally, the excitation spectra and the wave functions of the vortex and the edge bound states in the bilayer Rashba superconductor are calculated numerically. The PDW state in bilayer systems undergo the phase transition into the topologically non-trivial phase when a magnetic field exceeds the critical values, and then the zero energy vortex and the edge bound states appear.

Acknowledgments

List of Papers

- "Analysis of field-angle dependent specific heat in unconventional superconductors: a comparison between Doppler-shift method and Kramer-Pesch approximation",
N. Hayashi, Y. Nagai, and Y. Higashi,
Physica C **470**, S865-S867 (2010).

- "Field-angle dependence of the quasiparticle scattering inside a vortex core in unconventional superconductors",
Y. Higashi, Y. Nagai, M. Machida, and N. Hayashi,
Physica C **471**, 828-830 (2011).

- "Phase-Sensitive Flux-Flow resistivity in Unconventional Superconductors",
Y. Higashi, Y. Nagai, M. Machida, and N. Hayashi,
Journal of Physics: Conference Series **400**, 022025 (2012).

- "Effect of uniaxially anisotropic Fermi surface on the quasiparticle scattering inside a vortex core in unconventional superconductors",
Y. Higashi, Y. Nagai, M. Machida, and N. Hayashi,
Physica C **484**, 97-99 (2013).

- "Effect of Born and unitary impurity scattering on the Kramer-Pesch shrinkage of a vortex core in an s-wave superconductor",
N. Hayashi, Y. Higashi, N. Nakai, and H. Suematsu,
Physica C **484**, 69-73 (2013).

- "Effect of anisotropic Fermi surface on the flux-flow resistivity under rotating magnetic field",
Y. Higashi, Y. Nagai, M. Machida, and N. Hayashi,
Physics Procedia **45**, 137-140 (2013).

- "Field-angle resolved flux-flow resistivity as a phase-sensitive probe of unconventional Cooper pairing",
Y. Higashi, Y. Nagai, M. Machida, and N. Hayashi,
Physical Review B **88**, 224511 (2013).

- "Impurity Effect on the Local Density of States around a Vortex in Noncentrosymmetric Superconductors",
Y. Higashi, Y. Nagai, and N. Hayashi,
JPS Conference Proceedings **3**, 015003 (2014).

- "Vortex Core Structure in Multilayered Rashba Superconductors",
Y. Higashi, Y. Nagai, T. Yoshida, and Y. Yanase,
Journal of Physics: Conference Series **568**, 022018 (2014).

- "Excitation spectra and wave functions of quasiparticle bound states in bilayer Rashba superconductors",
Y. Higashi, Y. Nagai, T. Yoshida, M. Kato, and Y. Yanase,
Submitted to Physica C.

- "Robust zero-energy bound states around a pair-density-wave vortex core in locally non-centrosymmetric superconductors",
  Y. Higashi, Y. Nagai, T. Yoshida, Y. Masaki, and Y. Yanase,
  Submitted to Physical Review B.

Contents

Chapter 1

General Introduction

Superconductivity occurs with the quasiparticle states forming the Cooper pairs. The Cooper pair wave function may have the additional symmetry breaking other than $U(1)$ gauge symmetry breaking. The additional symmetry breaking of superconductivity reflects the remaining internal degree of freedom of the Cooper pair such as the relative angular momentum, the total spin and center of mass momentum. Such superconductivity is called *unconventional* or *exotic* superconductivity [1, 2]. Fist of all, I describe the vortex bound states. Then, I consider the case in which the Cooper pair wave function has the relative angular momentum (i.e., anisotropic superconductivity). We also consider the case in which the total spin of the Cooper pair is remaining in the context of noncentrosymmetric superconductivity where the spatial parity of the Cooper pair wave function is broken. Then, I give the background and the motivation of the dissertation.

1.1   Vortex core bound states

In type-II superconductors, a magnetic flux penetrates into a superconductor as a *quantized* magnetic flux above the lower critical field. Around a quantized magnetic flux, supercurrent flows. The supercurrent is proportional to the phase gradient of superconducting order parameter. The order parameter of superconductivity is expressed as a complex scalar field, $\psi = |\psi| \exp(i\theta)$. ψ is considered as the wave function of Cooper pairs, which are introduced later, and $|\psi|^2$ is proportional to the superconducting electron density. The quantized magnetic flux with the vortex rotational superflow is called a *vortex*. At the center of the vortex, the order parameter phase is not defined and the order parameter amplitude becomes zero. Near the vortex center, i.e., at the core of the vortex, the order parameter is locally suppressed and recovers its amplitude in the bulk. So the order parameter varies spatially $\psi(r) = |\psi(r)| \exp(i\theta \cdot n)$. The spatial variation scale of the order parameter is estimated by the Ginzburg-Landau (GL) equation, which is of the order of the coherence length $\xi = \hbar v_{\mathrm{F}} / \Delta_\infty$. Δ_∞ is the bulk gap energy and v_{F} is the Fermi velocity. Usually singly quantized vortices ($n = 1$) is the most stable.

In the presence of vortices, there are low energy excitation states around them. The GL theory is good at treating spatially inhomogeneous systems, but cannot treat excitations. For purpose of investigating the excitations around vortices, one has to use the theory capable to treat the excitations. Caroli *et al.* discussed the low energy excitations around a vortex in an *s*-wave superconductor for the first time, solving the Bogoliubov-de Gennes equation analytically [3]. They obtained the low energy excitation spectra proportional to angular quantum number and the inter-level spacing of the excitation spectra $\omega_0 \sim \Delta_\infty^2 / E_{\mathrm{F}}$. E_{F} is the Fermi energy. The same formula for excitation spectra was obtained also by Kramer and Pesch using the quasiclassical theory [4]. The lowest bound states level ω_0 is much smaller than the superconducting transition temperature T_{c}. So there are excitations from the superconducting condensates even at low temperature $\sim (\Delta_\infty / E_{\mathrm{F}}) T_{\mathrm{c}}$.

The first spectroscopic experiment on electronic states at the vortex core was conducted on NbSe$_2$ by Hess *et al.* in 1989, using the scanning tunneling microscopy/spectroscopy (STM/STS)

[5]. They succeeded to observe the large peak in the differential conductance (tunneling conductance) in the vicinity of the vortex center at zero energy. This peak is suppressed away from the vortex. The peak of the zero energy differential conductance stems from localized excitations at the vortex core, i.e., vortex core bound states. After that, the comprehensive numerical study on the vortex bound states was conducted by Gygi and Schlüter [6]. The fundamental properties of a vortex in an isotropic s-wave superconductor are covered in their paper. They showed the numerical result of the tunneling conductance explaining well the STM/STS experiment, namely they reproduced the split zero energy peak into the two ridge lines of the vortex bound states reaching the gap edges in the bulk. However, the origin of the star-shaped STM images observed in NbSe$_2$ [7] was still unclear. Hayashi *et al.* revealed the origin of the anisotropic vortex bound states taking into account the anisotropy of the superconducting order parameter [8, 9]. They explained in detail the concept of *quasiparticle trajectory* in the quasiclassical picture [9].

It is difficult to capture the physical picture of the vortex bound states. As mentioned above, the low energy excitation energy at the vortex core is proportional to the angular quantum number. This property of the vortex core bound states can be understood as a circular motion of quasiparticles about a vortex line in the quasiclassical picture. Besides, the zero energy peak of the vortex bound states splits into the two branches evolving to higher energy and finally reaching the gap edges as approaching to the bulk, which is called the spectral evolution. This means that the quasiparticles running around a vortex line have the higher energy as the radius of quasiparticle rotation gets larger. The quasiparticle rotating with its radius $\sim \xi$ from the vortex center has the energy $\sim (\hbar^2/2m)(1/\xi)^2 \sim \omega_0$. The angular frequency of the rotation is estimated as ω_0. If there is an anisotropy or gap nodes of the order parameter, the rotating quasiparticles around the core run away from the core in the direction of the nodes in momentum space [9, 10]. The gap nodes are the zeros of the superconducting gap (the absolute value of the order parameter) in the momentum space.

1.2 Anisotropic superconductivity in spatially isotropic systems

1.2.1 Cooper instability

First, we consider superconductivity or superfluidity in an isotropic system such as superfluid ^{3}He. In this situation, we can neglect the anisotropy of the crystal lattice. Single particle states are occupied up to the Fermi energy in the ground states of free electron gases. However, in the presence of an attractive interaction between at least one electron pair in momentum space, no matter how weak it is, the ground state becomes unstable and the electron system goes to more stable state. This is called the Cooper instability.

We start with the Schrödinger equation for the two electrons:

$$-\frac{\hbar^2}{2m}\left(\boldsymbol{\nabla}_1^2 + \boldsymbol{\nabla}_2^2\right)\psi_{\alpha\beta}\left(\boldsymbol{r}_1, \boldsymbol{r}_2\right) + V\left(\boldsymbol{r}_1 - \boldsymbol{r}_2\right)\psi_{\alpha\beta}\left(\boldsymbol{r}_1, \boldsymbol{r}_2\right) = \left(E + \frac{\hbar^2 k_{\mathrm{F}}^2}{2m} \times 2\right)\psi_{\alpha\beta}\left(\boldsymbol{r}_1, \boldsymbol{r}_2\right), \quad (1.1)$$

where E is the energy of an electron pair measured from the energy of two electrons at the Fermi level. The pair electron wave function is composed of the orbital wave function with respect to the center of mass coordinate and the relative one, and the spin wave function. Assuming the translational symmetry of the system, the center of mass wave function becomes plane wave. Then, the pair electron wave function is written as

$$\psi_{\alpha\beta}\left(\boldsymbol{r}_1, \boldsymbol{r}_2\right) = e^{i\boldsymbol{K}\cdot\boldsymbol{R}}\phi(\boldsymbol{r}_1 - \boldsymbol{r}_2)\chi(\alpha, \beta), \quad (1.2)$$

where $\boldsymbol{P} = \hbar\boldsymbol{K}$ and $\boldsymbol{R}$ are the center of mass momentum and coordinate, respectively. We assume $\boldsymbol{P} = \boldsymbol{0}$. Using the relative wave vector $\bar{\boldsymbol{k}}$, the two electron wave function is expressed as

$$\psi_{\alpha\beta}(\bar{\boldsymbol{r}}) = (2\pi\hbar)^{-3}\int d\bar{\boldsymbol{k}}\, e^{i\bar{\boldsymbol{k}}\cdot\bar{\boldsymbol{r}}}\phi(\bar{\boldsymbol{k}})\chi(\alpha, \beta). \quad (1.3)$$

[In sufficiently large systems, the summation converts into the integral over the continuous wave vector]. Here $\bar{r} = r_1 - r_2$ is the relative coordinate. Substitute Eq. (1.3) into Eq. (1.1). Then, multiplying $\exp[-i\bar{k}' \cdot \bar{r}]$ both sides and integrating over $\bar{r}$, we obtain

$$\frac{\hbar^2 |\bar{k}|^2}{m}\phi(\bar{k}) + (2\pi\hbar)^{-3}\int d\bar{k}' V(\bar{k} - \bar{k}')\phi(\bar{k}') = \left(E + \frac{\hbar^2 k_{\mathrm{F}}^2}{m}\right)\phi(\bar{k}). \tag{1.4}$$

In isotropic systems, we can expand the pairing interaction as

$$V(\bar{k} - \bar{k}') = \sum_{l=0}^{\infty} V_l(\bar{k}, \bar{k}') \sum_{m=-l}^{l} 4\pi Y_{lm}(\hat{\bar{k}})Y_{lm}^*(\hat{\bar{k}}') \tag{1.5}$$

Here we assume

$$V_l(\bar{k}, \bar{k}') = \begin{cases} -V_l & (\varepsilon_{\mathrm{F}} - \varepsilon_{\mathrm{c}} < \varepsilon(\bar{k}) < \varepsilon_{\mathrm{F}} + \varepsilon_{\mathrm{c}}, \\ & \quad \varepsilon_{\mathrm{F}} - \varepsilon_{\mathrm{c}} < \varepsilon(\bar{k}') < \varepsilon_{\mathrm{F}} + \varepsilon_{\mathrm{c}}), \\ 0 & (\text{otherwise}), \end{cases} \tag{1.6}$$

where $\varepsilon(\bar{k}) = \hbar^2 \bar{k}^2/2m$ and ε_{c} is the cutoff energy. Let us replace the integral over the wave vector in Eq. (1.4) by the integral over the quasiparticle energy $\xi_{\bar{k}} = \varepsilon(\bar{k}) - \varepsilon_{\mathrm{F}}$ and the angles, that is,

$$(2\pi\hbar)^{-3}\int d\bar{k}' \rightarrow N_{\mathrm{F}}\int d\xi'_{\bar{k}}\int \frac{d\Omega_{\bar{k}'}}{4\pi}. \tag{1.7}$$

N_{F} is the density of states at the Fermi level in the normal states per spin. $\int d\Omega_{\bar{k}'} \equiv \int_0^{2\pi} d\phi_{\bar{k}'}\int_0^{\pi} d\theta_{\bar{k}'}\sin\theta_{\bar{k}'}$ for isotropic three dimensional systems. Expanding the orbital wave function as

$$\phi(\bar{k}') = \sum_{l'}\sum_{m'=-l'}^{l'}\phi_{l'm'}(\bar{k}')Y_{l'm'}(\hat{\bar{k}}') \tag{1.8}$$

and substituting it into Eq. (1.4), we have the following Schrödinger equation for each quantum number of the relative orbital angular momentum l.

$$\left\{\frac{\hbar^2}{m}(|\bar{k}|^2 - k_{\mathrm{F}}) - E_l\right\}\phi_l(\bar{k}) - N_{\mathrm{F}}V_l\int_0^{\varepsilon_{\mathrm{c}}} d\xi_{\bar{k}'}\phi_l(\bar{k}) = 0, \tag{1.9}$$

where we used the orthonormality for spherical harmonics. Finally we obtain the eigen energy (two electrons bound state energy) for the weak coupling limit $N_{\mathrm{F}}V_l \ll 1$,

$$E_l \approx -2\varepsilon_{\mathrm{c}}e^{-2/(N_{\mathrm{F}}V_l)}(< 0). \tag{1.10}$$

When attractive interaction acts between the electrons on the Fermi surface, the two electrons state bound energy becomes lower than $2\varepsilon_{\mathrm{F}}$. The eigen wave function of the orbital part is

$$\phi_l(\bar{k}) = \frac{N_{\mathrm{F}}V_l C}{2\xi(\bar{k}) - E_l}, \tag{1.11}$$

where C is the dimensionless constant. In the presence of an attractive interaction between two electrons, the bound states is formed with respect to the relative orbital angular momentum l. For non-zero l, the bound electron pair has the orbital angular momentum l.

1.2.2 Anisotropic Cooper pair

In the superconducting ground state, a macroscopic number of electrons condensate into the paired states in momentum space. However, we can apply the similar analysis discussed above to superconductivity as many body problem using the second quantization for many electron systems (see the text book of superconductivity [11, 12] or superfluidity [13]). Investigating the

pair condensed state with use of the mean field approximation, following physical quantity is introduced:

$$\Delta_{ss'}(\bar{\boldsymbol{k}}) = -\sum_{\bar{\boldsymbol{k}}'} V(\bar{\boldsymbol{k}}, \bar{\boldsymbol{k}}') \left\langle c_{\bar{\boldsymbol{k}}'s} c_{-\bar{\boldsymbol{k}}'s'} \right\rangle. \tag{1.12}$$

This is the superconducting order parameter. At finite temperature, we have

$$\Delta(\bar{\boldsymbol{k}}) = -\sum_{\bar{\boldsymbol{k}}'} V(\bar{\boldsymbol{k}}, \bar{\boldsymbol{k}}') \frac{\Delta(\bar{\boldsymbol{k}}')}{2E(\bar{\boldsymbol{k}}')} \tanh\left(\frac{E(\bar{\boldsymbol{k}}')}{2k_{\mathrm{B}}T}\right). \tag{1.13}$$

This equation is called the gap equation. $E(\bar{\boldsymbol{k}}) = \sqrt{\xi^2(\bar{\boldsymbol{k}}) + |\Delta(\bar{\boldsymbol{k}})|^2}$ is the excitation energy of a quasiparticle in the superconducting state. $|\Delta(\bar{\boldsymbol{k}})|$ is the excitation energy gap of the quasiparticle relative to the chemical potential, which can be understood from $E(\bar{\boldsymbol{k}}) \geq |\Delta(\bar{\boldsymbol{k}})|$. This is a physical meaning of the order parameter amplitude. The phase of the order parameter is also detectable by phase-sensitive probes.

Assuming the translational symmetry, the pairing interaction depends only on $\bar{\boldsymbol{k}} - \bar{\boldsymbol{k}}'$. For isotropic systems, in the same way as the two electron bound state, we expand the pairing interaction and substitute it into the gap equation. Then we find that $\Delta(\bar{\boldsymbol{k}}) = \Delta_{lm} Y_{lm}(\hat{\bar{\boldsymbol{k}}})$ is the solution of the gap equation (1.13). The transition temperature is calculated as

$$T_{\mathrm{c}}^l = \frac{1.13\varepsilon_{\mathrm{c}}}{k_{\mathrm{B}}} e^{-1/(N_{\mathrm{F}}V_l)}. \tag{1.14}$$

The transition temperature does not depend on the magnetic quantum number m. Then T_{c}^l has the $m = 2l + 1$-fold degeneracy. Correspondingly, the order parameter is also $2l + 1$-fold degenerated. These consequences are due to the rotational symmetry of a continuous system.

In isotropic system where rotational symmetry is maintained, the order parameter symmetry of anisotropic superconductivity is classified by the quantum number of the relative angular momentum of the Cooper pair l. The superconductivity with $l = 0$ corresponds to an s-wave one and that with $l \geq 2$ is anisotropic one. For example, $l = 1$ corresponds to p-wave superconductivity and $l = 2$ corresponds to d-wave one. In isotropic systems, we cannot distinguish the orbital wave functions $Y_{lm}(\hat{\bar{\boldsymbol{k}}})$ with different magnetic quantum numbers m.

However, in the presence of the anisotropy of the background, the orbital wave functions with the same absolute value of the magnetic quantum number are mixed [2]. For instance, the orbital symmetry of the $d_{x^2-y^2}$-wave pair is $Y_{22}(\hat{\bar{\boldsymbol{k}}}) + Y_{2-2}(\hat{\bar{\boldsymbol{k}}}) \propto [\exp(2i\phi_k) + \exp(-2i\phi_k)]/2 = \cos(2\phi_k)$. Strictly speaking, the real crystal lattice lacks the rotational symmetry and then the relative angular momentum of the Cooper pair is not defined. Thus we need to classify the symmetry of the orbital wave function of the Cooper pair by means of the irreducible representation of the point group [1].

1.3 Superconductivity in noncentrosymmetric systems

In this section, we consider superconductivity in the system lacking in an inversion center.

1.3.1 Anti-symmetric spin-orbit coupling

We start with the interaction between valence electron spin and electrostatic potential $\phi(r)$ in an atomic nucleus, which is called the LS coupling. We consider the orbital motion of a valence electron with the velocity $\boldsymbol{v}$, suffering the electric field $\boldsymbol{E} = -\boldsymbol{\nabla}\phi(\boldsymbol{r})$. The atomic nucleus runs with the relative velocity $-\boldsymbol{v}$ seen from the coordinate system moving with the electron. Thus, the magnetic field $\boldsymbol{H} = -(1/c)\boldsymbol{v} \times \boldsymbol{E}$ appears at the position of the electron. This magnetic field couples the electron spin. The interaction energy is given by

$$-\mu_{\mathrm{s}} \cdot \boldsymbol{H} = -\frac{g\hbar e}{2mc^2} [\boldsymbol{v} \times \boldsymbol{E}] \cdot \boldsymbol{S}, \tag{1.15}$$

where the mass of an electron m, the absolute value of the electron charge $e(>0)$, the velocity of light c. The electronic g-factor is given by $g = 2.0023$. By the relativistic treatment with the Dirac equation, one can obtain a factor 2 smaller value. Thus, the LS coupling is obtained as

$$\mathscr{H}_{\mathrm{LS}} = -\frac{\hbar e}{2m^2c^2}[\boldsymbol{p} \times \boldsymbol{E}] \cdot \boldsymbol{S}. \tag{1.16}$$

Here we used $\boldsymbol{p} = m\boldsymbol{v}$. If we view the momentum as the crystal momentum of the electron ($\boldsymbol{p} = \hbar\boldsymbol{k}$) and consider the electric field parallel to z axis ($\boldsymbol{E} = E\hat{\boldsymbol{z}}$), we have [14, 15]

$$\mathscr{H}_{\mathrm{LS}} = -\frac{\hbar^2 eE}{2m^2c^2}\boldsymbol{g}(\boldsymbol{k}) \cdot \boldsymbol{S}. \tag{1.17}$$

$\boldsymbol{g}(\boldsymbol{k}) = (k_y, -k_x, 0)$ is the Rashba type orbital vector. The expectation value of the electric field ($\boldsymbol{E} \parallel \hat{\boldsymbol{z}}$) for the wave function $\psi_{\boldsymbol{k}}(\boldsymbol{r}) = \exp(i\boldsymbol{k} \cdot \boldsymbol{r})$ is

$$
\begin{aligned}
-\int_{\mathrm{u.c.}} d\boldsymbol{r}\,\psi_{\boldsymbol{k}}^*(\boldsymbol{r})\,[\boldsymbol{\nabla}\phi(\boldsymbol{r})]_z\,\psi_{\boldsymbol{k}}(\boldsymbol{r}) &= -\int_{\mathrm{u.c.}} d\boldsymbol{r}\,\frac{\partial}{\partial z}\phi(\boldsymbol{r}) \\
&= -\int dx \int dy \int_{-c/2}^{c/2} dz\,\frac{\partial}{\partial z}\phi(\boldsymbol{r}) \\
&= -\int dx \int dy\,[\phi(x, y, c/2) - \phi(x, y, -c/2)] \\
&= -\int dx \int dy\,[\phi(x, y, c/2) - \phi(-x, -y, -c/2)]. \tag{1.18}
\end{aligned}
$$

$\int_{\mathrm{u.c.}}$ denotes the integral over a unit cell. The expectation value is zero for $\phi(x, y, c/2) = \phi(-x, -y, -c/2)$ and finite for $\phi(x, y, c/2) \neq \phi(-x, -y, -c/2)$. Thus, when $\phi(\boldsymbol{r})$ has the asymmetric form lacking in an inversion center, the finite expectation value of the electric field appears in the direction of the z axis.

At the beginning of the discussion, we considered the electric field arising from electrostatic potential in atomic nucleus. At the middle of the discussion, we considered the z-axis electric field arising from the electrostatic potential asymmetry due to the noncentrosymmetricity of the crystal lattice. Besides, we took into account only the plane wave part of the wave function when calculating the expectation value of the electric field. This simplification might be justified for electrons moving away from the atomic nucleus. However, as pointed out by Yanase [15] following the discussion to derive the antisymmetric spin-orbit coupling (ASOC) [16, 14], we have to take into account the momentum of the electron instead of the crystal momentum when the electron is in the vicinity of atomic nucleus. Considering the expectation value for the Bloch wave function $\psi_{\boldsymbol{k}}(\boldsymbol{r}) = \exp(i\boldsymbol{k} \cdot \boldsymbol{r})u(\boldsymbol{r})$, Eq. (1.16) yields the following ASOC.

$$
\begin{aligned}
\mathscr{H}_{\mathrm{ASOC}} &= \frac{\hbar e}{2m^2c^2}\left[\int_{\mathrm{u.c.}} d\boldsymbol{r}\,\psi_{\boldsymbol{k}}^*(\boldsymbol{r})(\boldsymbol{p} \times \boldsymbol{\nabla}\phi(\boldsymbol{r}))\psi_{\boldsymbol{k}}(\boldsymbol{r})\right] \cdot \boldsymbol{S} \\
&= \frac{\hbar e}{2m^2c^2}\left[\int_{\mathrm{u.c.}} d\boldsymbol{r}(\boldsymbol{J}_{\boldsymbol{k}}(\boldsymbol{r}) \times \boldsymbol{\nabla}\phi(\boldsymbol{r}))\right] \cdot \boldsymbol{S}, \tag{1.19}
\end{aligned}
$$

with

$$\boldsymbol{J}_{\boldsymbol{k}}(\boldsymbol{r}) \equiv \frac{\hbar}{2mi}[\psi_{\boldsymbol{k}}^*(\boldsymbol{r})\boldsymbol{\nabla}\psi_{\boldsymbol{k}}(\boldsymbol{r}) - \psi_{\boldsymbol{k}}(\boldsymbol{r})\boldsymbol{\nabla}\psi_{\boldsymbol{k}}^*(\boldsymbol{r})]. \tag{1.20}$$

Neglecting the spatial derivative of $u_{\boldsymbol{k}}(\boldsymbol{r})$ and $u_{\boldsymbol{k}}^*(\boldsymbol{r})$, we obtain

$$\mathscr{H}_{\mathrm{ASOC}} = -\frac{\hbar^2 e}{2m^2c^2}(\boldsymbol{k} \times \boldsymbol{E}_{\mathrm{AVL.}}) \cdot \boldsymbol{S}, \tag{1.21}$$

$$\boldsymbol{E}_{\mathrm{AVL.}} \equiv \int_{\mathrm{u.c.}} d\boldsymbol{r}\,|\psi_{\boldsymbol{k}}(\boldsymbol{r})|^2 \boldsymbol{E}(\boldsymbol{r}). \tag{1.22}$$

$\boldsymbol{E}_{\mathrm{AVL}}$ is the expectation value of the electric field for the Bloch wave function $\psi_{\boldsymbol{k}}(\boldsymbol{r}) = \exp(i\boldsymbol{k} \cdot \boldsymbol{r})u(\boldsymbol{r})$. This formula estimates the value of the ASOC much larger than that in metals, which is caused by neglecting the spatial derivative of $u_{\boldsymbol{k}}(\boldsymbol{r})$ and $u_{\boldsymbol{k}}^*(\boldsymbol{r})$ [15]. The detailed derivation of the ASOC on the basis of the microscopic model is given in Ref. [15].
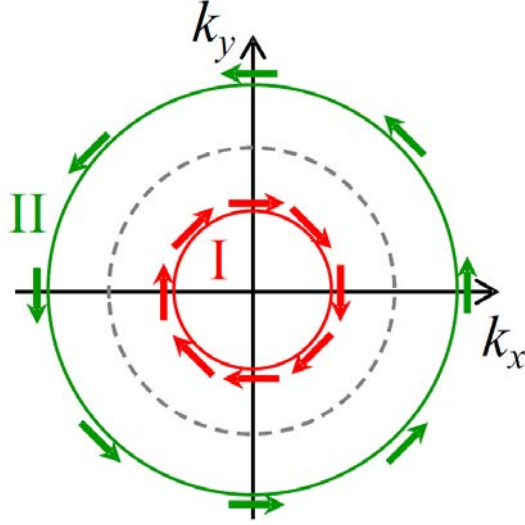
Figure 1.1: Spin structure on the split Fermi surface. The dotted circle indicates the Fermi surface in the absence of the spin-orbit coupling.

1.3.2 Spin structure on the Fermi surface

The lack of inversion symmetry is incorporated by an ASOC. The normal state Hamiltonian in the wave vector representation is

$$\mathscr{H} = \sum_{\boldsymbol{k},s} \xi(\boldsymbol{k}) c_{\boldsymbol{k}s}^{\dagger} c_{\boldsymbol{k}s} + \alpha \sum_{\boldsymbol{k},s,s'} \boldsymbol{g}(\boldsymbol{k}) \cdot \hat{\boldsymbol{\sigma}}_{ss'} c_{\boldsymbol{k}s}^{\dagger} c_{\boldsymbol{k}s'}. \tag{1.23}$$

Here, $c_{\boldsymbol{k}s}^{\dagger}$ and $c_{\boldsymbol{k}s}$ are the creation and annihilation operators for a quasiparticle with wave vector $\boldsymbol{k}$ and spin s, respectively. α is the SOC strength and $\hat{\boldsymbol{\sigma}}^{\mathrm{T}} = (\hat{\sigma}_x, \hat{\sigma}_y, \hat{\sigma}_z)$. We consider the Rashba type SOC in three dimensional systems and take the orbital vector as $\boldsymbol{g}(\boldsymbol{k}) = \sqrt{3/2}(-k_y, k_x, 0)/k_{\mathrm{F}}$. Considering the periodic system in a lattice model, the orbital vector becomes periodic to satisfy the periodicity of the Brillouin zone. This model Hamiltonian was introduced to describe the electronic structure of the noncentrosymmetric material CePt$_3$Si [17]. This model can describe two dimensional electron systems such as an oxide heterostructure or an interface between transition metal oxides, too.

The normal state Hamiltonian (1.23) is expressed by the 2×2 matrix in spin space

$$\mathscr{H} = \sum_{\boldsymbol{k}} \begin{pmatrix} c_{\boldsymbol{k}\uparrow}^{\dagger} & c_{\boldsymbol{k}\downarrow}^{\dagger} \end{pmatrix} \begin{pmatrix} \xi(\boldsymbol{k}) & -i\alpha\sqrt{\dfrac{3}{2}}\dfrac{k_-}{k_{\mathrm{F}}} \\ i\alpha\sqrt{\dfrac{3}{2}}\dfrac{k_+}{k_{\mathrm{F}}} & \xi(\boldsymbol{k}) \end{pmatrix} \begin{pmatrix} c_{\boldsymbol{k}\uparrow} \\ c_{\boldsymbol{k}\downarrow} \end{pmatrix}. \tag{1.24}$$

k_{F} is the Fermi wave number and $k_{\pm} \equiv k_x \pm i k_y$. Now the spin quantization axis is oriented parallel to the z axis. Let us transform the basis into the band basis in which the normal state Hamiltonian is diagonalized. Inserting the unitary matrices, Eq. (1.24) becomes

$$\mathscr{H} = \sum_{\boldsymbol{k}} \begin{pmatrix} c_{\boldsymbol{k}\uparrow}^{\dagger} & c_{\boldsymbol{k}\downarrow}^{\dagger} \end{pmatrix} \hat{U}_k \hat{U}_k^{\dagger} \begin{pmatrix} \xi(\boldsymbol{k}) & -i\alpha\sqrt{\dfrac{3}{2}}\dfrac{k_-}{k_{\mathrm{F}}} \\ i\alpha\sqrt{\dfrac{3}{2}}\dfrac{k_+}{k_{\mathrm{F}}} & \xi(\boldsymbol{k}) \end{pmatrix} \hat{U}_k \hat{U}_k^{\dagger} \begin{pmatrix} c_{\boldsymbol{k}\uparrow} \\ c_{\boldsymbol{k}\downarrow} \end{pmatrix}$$

$$= \sum_{\boldsymbol{k}} \begin{pmatrix} a_{\boldsymbol{k}\uparrow}^{\dagger} & a_{\boldsymbol{k}\downarrow}^{\dagger} \end{pmatrix} \begin{pmatrix} E_{\mathrm{II}}(\boldsymbol{k}) & 0 \\ 0 & E_{\mathrm{I}}(\boldsymbol{k}) \end{pmatrix} \begin{pmatrix} a_{\boldsymbol{k}\uparrow} \\ a_{\boldsymbol{k}\downarrow} \end{pmatrix}. \tag{1.25}$$

The excitation energies are $E_{\mathrm{I,II}}(\boldsymbol{k}) = \xi(\boldsymbol{k}) \pm \alpha |\boldsymbol{g}(\boldsymbol{k})|$. This two band feature is the consequence of lifting the spin degeneracy due to the SOC. We have defined the canonical transformations: $\left(\begin{array}{cc} a^\dagger_{\boldsymbol{k}\uparrow} & a^\dagger_{\boldsymbol{k}\downarrow} \end{array} \right) = \left(\begin{array}{cc} c^\dagger_{\boldsymbol{k}\uparrow} & c^\dagger_{\boldsymbol{k}\downarrow} \end{array} \right) \hat{U}_k$ and $\left(\begin{array}{cc} a_{\boldsymbol{k}\uparrow} & a_{\boldsymbol{k}\downarrow} \end{array} \right)^{\mathrm{T}} = \hat{U}^\dagger_k \left(\begin{array}{cc} c_{\boldsymbol{k}\uparrow} & c_{\boldsymbol{k}\downarrow} \end{array} \right)^{\mathrm{T}}$ with

$$\hat{U}_k = \frac{1}{\sqrt{2}} \begin{pmatrix} 1 & -i\bar{k}_- \\ -i\bar{k}_+ & 1 \end{pmatrix}, \quad \hat{U}^\dagger_k = \frac{1}{\sqrt{2}} \begin{pmatrix} 1 & i\bar{k}_- \\ i\bar{k}_+ & 1 \end{pmatrix}, \tag{1.26}$$

where $\bar{k}_\pm \equiv k_\pm / |k_\pm|$. When transforming the basis from the real spin basis into the band basis, we operate the unitary matrix, which represents the rotation in spin space. Here the unitary matrix depends on the wave vector. The unitary matrix rotates the spin quantization axis with respect to each wave vector. Hence, as depicted in Fig. 1.1, the spin quantization axis rotates on the Fermi surface. The way of lifting the spin degeneracy in noncentrosymmetric systems is different from other systems. One example is the Zeeman splitting electron systems under a high magnetic field, in which the Fermi surface is split with respect to a certain quantization axis. The Dirac electron system is another example.

1.3.3 Anderson's theorem

First of all, we assume that the system has an spatial inversion center. In this situation, we can label the single particle state occupying the certain energy band with the spin projection. We express this electronic state as the state vector $|\boldsymbol{k}\boldsymbol{\sigma}\rangle$ with the wave vector $\boldsymbol{k}$ and the spin vector $\boldsymbol{\sigma}$. Let us consider the case with the time-reversal symmetry. The time-reversal operation $\hat{T}$ reverses momentum, spin and orbital angular momentum [18]:

$$\hat{T}|\boldsymbol{k}\boldsymbol{\sigma}\rangle = |-\boldsymbol{k}-\boldsymbol{\sigma}\rangle, \tag{1.27}$$

where we choose the phase such that the phase factor is unity ($e^{i\phi} = 1$). The spatial inversion (parity) operation $\hat{P}$ reverses momentum only:

$$\hat{P}|\boldsymbol{k}\boldsymbol{\sigma}\rangle = |-\boldsymbol{k}\boldsymbol{\sigma}\rangle. \tag{1.28}$$

Combining the parity operator with the time-reversal operator, we obtain the following relation

$$\hat{P}\hat{T}|\boldsymbol{k}\boldsymbol{\sigma}\rangle = \hat{P}|-\boldsymbol{k}-\boldsymbol{\sigma}\rangle = |\boldsymbol{k}-\boldsymbol{\sigma}\rangle. \tag{1.29}$$

Hence, in the presence of the spatial inversion symmetry and the time-reversal symmetry, the four electronic states $|\boldsymbol{k}\boldsymbol{\sigma}\rangle$, $|-\boldsymbol{k}-\boldsymbol{\sigma}\rangle$, $|-\boldsymbol{k}\boldsymbol{\sigma}\rangle$ and $|\boldsymbol{k}-\boldsymbol{\sigma}\rangle$ are degenerated, i.e., $E(\boldsymbol{k},\boldsymbol{\sigma}) = E(-\boldsymbol{k},-\boldsymbol{\sigma}) = E(-\boldsymbol{k},\boldsymbol{\sigma}) = E(\boldsymbol{k},-\boldsymbol{\sigma})$. E is the energy spectra of conduction electrons.

If the time reversal symmetry is broken (e.g., under a magnetic field), the system has only the spatial inversion symmetry. Then, the two electronic states $|\boldsymbol{k}\boldsymbol{\sigma}\rangle$ and $|-\boldsymbol{k}\boldsymbol{\sigma}\rangle$ are degenerated, i.e., $E(\boldsymbol{k},\boldsymbol{\sigma}) = E(-\boldsymbol{k},\boldsymbol{\sigma})$.

Next, let us consider the case without an inversion center. In this case, two electronic states $|\boldsymbol{k}\boldsymbol{\sigma}\rangle$ and $|-\boldsymbol{k}-\boldsymbol{\sigma}\rangle$ are degenerated due to the time-reversal symmetry $[E(\boldsymbol{k},\boldsymbol{\sigma}) = E(-\boldsymbol{k},-\boldsymbol{\sigma})]$. Note that there remains the degeneracy at the Γ point ($\boldsymbol{k} = \boldsymbol{0}$) in the presence of the time-reversal symmetry, which is called Kramers degeneracy.

Anderson discussed which quasiparticle states degenerated on the Fermi surface can form the Cooper pairs. According to Ref. [19], the time-reversal symmetry is essential for the spin-singlet pairing. The quasiparticle states can form the Cooper pairs using the degenerated quasiparticle states $|\boldsymbol{k}\boldsymbol{\sigma}\rangle$ and $|-\boldsymbol{k}-\boldsymbol{\sigma}\rangle$ in the vicinity of the Fermi surface. The spin-singlet pairs are fragile against the time-reversal symmetry breaking perturbations such as magnetic impurities, ferromagnetism and Zeeman field. On the other hand, both the time-reversal symmetry and the spatial inversion symmetry are essential for the spin-triplet pairs [20]. They are fragile against breaking spatial inversion symmetry.

1.3.4 Parity mixing

According to the discussion in the subsection 1.3.3, inversion symmetry is essential for spin-triplet pairing. One would question whether or not the lack of an inversion center always prevent

degenerated quasiparticles from forming spin-triplet pair. Under a certain condition, the answer is No. That is, the spin-triplet state remains stable when the d vector is parallel to the orbital vector $[\boldsymbol{d}(\boldsymbol{k}) \parallel \boldsymbol{g}(\boldsymbol{k})]$ (see Appendix A as for the d vector) [17].

In the presence of an inversion center, the orbital part of the Cooper pair wave function is classified by the spatial parity (the eigen values of the parity operator are ± 1). Correspondingly, the spin part of the wave function is classified to spin singlet or triplet in order to satisfy the Pauli principle. In the absence of a spatial inversion center, however, the Cooper pair wave function needs not to be the eigen wave function of the parity operator. Thus the parity mixing of the wave function occurs.

1.4   Background and motivation

It is of great interest and of importance to identify the internal degree of freedom of the Cooper pair wave functions in unconventional superconductors. In this dissertation, through vortex core bound states, I focus on the different three unconventional superconductivity, namely anisotropic, noncentrosymmetric and locally noncentrosymmetric ones. In anisotropic pairing states, the relative orbital angular momentum of the Cooper pair remains. In noncentrosymmetric systems, the admixture of the Cooper pairs with the non-zero total spin and without the total spin occurs due to the breaking of the spatial parity. The local noncentrosymmetricity influences the internal structure of the Cooper pair. I address the following three topics: (i) Flux-flow resistivity under a rotating magnetic field in anisotropic superconductors, (ii) Impurity effect on the vortex bound states in noncentrosymmetric superconductors, and (iii) Electronic structure of a vortex core in multilayered superconductors.

First, I describe the background and the motivation for the first topic. My theoretical study stems from the measurement of the field-angle dependent flux-flow resistivity (FFR) by Yasuzuka *et al.* [21] They conducted the experiment of measuring the Josephson vortex flow resistance in the layered organic superconductor κ-(BEDT-TTF)$_2$Cu(NCS)$_2$ [22, 23] and found the four-fold in-plane anisotropy of the FFR. They mentioned the relation between the observed four-fold anisotropy of the FFR and the d-wave pairing symmetry. Yasuzuka *et al.* reported the in-plane anisotropy of the FFR of the layered organic superconductor λ-(BETS)$_2$GaCl$_4$, too [24]. Through a series of the flux-flow experiments, I became interested in the in-plane field-angle dependent measurement of the FFR in three dimensional system. In the three dimensional system, the vortices with the core around the vortex center are formed even under an in-plane field. In this situation, there are two possible interpretations of the field-angle dependence of the FFR. One is the anisotropy of the upper critical field H_{c2}. According to the theoretical study on the anisotropy of H_{c2} [25, 26], H_{c2} with a magnetic field H parallel to the anti-node is larger than that with H parallel to the gap node direction $[H_{c2}(\text{node}) < H_{c2}(\text{anti-node})]$. Correspondingly, $T_c(\text{anti-node})$ is larger than $T_c(\text{node})$. Thus, the FFR with $H \parallel$ the gap node direction is larger than that with $H \parallel$ the anti-node direction. In this study, I neglect the contribution of the anisotropy of H_{c2} to the FFR, since the contribution is not important unless considering the FFR in a high field. Another possible interpretation is the anisotropy of the quasiparticle (QP) relaxation inside a vortex core. The field-angle dependence of the QP scattering rate in a vortex core is still elusive. In moderately clean systems, the FFR is proportional to the QP scattering rate inside a vortex core [27] Our theoretical study is devoted to elucidating the relation between field direction and the FFR.

Next, I would like to present the background and motivation of the second topic. In clean noncentrosymmetric superconductors, off-diagonal components of the Green's function in the band basis vanishes in the bulk [28, 29] and even in the vicinity of a vortex [29, 30]. That is, the electronic state is decoupled with respect to each band split due to the SOC as introduced in section 1.3. As Frigeri *et al.* pointed out [28], the splitting two bands are not mixed by the position averaged impurity scattering in the bulk. I summarize the treatment of bulk impurity effects in noncentrosymmetric superconductors with use of the quasiclassical theory in appendix D. Up to now, several authors have theoretically investigated bulk impurity effects on the superconducting properties in noncentrosymmetric systems; the transition temperature T_c [28, 31], the spin susceptibility [32], the NMR relaxation rate [33] and the H_{c2} with the approach from

the strong SOC [34]. Bao *et al.* experimentally investigated the non-magnetic impurity effect on the T_c and the T-H phase diagram in Li_2Pd_3B [35]. In addition, they reported the impurity scattering effect of Li_2Pt_3B in comparison with Li_2Pd_3B with changing the impurity content systematically [36].

However, under inhomogeneous situations, the impurity effect is different from that in the bulk. In the presence of impurities around a vortex, off-diagonal components of the normal and anomalous Green's functions remain in the band representation for $s + p$-wave pair. Then, the Green's functions cannot be separated with respect to each Fermi surface which is splitting up due to the SOC. This consideration comes from the impurity effect around a vortex core, which is different from that in the bulk. Around a vortex, there is the superflow. Thereby anomalous Green's function becomes not invariant under the transformation $\boldsymbol{k} \rightarrow -\boldsymbol{k}$ and the formula of the anomalous self-energy changes from that in the bulk (see appendix D and Ref. [37] for more detailed discussions). Hence, the impurity scattering affects the quasiparticle structure of a vortex core and interesting phenomena in the vortex bound states are expected. The purpose of our theoretical study is to elucidate the impurity effect around a vortex core through vortex core states. The first STM/STS experiment on vortex core states in the noncentrosymmetric superconductor is conducted for BiPd [38]. This experiment also motivates our calculation of the quasiparticle structure at the vortex core.

At last, I present the background and motivation for the third topic. Recently, much interest has been focused on superconductivity in locally noncentrosymmetric systems (LNCS) [39, 40]. Yanase conducted the pioneering work pointing out the importance of the broken local inversion symmetry on the superconductivity focusing on the random SOC effect in Sr_2RuO_4 and $CePt_3Si$ [41]. After that, the Niigata University and ETH-Zürich groups have actively investigated superconductivity in LNCS focusing mainly on the heavy Fermion superlattice $CeCoIn_5/YbCoIn_5$ and pnictide superconductor SrPtAs. Yoshida *et al.* found that exotic inhomogeneous superconducting phases stabilize in multilayered systems under a high magnetic field. They numerically investigated the stability of the exotic superconducting state in the T-H phase diagram and showed the staggered anti-symmetric SOC arising from local noncentrosymmetriciry is essential. They found that the pair-density wave (PDW) phase is stabilized in a high field perpendicular to the atomic lattice layers [42] and the complex-stripe (CS) phase is stabilized under a field parallel to the layers [43]. In the PDW phase, the phase of the superconducting order parameter modulates layer by layer due to the spatially inhomogeneous spin-orbit coupling. The length scale of the modulation is the order of the atomic lattice constant, which is much shorter than that of the Fulde-Ferrell-Larkin-Ovchinnikov state [42, 44]. The uniform superconducting phase is more stable in a low magnetic field and is destroyed by the paramagnetic deparing in a high field, whereas the PDW phase can survive up to a high magnetic field by the presence of the SOC in the system where the paramagnetic depairing is dominant. On the other hand, in the CS phase, the amplitude and the phase of the order parameter modulates within the layer, which is in contrast with the helical vortex phase in noncentrosymmetric superconductors. In the helical vortex phase, only the order parameter phase modulates [45], and then a phase-sensitive probe is needed to detect experimentally the helical phase [45]. As for the CS state, the phase-sensitive probe is not necessary and the high resolution local probe such as the STM might detect the CS phase.

The exotic superconducting phases introduced above stabilize in a magnetic field. Although vortices do not affect the phase modulation and not play a crucial role in the stability of the PDW phase, the effect of vortices is of importance for transport and thermodynamic properties. In addition, the observation of quasiparticle states around a vortex gives us rich information on the pairing state in general. I believe that the observation of the vortex core states will be a key to identify the PDW state experimentally. Hence, I try to elucidate the vortex structure in the PDW state at the beginning stage of the theoretical study on vortex states in the exotic superconducting states.

1.5 Outline

In this dissertation, I address the following four topics.

- **Chapter 3** Field-angle Resolved Flux-flow Resistivity as a Phase-sensitive Probe of Unconventional Cooper Pairing:
  Y. Higashi, Y. Nagai, M. Machida, and N. Hayashi, Physical Review B **88**, 224511 (2013),
  Y. Higashi, Y. Nagai, M. Machida, and N. Hayashi, Physics Procedia **45**, 137-140 (2013).

- **Chapter 4** Impurity Effect on the Local Density of States around a Vortex in Noncentrosymmetric Superconductors:
  Y. Higashi, Y. Nagai, and N. Hayashi, JPS Conference Proceedings **3**, 015003 (2014).

- **Chapter 5** Vortex Core Structure in Multilayered Rashba Superconductors:
  Y. Higashi, Y. Nagai, T. Yoshida, and Y. Yanase, Journal of Physics: Conference Series **568**, 022018 (2014),
  Y. Higashi, Y. Nagai, T. Yoshida, Y. Masaki, and Y. Yanase, Submitted to Physical Review B.

- **Chapter 6** Excitation Spectra and Wave Functions of Quasiparticle Bound States in Bilayer Rashba Superconductors:
  Y. Higashi, Y. Nagai, T. Yoshida, M. Kato, and Y. Yanase, Submitted to Physica C.

In chapter 3, we investigate the flux-flow resistivity (FFR) under rotating magnetic field in anisotropic superconductors (SCs). First, on the basis of the quasiclassical theory and the Kramer-Pesch approximation, the FFR is analytically calculated from the impurity scattering rate inside a vortex core. Next, assuming the anisotropic superconducting pairing state (d-wave pair or line node s-wave one), we numerically calculate the in-plane field-angle dependence of the FFR.

In chapter 4, we focus on the impurity scattering effect on the local density of states (LDOS) around a vortex core in noncentrosymmetric SCs within the Born approximation. We discuss the spin-orbit coupling strength dependence of the impurity effect on the LDOS structure for both an s-wave and an $s + p$-wave pairing.

In chapter 5, we numerically investigate the vortex core structure in bilayer Rashba SCs by means of the self-consistent calculations using the quasiclassical theory. Especially, we discuss the spin-orbit coupling strength dependence of the core structure for both the BCS and the pair-density wave (PDW) states.

In chapter 6, we investigate the energy spectra and the wave functions of bound Bogoliubov quasiparticles at a vortex and an edge in the PDW state in bilayer systems on the basis of the Bogoliubov-de Gennes theory.

In chapter 7, we conclude our discussions.

Chapter 2

Mean Field Theory of Superconductivity

In this chapter, we would like to describe the quasiclassical Green's function method. In particular, we address the derivation of the quasiclassical theory of superconductivity in multilayered systems with the Rashba type spin-orbit coupling. For simpler systems, one can formulate in the same way.

2.1   System

We consider a multilayered superconductor with the Rashba-type spin-orbit coupling taking into account the paramagnetic effect. Each layer is connected through the inter-layer coupling. The system we consider is described by the Hamiltonian

$$\mathscr{H} = \mathscr{H}_{\mathrm{kin}} + \mathscr{H}_{\mathrm{Z}} + \mathscr{H}_{\mathrm{SO}} + \mathscr{H}_{\mathrm{inter}} + \mathscr{H}_{\mathrm{SC}} = \mathscr{H}_0 + \mathscr{H}_{\mathrm{SC}}, \tag{2.1}$$

where $\mathscr{H}_{\mathrm{SC}}$ is the two body interaction reproducing superconductivity. The kinetic energy term is

$$\mathscr{H}_{\mathrm{kin}} = \sum_{s,s',m} \int d\boldsymbol{r} \int d\boldsymbol{r}' \delta_{ss'} \delta(\boldsymbol{r} - \boldsymbol{r}') \xi\left(\boldsymbol{r}', -i\boldsymbol{\nabla}'\right) \psi_{sm}^{\dagger}(\boldsymbol{r})\psi_{s'm}(\boldsymbol{r}'), \tag{2.2}$$

where $\psi_{sm}^{\dagger}(\boldsymbol{r})$ $[\psi_{sm}(\boldsymbol{r})]$ is the field operator creating (annihilating) a quasiparticle with the spin s at the position $\boldsymbol{r}$ in the m-th superconducting layer in the Schrödinger representation, and the energy dispersion measured from the chemical potential μ,

$$\xi\left(\boldsymbol{r}', -i\boldsymbol{\nabla}'\right) = \frac{1}{2m}\left[-i\boldsymbol{\nabla}' + e\boldsymbol{A}(\boldsymbol{r}')\right]^2 - \mu, \tag{2.3}$$

with the mass of an electron m, the absolute value of the electron charge e, the velocity of light c and the vector potential $\boldsymbol{A}(\boldsymbol{r})$. From now on, we use units in which $\hbar = k_{\mathrm{B}} = c = 1$. The Zeeman term is

$$\mathscr{H}_{\mathrm{Z}} = \sum_{s,s',m} \int d\boldsymbol{r} \int d\boldsymbol{r}' \psi_{sm}^{\dagger}(\boldsymbol{r})\left[-\delta(\boldsymbol{r} - \boldsymbol{r}')\mu_{\mathrm{B}}\boldsymbol{H}\right] \cdot \boldsymbol{\sigma}_{ss'} \psi_{s'm}(\boldsymbol{r}'), \tag{2.4}$$

where μ_{B} is the magnetic moment of the quasiparticle, $\boldsymbol{H}$ is a magnetic field and $\boldsymbol{\sigma} = (\sigma_x, \sigma_y, \sigma_z)^{\mathrm{T}}$ is the vector consisting of the Pauli spin matrix. The spin-orbit coupling is described by

$$\mathscr{H}_{\mathrm{SO}} = \sum_{s,s',m} \int d\boldsymbol{r} \int d\boldsymbol{r}' \psi_{sm}^{\dagger}(\boldsymbol{r})\alpha_m \boldsymbol{g}(\boldsymbol{r} - \boldsymbol{r}') \cdot \boldsymbol{\sigma}_{ss'} \psi_{s'm}(\boldsymbol{r}'), \tag{2.5}$$

where α_m is the spin-orbit coupling energy in the m-th layer [e.g., $(\alpha_1, \alpha_2) = (\alpha, -\alpha)$ in the bilayer system]. $\boldsymbol{g}(\boldsymbol{r} - \boldsymbol{r}')$ is defined through $\boldsymbol{g}(\bar{\boldsymbol{k}})$ as

$$\boldsymbol{g}(\bar{\boldsymbol{k}}) = \int d\boldsymbol{r} e^{-i\bar{\boldsymbol{k}}\cdot\bar{\boldsymbol{r}}} \boldsymbol{g}(\bar{\boldsymbol{r}} = \boldsymbol{r} - \boldsymbol{r}'). \tag{2.6}$$

Here $\bar{\boldsymbol{k}}$ denotes the relative momentum. The inter-layer hopping is

$$\mathscr{H}_{\mathrm{inter}} = t_\perp \sum_{s,\langle m,m'\rangle} \int d\boldsymbol{r}\, \psi_{sm}^\dagger(\boldsymbol{r})\psi_{s,m'}(\boldsymbol{r}). \tag{2.7}$$

$\langle m,m'\rangle$ indicates the summation over the nearest neighbor layers. Hence, the normal state Hamiltonian is written as

$$\mathscr{H}_0 = \sum_{s,s',m} \int d\boldsymbol{r} \int d\boldsymbol{r}'\, \psi_{sm}^\dagger(\boldsymbol{r})\mathscr{H}_{ss'm}^0\left(\boldsymbol{r},\boldsymbol{r}',-i\boldsymbol{\nabla}'\right)\psi_{s'm}(\boldsymbol{r}') + t_\perp \sum_{s,\langle m,m'\rangle} \int d\boldsymbol{r}\, \psi_{sm}^\dagger(\boldsymbol{r})\psi_{s,m'}(\boldsymbol{r}),$$
$$\tag{2.8}$$

$$\mathscr{H}_{ss'm}^0\left(\boldsymbol{r},\boldsymbol{r}',-i\boldsymbol{\nabla}'\right) = \delta_{ss'}\delta(\boldsymbol{r}-\boldsymbol{r}')\xi\left(\boldsymbol{r}',-i\boldsymbol{\nabla}'\right) - \delta(\boldsymbol{r}-\boldsymbol{r}')\mu_{\mathrm{B}}\boldsymbol{H}\cdot\boldsymbol{\sigma}_{ss'} + \alpha_m \boldsymbol{g}(\boldsymbol{r}-\boldsymbol{r}')\cdot\boldsymbol{\sigma}_{ss'}. \tag{2.9}$$

At last, the interaction term for superconductivity is

$$\mathscr{H}_{\mathrm{SC}} = \frac{1}{2}\sum_{s,s',m} \int d\boldsymbol{r} \int d\boldsymbol{r}'\, \psi_{sm}^\dagger(\boldsymbol{r})\psi_{s'm}^\dagger(\boldsymbol{r}')V(\boldsymbol{r}-\boldsymbol{r}')\psi_{s'm}(\boldsymbol{r}')\psi_{sm}(\boldsymbol{r}), \tag{2.10}$$

where the pairing interaction $V(\boldsymbol{r}-\boldsymbol{r}')$ is defined by

$$V(\bar{\boldsymbol{r}} = \boldsymbol{r}-\boldsymbol{r}') = \sum_{\bar{\boldsymbol{k}}} V(\bar{\boldsymbol{k}})e^{i\bar{\boldsymbol{k}}\cdot\bar{\boldsymbol{r}}}. \tag{2.11}$$

2.2 Wigner representation of Gor'kov equation

The Gor'kov equation for multilayered systems is given by

$$\int d\boldsymbol{r}' \left[\begin{array}{cc} \left\{i\omega_n\sigma_0\otimes I_{N\times N} - \hat{\mathscr{H}}_0\left(\boldsymbol{r}'-i\boldsymbol{\nabla}'\right)\right\}\delta\left(\boldsymbol{r}-\boldsymbol{r}'\right) & \hat{\Delta}(\boldsymbol{r},\boldsymbol{r}',i\omega_n) \\ \hat{\Delta}^\dagger(\boldsymbol{r},\boldsymbol{r}',i\omega_n) & \left\{i\omega_n\sigma_0\otimes I_{N\times N} + \hat{\mathscr{H}}_0^*\left(\boldsymbol{r}',i\boldsymbol{\nabla}'\right)\right\}\delta\left(\boldsymbol{r}-\boldsymbol{r}'\right) \end{array} \right]$$
$$\left[\begin{array}{cc} \hat{\mathscr{G}}(\boldsymbol{r}',\boldsymbol{r}'',i\omega_n) & \hat{\mathscr{F}}(\boldsymbol{r}',\boldsymbol{r}'',i\omega_n) \\ \hat{\bar{\mathscr{F}}}(\boldsymbol{r}',\boldsymbol{r}'',i\omega_n) & \hat{\bar{\mathscr{G}}}(\boldsymbol{r}',\boldsymbol{r}'',i\omega_n) \end{array} \right] = \check{\tau}_0\delta(\boldsymbol{r}-\boldsymbol{r}''), \tag{2.12}$$

with

$$\hat{\mathscr{H}}_0\left(\boldsymbol{r}',-i\boldsymbol{\nabla}'\right) = \xi\left(\boldsymbol{r}',-i\boldsymbol{\nabla}'\right)\sigma_0\otimes I_{N\times N} - \mu_{\mathrm{B}}H\sigma_z\otimes I_{N\times N} + t_\perp\sigma_o\otimes T_\perp + \alpha\boldsymbol{g}\left(-i\boldsymbol{\nabla}'\right)\cdot\boldsymbol{\sigma}\otimes S_{\mathrm{d}}, \tag{2.13}$$

$$\hat{\mathscr{H}}_0^*\left(\boldsymbol{r}',i\boldsymbol{\nabla}'\right) = \xi'\left(\boldsymbol{r}',i\boldsymbol{\nabla}'\right)\sigma_0\otimes I_{N\times N} - \mu_{\mathrm{B}}H\sigma_z\otimes I_{N\times N} + t_\perp\sigma_o\otimes T_\perp + \alpha\boldsymbol{g}\left(i\boldsymbol{\nabla}'\right)\cdot\boldsymbol{\sigma}^*\otimes S_{\mathrm{d}}, \tag{2.14}$$

where $I_{N\times N}$ is the unit matrix. Here we restrict the discussion to bilayer systems ($N = 2$). $T_\perp = \mathrm{offdiag}(1,1)$ and $S_{\mathrm{d}} = \mathrm{diag}(1,-1)$. These are the matrices in the space composed of the layer degree of freedom. $\hat{\mathscr{G}}$ and $\hat{\mathscr{F}}$ are the normal and anomalous temperature Green's functions, respectively, represented by the 4×4 matrix in the space composed of spin and layer degree of freedom. The orbital vector satisfies the relation $\boldsymbol{g}(i\boldsymbol{\nabla}') = -\boldsymbol{g}(-i\boldsymbol{\nabla}')$ due to the time-reversal symmetry of the spin-orbit coupling term. By inserting $\check{\tau}_3^2 = \check{\tau}_0$ into the Gor'kov equation (2.12),

we obtain

$$
\int d\boldsymbol{r}' \left[
\begin{array}{cc}
\left\{ i\omega_n\sigma_0 \otimes I_{N\times N} - \hat{\mathscr{H}}_0\left(\boldsymbol{r}', -i\boldsymbol{\nabla}'\right)\right\}\delta\left(\boldsymbol{r}-\boldsymbol{r}'\right) & -\hat{\Delta}(\boldsymbol{r},\boldsymbol{r}',i\omega_n) \\
\hat{\Delta}^\dagger(\boldsymbol{r},\boldsymbol{r}',i\omega_n) & -\left\{ i\omega_n\sigma_0 \otimes I_{N\times N} + \hat{\mathscr{H}}_0^*\left(\boldsymbol{r}', i\boldsymbol{\nabla}'\right)\right\}\delta\left(\boldsymbol{r}-\boldsymbol{r}'\right)
\end{array}
\right]
$$

$$
\left[
\begin{array}{cc}
\hat{\mathscr{G}}(\boldsymbol{r}',\boldsymbol{r}'',i\omega_n) & \hat{\mathscr{F}}(\boldsymbol{r}',\boldsymbol{r}'',i\omega_n) \\
-\hat{\bar{\mathscr{F}}}(\boldsymbol{r}',\boldsymbol{r}'',i\omega_n) & -\hat{\bar{\mathscr{G}}}(\boldsymbol{r}',\boldsymbol{r}'',i\omega_n)
\end{array}
\right] = \check{\tau}_0\delta(\boldsymbol{r}-\boldsymbol{r}''),
$$

$$
\int d\boldsymbol{r}'\Bigg[i\omega_n\delta(\boldsymbol{r}-\boldsymbol{r}')\check{\tau}_3 - \left(
\begin{array}{cc}
\hat{\mathscr{H}}_0(\boldsymbol{r}',-i\boldsymbol{\nabla}')\delta(\boldsymbol{r}-\boldsymbol{r}') & \hat{0} \\
\hat{0} & \hat{\mathscr{H}}_0^*(\boldsymbol{r}',i\boldsymbol{\nabla}')\delta(\boldsymbol{r}-\boldsymbol{r}')
\end{array}
\right)
$$

$$
- \left(
\begin{array}{cc}
\hat{0} & \hat{\Delta}(\boldsymbol{r},\boldsymbol{r}',i\omega_n) \\
-\hat{\Delta}^\dagger(\boldsymbol{r},\boldsymbol{r}',i\omega_n) & \hat{0}
\end{array}
\right)\Bigg]
\left[
\begin{array}{cc}
\hat{\mathscr{G}}(\boldsymbol{r}',\boldsymbol{r}'',i\omega_n) & \hat{\mathscr{F}}(\boldsymbol{r}',\boldsymbol{r}'',i\omega_n) \\
-\hat{\bar{\mathscr{F}}}(\boldsymbol{r}',\boldsymbol{r}'',i\omega_n) & -\hat{\bar{\mathscr{G}}}(\boldsymbol{r}',\boldsymbol{r}'',i\omega_n)
\end{array}
\right] = \check{\tau}_0\delta(\boldsymbol{r}-\boldsymbol{r}''),
$$

$$(2.15)$$

where we define the Pauli matrix in Nambu space as

$$
\check{\tau}_3 = \left(
\begin{array}{cc}
\sigma_0 \otimes I_{N\times N} & \hat{0} \\
\hat{0} & -\sigma_0 \otimes I_{N\times N}
\end{array}
\right). \tag{2.16}
$$

Here we have neglected the vector potential. Then, the normal state Hamiltonian depends only on the spatial derivative [i.e., $\hat{\mathscr{H}}_0(\boldsymbol{r}', -i\boldsymbol{\nabla}') \to \hat{\mathscr{H}}_0(-i\boldsymbol{\nabla}')$].

Next, we would like to have the Wigner representation for the Gor'kov equation. The Gor'kov equation is composed of the product of the BdG mean field Hamiltonian and the Green's function matrix in Nambu space. To obtain the Wigner representation of the product of the matrices, the circle product or the Moyal product is introduced (see Appendix B) [46, 47, 48, 49, 50, 51]. Before obtaining the Wigner representation of the Gor'kov equation, we first consider the Wigner representation of the normal state Hamiltonian.

$$
\hat{\mathscr{H}}_0(\boldsymbol{R}, \bar{\boldsymbol{k}}) = \int e^{-i\bar{\boldsymbol{k}}\cdot\bar{\boldsymbol{r}}} \hat{\mathscr{H}}_0\left[-i\left(\frac{1}{2}\boldsymbol{\nabla}_{\boldsymbol{R}} + \boldsymbol{\nabla}_{\bar{\boldsymbol{r}}}\right)\right]\delta(\bar{\boldsymbol{r}})d\bar{\boldsymbol{r}}
$$

$$
= \int e^{-i\bar{\boldsymbol{k}}\cdot\bar{\boldsymbol{r}}}\hat{\mathscr{H}}_0\left(-i\boldsymbol{\nabla}_{\bar{\boldsymbol{r}}}\right)\delta(\bar{\boldsymbol{r}})d\bar{\boldsymbol{r}}. \tag{2.17}
$$

The superconducting order parameter Δ varies spatially over the coherence length ξ, which is the characteristic distance of the electronic state in superconductivity. ξ is much longer than the wavelength of the band electrons in the vicinity of the Fermi energy $2\pi/k_{\mathrm{F}}$. In the energy axis, the characteristic energy scale for superconductivity is much smaller than the electron energy at the Fermi level ($\Delta \ll E_{\mathrm{F}}$). Then the band electron dispersion is nearly linear in $\bar{\boldsymbol{k}}$ in the energy scale of Δ around the Fermi level. Hence, we can expand the band electron energy with respect to $-i\boldsymbol{\nabla}_{\bar{\boldsymbol{r}}}$,

$$
\varepsilon\left[\bar{\boldsymbol{k}} + (-i\boldsymbol{\nabla}_{\bar{\boldsymbol{r}}})\right] - \mu \approx \xi(\bar{\boldsymbol{k}}) + \boldsymbol{\nabla}_{\bar{\boldsymbol{k}}}\varepsilon(\bar{\boldsymbol{k}})\cdot(-i\boldsymbol{\nabla}_{\bar{\boldsymbol{r}}}),
$$

$$
= \xi(\bar{\boldsymbol{k}}) + \boldsymbol{v}(\bar{\boldsymbol{k}})\cdot(-i\boldsymbol{\nabla}_{\bar{\boldsymbol{r}}}). \tag{2.18}
$$

Here we assume that the Zeeman field, the spin-orbit coupling and the interlayer coupling are sufficiently small. So the split of the Fermi surface due to the spin degeneracy lifting is also small. Then, we can define the velocity of the band electron on a spin degenerated single Fermi surface. If $\hat{\mathscr{H}}_0(\bar{\boldsymbol{k}})$ can be expanded in a power series of $-i\boldsymbol{\nabla}_{\bar{\boldsymbol{r}}}$, we obtain $\hat{\mathscr{H}}_0(\boldsymbol{R}, \bar{\boldsymbol{k}}) = \hat{\mathscr{H}}_0(\bar{\boldsymbol{k}})$.

Consequently, using the circle or Moyal product described in Appendix B, the Wigner representation of the Gor'kov equation is obtained as

$$
\left[i\omega_n\check{\tau}_3 - \xi(\bar{\boldsymbol{k}})\check{\tau}_0 - \check{\mathscr{K}}(\bar{\boldsymbol{k}}) - \check{\Delta}(\boldsymbol{R}, \bar{\boldsymbol{k}}, i\omega_n)\right] \circ \check{\mathscr{G}}(\boldsymbol{R}, \bar{\boldsymbol{k}}, i\omega_n) = \check{\tau}_0, \tag{2.19}
$$

13

where

$$\check{\mathscr{K}}(\bar{\boldsymbol{k}}) = -\mu_{\mathrm{B}}\boldsymbol{H} \cdot \check{\boldsymbol{S}} + \alpha\check{\boldsymbol{g}}(\bar{\boldsymbol{k}}) \cdot \check{\boldsymbol{S}} + t_{\perp}(\sigma_0 \otimes T_{\perp}) \otimes \check{\tau}_0, \tag{2.20}$$

$$\check{\boldsymbol{S}} = \begin{pmatrix} \boldsymbol{\sigma} \otimes I_{N \times N} & \hat{0} \\ \hat{0} & \boldsymbol{\sigma}^* \otimes I_{N \times N} \end{pmatrix}, \tag{2.21}$$

$$\check{\boldsymbol{g}}(\bar{\boldsymbol{k}}) = \begin{pmatrix} \boldsymbol{g}(\bar{\boldsymbol{k}})\sigma_0 \otimes S_{\mathrm{d}} & \hat{0} \\ \hat{0} & \boldsymbol{g}(-\bar{\boldsymbol{k}})\sigma_0 \otimes S_{\mathrm{d}} \end{pmatrix}, \tag{2.22}$$

$$\check{\Delta}(\boldsymbol{R}, \bar{\boldsymbol{k}}, i\omega_n) = \begin{pmatrix} \hat{0} & \hat{\Delta}(\boldsymbol{R}, \bar{\boldsymbol{k}}, i\omega_n) \\ -\hat{\Delta}^{\dagger}(\boldsymbol{R}, \bar{\boldsymbol{k}}, i\omega_n) & \hat{0} \end{pmatrix}, \tag{2.23}$$

$$\check{\mathscr{G}}(\boldsymbol{R}, \bar{\boldsymbol{k}}, i\omega_n) = \begin{pmatrix} \hat{\mathscr{G}}(\boldsymbol{R}, \bar{\boldsymbol{k}}, i\omega_n) & \hat{\mathscr{F}}(\boldsymbol{R}, \bar{\boldsymbol{k}}, i\omega_n) \\ -\hat{\bar{\mathscr{F}}}(\boldsymbol{R}, \bar{\boldsymbol{k}}, i\omega_n) & -\hat{\bar{\mathscr{G}}}(\boldsymbol{R}, \bar{\boldsymbol{k}}, i\omega_n) \end{pmatrix}. \tag{2.24}$$

2.3 Quasiclassical Green's function method

First of all, we expand the circle or Moyal product in the Gor'kov equation up to first order (see Appendix B),

$$\xi(\bar{\boldsymbol{k}})\check{\tau}_0 \circ \check{\mathscr{G}} \approx \xi(\bar{\boldsymbol{k}})\check{\mathscr{G}} - \frac{i}{2}\boldsymbol{\nabla}_{\bar{\boldsymbol{k}}}\xi(\bar{\boldsymbol{k}})\check{\tau}_0\boldsymbol{\nabla}_{\boldsymbol{R}}\check{\mathscr{G}} \tag{2.25}$$

$$\check{\mathscr{K}} \circ \check{\mathscr{G}} \approx \check{\mathscr{K}}\check{\mathscr{G}} - \frac{i}{2}\boldsymbol{\nabla}_{\bar{\boldsymbol{k}}}\check{\mathscr{K}}\boldsymbol{\nabla}_{\boldsymbol{R}}\check{\mathscr{G}} \tag{2.26}$$

$$\check{\Delta} \circ \check{\mathscr{G}} \approx \check{\Delta}\check{\mathscr{G}} + \frac{i}{2}\big(\boldsymbol{\nabla}_{\boldsymbol{R}}\check{\Delta}\boldsymbol{\nabla}_{\bar{\boldsymbol{k}}}\check{\mathscr{G}} - \boldsymbol{\nabla}_{\bar{\boldsymbol{k}}}\check{\Delta}\boldsymbol{\nabla}_{\boldsymbol{R}}\check{\mathscr{G}}\big)$$

$$\approx \check{\Delta}\check{\mathscr{G}} + \frac{i}{2}\boldsymbol{\nabla}_{\boldsymbol{R}}\check{\Delta}\boldsymbol{\nabla}_{\bar{\boldsymbol{k}}}\check{\mathscr{G}}. \tag{2.27}$$

Here we neglect $\bar{\boldsymbol{k}}$ dependence of the order parameter. This is because the superconducting gap can be viewed as nearly flat in $\bar{\boldsymbol{k}}$ in the vicinity of $\bar{\boldsymbol{k}}_{\mathrm{F}}$ (i.e., around the Fermi energy E_{F}) if the gap size is much smaller than E_{F}. Thus, the Gor'kov equation is obtained as

$$\big[i\omega_n\check{\tau}_3 - \xi(\bar{\boldsymbol{k}})\check{\tau}_0 - \check{\mathscr{K}}(\bar{\boldsymbol{k}}) - \check{\Delta}(\boldsymbol{R}, \bar{\boldsymbol{k}}, i\omega_n)\big]\check{\mathscr{G}}(\boldsymbol{R}, \bar{\boldsymbol{k}}, i\omega_n) + \frac{i}{2}\boldsymbol{v}(\bar{\boldsymbol{k}})\check{\tau}_0 \cdot \boldsymbol{\nabla}_{\boldsymbol{R}}\check{\mathscr{G}}(\boldsymbol{R}, \bar{\boldsymbol{k}}, i\omega_n)$$

$$+ \frac{i}{2}\boldsymbol{\nabla}_{\bar{\boldsymbol{k}}}\check{\mathscr{K}}(\bar{\boldsymbol{k}})\boldsymbol{\nabla}_{\boldsymbol{R}}\check{\mathscr{G}}(\boldsymbol{R}, \bar{\boldsymbol{k}}, i\omega_n) - \frac{i}{2}\boldsymbol{\nabla}_{\boldsymbol{R}}\check{\Delta}(\boldsymbol{R}, \bar{\boldsymbol{k}}, i\omega_n)\boldsymbol{\nabla}_{\bar{\boldsymbol{k}}}\check{\mathscr{G}}(\boldsymbol{R}, \bar{\boldsymbol{k}}, i\omega_n) = \check{\tau}_0. \tag{2.28}$$

In the same way, another Gor'kov equation is obtained as

$$\check{\mathscr{G}}(\boldsymbol{R}, \bar{\boldsymbol{k}}, i\omega_n)\big[i\omega_n\check{\tau}_3 - \xi(\bar{\boldsymbol{k}})\check{\tau}_0 - \check{\mathscr{K}}(\bar{\boldsymbol{k}}) - \check{\Delta}(\boldsymbol{R}, \bar{\boldsymbol{k}}, i\omega_n)\big] - \frac{i}{2}\boldsymbol{\nabla}_{\boldsymbol{R}}\check{\mathscr{G}}(\boldsymbol{R}, \bar{\boldsymbol{k}}, i\omega_n) \cdot \boldsymbol{v}(\bar{\boldsymbol{k}})\check{\tau}_0$$

$$- \frac{i}{2}\boldsymbol{\nabla}_{\boldsymbol{R}}\check{\mathscr{G}}(\boldsymbol{R}, \bar{\boldsymbol{k}}, i\omega_n)\boldsymbol{\nabla}_{\bar{\boldsymbol{k}}}\check{\mathscr{K}}(\bar{\boldsymbol{k}}) + \frac{i}{2}\boldsymbol{\nabla}_{\bar{\boldsymbol{k}}}\check{\mathscr{G}}(\boldsymbol{R}, \bar{\boldsymbol{k}}, i\omega_n)\boldsymbol{\nabla}_{\boldsymbol{R}}\check{\Delta}(\boldsymbol{R}, \bar{\boldsymbol{k}}, i\omega_n) = \check{\tau}_0. \tag{2.29}$$

Subtracting Eq. (2.29) from Eq. (2.28), we have

$$\big[i\omega_n\check{\tau}_3 - \check{\mathscr{K}}(\bar{\boldsymbol{k}}) - \check{\Delta}(\boldsymbol{R}, \bar{\boldsymbol{k}}, i\omega_n), \check{\mathscr{G}}(\boldsymbol{R}, \bar{\boldsymbol{k}}, i\omega_n)\big]_- + i\boldsymbol{v}(\bar{\boldsymbol{k}})\check{\tau}_0 \cdot \boldsymbol{\nabla}_{\boldsymbol{R}}\check{\mathscr{G}}(\boldsymbol{R}, \bar{\boldsymbol{k}}, i\omega_n)$$

$$+ \frac{i}{2}\big[\boldsymbol{\nabla}_{\bar{\boldsymbol{k}}}\check{\mathscr{K}}(\bar{\boldsymbol{k}}), \boldsymbol{\nabla}_{\boldsymbol{R}}\check{\mathscr{G}}(\boldsymbol{R}, \bar{\boldsymbol{k}}, i\omega_n)\big]_+ - \frac{i}{2}\big[\boldsymbol{\nabla}_{\boldsymbol{R}}\check{\Delta}(\boldsymbol{R}, \bar{\boldsymbol{k}}, i\omega_n), \boldsymbol{\nabla}_{\bar{\boldsymbol{k}}}\check{\mathscr{G}}(\boldsymbol{R}, \bar{\boldsymbol{k}}, i\omega_n)\big]_+ = \check{0}. \tag{2.30}$$

In superconducting states, the energy gap opens in the quasiparticle energy spectrum corresponding to the vicinity of the Fermi surface. If the condition $\Delta \ll E_{\mathrm{F}}$ is satisfied, we can put the quasiparticle energy $\xi_{\bar{\boldsymbol{k}}} = v_{\mathrm{F}}(\bar{\boldsymbol{k}} - \bar{\boldsymbol{k}}_{\mathrm{F}})$. Then the derivative with respect to $\bar{\boldsymbol{k}}$ is proportional to that to $\xi_{\bar{\boldsymbol{k}}}$. Integrating Eq. (2.30) over the quasiparticle energy in the vicinity of the Fermi surface $\xi_{\bar{\boldsymbol{k}}}$, the derivative terms with respect to $\bar{\boldsymbol{k}}$ vanish from the equation. The Green's functions

describe the low lying quasiparticles in the vicinity of the Fermi surface, and their excitation energy correspond to the poles of the Green's function. Thus, we define the $\xi_{\bar{k}}$ integrated Green's function, namely, the quasiclassical Green's function as [51]

$$\check{g}(\boldsymbol{R}, \tilde{\bar{\boldsymbol{k}}}, i\omega_n) \equiv \oint d\xi_{\bar{\boldsymbol{k}}} \check{\mathscr{G}}(\boldsymbol{R}, \bar{\boldsymbol{k}}, i\omega_n) \tag{2.31}$$

$$\equiv -i\pi \begin{pmatrix} \hat{g}(\boldsymbol{R}, \tilde{\bar{\boldsymbol{k}}}, i\omega_n) & i\hat{f}(\boldsymbol{R}, \tilde{\bar{\boldsymbol{k}}}, i\omega_n) \\ -i\hat{\bar{f}}(\boldsymbol{R}, \tilde{\bar{\boldsymbol{k}}}, i\omega_n) & -\hat{\bar{g}}(\boldsymbol{R}, \tilde{\bar{\boldsymbol{k}}}, i\omega_n) \end{pmatrix}, \tag{2.32}$$

where the contour integral takes in the contribution from the poles in the vicinity of the Fermi surface. Consequently, we obtain the Eilenberger equation

$$i\boldsymbol{v}_{\mathrm{F}}(\tilde{\bar{\boldsymbol{k}}})\check{\tau}_0 \cdot \boldsymbol{\nabla}_{\boldsymbol{R}}\check{g}(\boldsymbol{R}, \tilde{\bar{\boldsymbol{k}}}, i\omega_n) + \left[i\omega_n\check{\tau}_3 - \check{\mathscr{K}}(\tilde{\bar{\boldsymbol{k}}}) - \check{\Delta}(\boldsymbol{R}, \tilde{\bar{\boldsymbol{k}}}, i\omega_n), \check{g}(\boldsymbol{R}, \tilde{\bar{\boldsymbol{k}}}, i\omega_n) \right]_{-} = \check{0}. \tag{2.33}$$

We have replaced the quasiparticle velocity with the Fermi velocity when introducing the quasiclassical Green's function.

Chapter 3

Field-angle Resolved Flux-flow Resistivity as a Phase-sensitive Probe of Unconventional Cooper Pairing

We theoretically investigate the applied magnetic field-angle dependence of the flux-flow resistivity $\rho_{\mathrm{f}}(\alpha_{\mathrm{M}})$ for both a uniaxially anisotropic Fermi surface and an in-plane anisotropic one. ρ_{f} is related to the quasiparticle scattering rate inside a vortex core, which reflects the sign change in the superconducting pair potential. We find that $\rho_{\mathrm{f}}(\alpha_{\mathrm{M}})$ is sensitive to the sign change in the pair potential and has its maximum when the magnetic field is parallel to the gap-node direction. We propose the measurement of the field-angle dependent oscillation of $\rho_{\mathrm{f}}(\alpha_{\mathrm{M}})$ as a phase-sensitive field-angle resolved experiment.

3.1   Introduction

It is of great importance to elucidate the symmetry of a superconducting pair potential when studying the Cooper pairing mechanisms in unconventional superconductors (SCs). The pair potential is composed of spin and orbital wave functions. The orbital wave function is characterized by its amplitude and phase (sign of the wave function).

In the past decade, experimental techniques for the field-angle resolved specific heat and thermal conductivity measurements have developed to identify the Cooper pairing symmetry in various superconducting systems [52, 53]. These angle-resolved measurements are powerful techniques that can detect the anisotropy of the pair potential amplitude. The theory proposed by Vorontsov and Vekhter has successfully explained these experiments for CeCoIn$_5$ assuming d-wave Cooper pairing [54, 55]. However, these field-angle resolved experiments cannot probe the sign change in the pair potential. That is, they are not phase-sensitive probes. In addition to detecting the anisotropy of the pair potential, it is crucial to probe the phase of the Cooper pair in order to discriminate unconventional SCs, including iron-based SCs, from conventional ones.

Until now, only a few phase-sensitive probes have been developed and succeeded, e.g., the half-flux quantum observation in the tricrystal geometry by a scanning SQUID (superconducting quantum interference device) microscope [56], and detecting the quasiparticle interference pattern by scanning tunneling spectroscopy (STS) [57]. Another phase-sensitive probe is measuring bound states at an interface by point-contact spectroscopy or STS experiments. If both sides of a SC/SC junction are of the same pair potential amplitude but with opposite signs, the quasiparticle (QP) path through the interface acquires a π phase shift and generating bound states around the interface. This situation is similar to a vortex line in superconductors. However, there is

the difficulty of fabricating a junction in terms of nono-structured processing techniques. Actually, the phase-sensitive test using SC/SC junctions succeeds only for cuprate superconductors [58, 59]. In addition to these existing experiments, a new phase-sensitive test is highly desired.

In this study, we propose a new experiment that can detect the phase (sign-change) of the pair potential free from fabricating a SC/SC junction. This is the great advantage of the phase-sensitive test proposed in the present work. We theoretically study the in-plane field-angle dependence of the flux-flow resistivity $\rho_{\mathrm{f}}(\alpha_{\mathrm{M}})$ for typical gap functions and Fermi surface (FS). From our numerical calculations, we show that the phase-sensitive QP scattering inside a vortex core leads to different behavior of $\rho_{\mathrm{f}}(\alpha_{\mathrm{M}})$ between conventional and unconventional Cooper pairing. In addition, we show that $\rho_{\mathrm{f}}(\alpha_{\mathrm{M}})$ has its maximum when the applied magnetic field $\boldsymbol{H}$ is parallel to the gap-node directions. Our results show that the field-angle dependence of the flux-flow resistivity can detect both the sign change of the pair potential and the direction of the gap nodes.

3.2   Flux-flow resistivity and quasiparticle scattering rate

The flux-flow resistivity ρ_{f} is dominated by the quasiparticle within a vortex core. We assume the system belongs to the moderately clean regime, in which there are two important contributions to ρ_{f}. One is the QP scattering rate Γ inside a vortex core, and the other is the momentum-dependent quantum level spacing of the vortex bound states $\omega_0(\boldsymbol{k}_{\mathrm{F}})$ [60, 61, 62, 63]. Here, the QP scattering is due to non-magnetic impurities randomly distributed in the system.

We attribute the flux-flow resistivity ρ_{f} to the energy dissipation of the vortex bound states due to the impurity scattering inside a vortex core [27]. ρ_{f} is characterized by the two quantities mentioned above [60, 61, 62, 63],

$$\rho_{\mathrm{f}}(T) \propto \frac{\Gamma_{\mathrm{n}}}{\Delta_0} \left[\frac{1}{\nu_0} \int \frac{dS_{\mathrm{F}}}{|\boldsymbol{v}_{\mathrm{F}}(\boldsymbol{k}_{\mathrm{F}})|} \frac{\omega_0(\boldsymbol{k}_{\mathrm{F}})}{\Delta_0} \frac{\Gamma_{\mathrm{n}}}{\Gamma(\varepsilon = k_{\mathrm{B}}T, \boldsymbol{k}_{\mathrm{F}})} \right]^{-1}, \tag{3.1}$$

where Γ_{n} is the impurity scattering rate in the normal state and Δ_0 is the bulk amplitude of the pair potential. We assume that the temperature T dependence of ρ_{f} comes predominantly from Γ with the QP energy $\varepsilon = k_{\mathrm{B}}T$. Here, we have made a rough estimate. Actually, the QPs distributed with the energy width $\Delta\varepsilon \sim k_{\mathrm{B}}T$ contribute to Γ. The total density of states on a FS is $\nu_0 = \int dS_{\mathrm{F}}/|\boldsymbol{v}_{\mathrm{F}}(\boldsymbol{k}_{\mathrm{F}})|$, with $dS_{\mathrm{F}} = |\boldsymbol{k}_{\mathrm{F}}(\phi_k, \theta_k)|^2 \sin\theta_k d\phi_k d\theta_k$ being an area element on the FS, the Fermi velocity $\boldsymbol{v}_{\mathrm{F}}(\boldsymbol{k}_{\mathrm{F}}) = \boldsymbol{\nabla}_{\boldsymbol{k}}\epsilon(\boldsymbol{k})|_{\boldsymbol{k}=\boldsymbol{k}_{\mathrm{F}}}$, and the Fermi wave vector $\boldsymbol{k}_{\mathrm{F}} = |\boldsymbol{k}_{\mathrm{F}}(\phi_k, \theta_k)|(\bar{\boldsymbol{a}}\cos\phi_k\sin\theta_k + \bar{\boldsymbol{b}}\sin\phi_k\sin\theta_k + \bar{\boldsymbol{c}}\cos\theta_k)$. $\epsilon(\boldsymbol{k})$ is the energy dispersion of electrons. ϕ_k (θ_k) is the azimuthal (polar) angle on the FS. $\bar{\boldsymbol{a}}$, $\bar{\boldsymbol{b}}$, and $\bar{\boldsymbol{c}}$ denote orthogonal unit vectors spanning crystal coordinates. We use the unit system in which $\hbar = 1$.

The momentum-dependent inter-level spacing of the vortex bound states $\omega_0(\boldsymbol{k}_{\mathrm{F}})$ is obtained analytically as [64, 65, 66, 67] $\omega_0(\boldsymbol{k}_{\mathrm{F}}) = 2|d(\boldsymbol{k}_{\mathrm{F}})|^2\Delta_0^2/[|\boldsymbol{k}_{\mathrm{F}\perp}||\boldsymbol{v}_{\mathrm{F}\perp}(\boldsymbol{k}_{\mathrm{F}})|]$ using the quasiclassical Green's function method and the Kramer-Pesch approximation [68, 10, 69]. $d(\boldsymbol{k}_{\mathrm{F}})$ indicates the anisotropy of pair potential and the vector with $\perp$ denotes the vector component projected onto the plane perpendicular to $\boldsymbol{H}$. We treat the non-magnetic impurity scattering by means of the Born approximation [27, 70, 71, 72]. The quasiparticle scattering rate for the QPs with the energy ε inside a vortex core is obtained as [69, 73]

$$\frac{\Gamma(\varepsilon)}{\Gamma_{\mathrm{n}}} = \left\langle \left\langle \frac{\Gamma(\boldsymbol{k}_{\mathrm{F}}, \boldsymbol{k}'_{\mathrm{F}}, \varepsilon)}{\Gamma_{\mathrm{n}}} \right\rangle_{\mathrm{FS}'} \right\rangle_{\mathrm{FS}}, \tag{3.2}$$

$$\frac{\Gamma(\boldsymbol{k}_{\mathrm{F}}, \boldsymbol{k}'_{\mathrm{F}}, \varepsilon)}{\Gamma_{\mathrm{n}}} = \frac{\pi}{2} C(\boldsymbol{k}_{\mathrm{F}}, \boldsymbol{k}'_{\mathrm{F}}) D(\boldsymbol{k}_{\mathrm{F}}, \boldsymbol{k}'_{\mathrm{F}}) F(\varepsilon, \boldsymbol{k}_{\mathrm{F}}, \boldsymbol{k}'_{\mathrm{F}}), \tag{3.3}$$

$$C(\boldsymbol{k}_{\mathrm{F}}, \boldsymbol{k}'_{\mathrm{F}}) = 1 - \mathrm{sgn}[d(\boldsymbol{k}_{\mathrm{F}})d(\boldsymbol{k}'_{\mathrm{F}})]\cos\Theta, \tag{3.4}$$

$$D(\boldsymbol{k}_{\mathrm{F}}, \boldsymbol{k}'_{\mathrm{F}}) = \frac{1}{|\sin\Theta|}, \tag{3.5}$$

$$F(\varepsilon, \boldsymbol{k}_{\mathrm{F}}, \boldsymbol{k}'_{\mathrm{F}}) = \frac{|\boldsymbol{v}_{\mathrm{F}\perp}(\boldsymbol{k}'_{\mathrm{F}})|}{|\boldsymbol{v}_{\mathrm{F}\perp}(\boldsymbol{k}_{\mathrm{F}})|} \frac{|d(\boldsymbol{k}_{\mathrm{F}})|}{|d(\boldsymbol{k}'_{\mathrm{F}})|} e^{-u(s_0, \boldsymbol{k}_{\mathrm{F}})} e^{-u(s'_0, \boldsymbol{k}'_{\mathrm{F}})}. \tag{3.6}$$
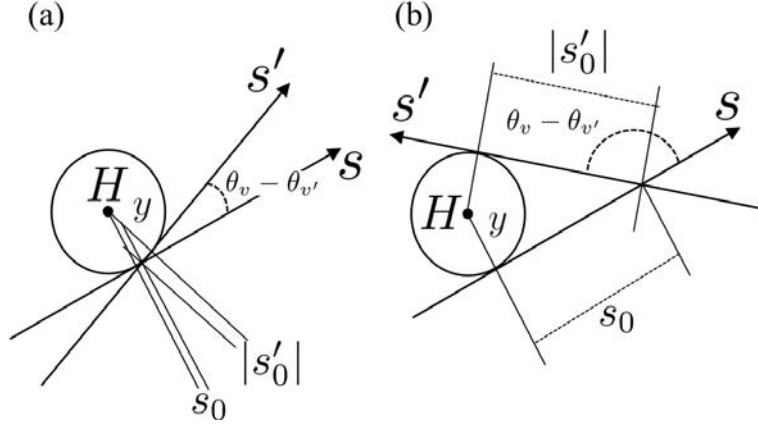
17

Figure 3.1: The schematic figures of (a) the forward scattering and (b) the backward scattering in the vicinity of a vortex. s and s' indicate the QP trajectory before and after scattering, respectively. Reprinted figure with permission from [Yoichi Higashi, Yuki Nagai, Masahiko Machida, and Nobuhiko Hayashi, Physical Review B **88**, 224511 (2013)] Copyright (2013) by the American Physical Society.

Here, $\langle \cdots \rangle_{\mathrm{FS}} \equiv (1/\nu_0) \int dS_{\mathrm{F}} \cdots / |\boldsymbol{v}_{\mathrm{F}}(\boldsymbol{k}_{\mathrm{F}})|$, $\Theta(\boldsymbol{k}_{\mathrm{F}}, \boldsymbol{k}'_{\mathrm{F}}) \equiv \theta_v(\boldsymbol{k}_{\mathrm{F}}) - \theta_{v'}(\boldsymbol{k}'_{\mathrm{F}})$ for the scattering angle [see Fig. 3.1]. Γ has the decay factor $\exp[-u(s_0, \boldsymbol{k}_{\mathrm{F}})]$ with $u(s_0, \boldsymbol{k}_{\mathrm{F}}) = [2|d(\boldsymbol{k}_{\mathrm{F}})|/|\boldsymbol{v}_{\mathrm{F}\perp}(\boldsymbol{k}_{\mathrm{F}})|] \int_0^{|s_0|} ds' \tilde{\Delta}(s')$. We adopt $\tilde{\Delta}(s') = \Delta_0 \tanh(s'/\xi_0)$ as the spatial variation of the pair potential. The coherence length is defined by $\xi_0 = v_{\mathrm{F}\perp}/(\pi \Delta_0)$ with $v_{\mathrm{F}\perp} \equiv \langle |\boldsymbol{v}_{\mathrm{F}\perp}(\boldsymbol{k}_{\mathrm{F}})| \rangle_{\mathrm{FS}}$. Here, we define the field-angular dependent effective coherence length for the later discussions as

$$\xi_{\mathrm{eff}}(\boldsymbol{k}_{\mathrm{F}}) = |\boldsymbol{v}_{\mathrm{F}\perp}(\boldsymbol{k}_{\mathrm{F}})|/[\Delta_0 |d(\boldsymbol{k}_{\mathrm{F}})|]. \tag{3.7}$$

This length scale $\xi_{\mathrm{eff}}(\boldsymbol{k}_{\mathrm{F}})$ characterizes the size of the bound states of the QP with the momentum $\boldsymbol{k}_{\mathrm{F}}$. Figure 3.1 shows the QP trajectories on the plane perpendicular to the magnetic field $\boldsymbol{H}$. The quantities with a prime are those after scattering. s_0 and $|s'_0|$ denote the length between the point that is the nearest from the vortex center on the QP trajectory and the scattering point [69, 73].

3.3 System

In this study, we consider the case in which $\boldsymbol{H}$ is applied parallel to the a-b plane and rotated. The field angle measured from a axis is α_{M}. Here, a, b, and c are crystal axes. When calculating the dependence of ρ_{f} on the magnetic field angle α_{M}, we need a coordinate system fixed to $\boldsymbol{H}$ which is spanned by $\bar{\boldsymbol{a}}_{\mathrm{M}}$, $\bar{\boldsymbol{b}}_{\mathrm{M}}$, and $\bar{\boldsymbol{c}}_{\mathrm{M}}$ (vortex coordinate system). Here, these axes are orthogonal unit vectors with $\bar{\boldsymbol{c}}_{\mathrm{M}}$ set parallel to $\boldsymbol{H}$ ($\bar{\boldsymbol{c}}_{\mathrm{M}} \parallel \boldsymbol{H}$). $\boldsymbol{v}_{\mathrm{F}\perp}$, θ_v, and those with a prime are defined in the vortex coordinates. However, $\boldsymbol{k}_{\mathrm{F}}$ and $\boldsymbol{k}'_{\mathrm{F}}$ are identified by (ϕ_k, θ_k) on a FS in the crystal coordinates spanned by $\bar{\boldsymbol{a}}$, $\bar{\boldsymbol{b}}$ and $\bar{\boldsymbol{c}}$, which characterize the crystal axes. In order to calculate the field-angle α_{M} dependence of ρ_{f}, we need to derive the relation between $\boldsymbol{v}_{\mathrm{F}\perp}$, θ_v, and $\boldsymbol{v}_{\mathrm{F}}$, θ_k [73]. Then, the component of $\boldsymbol{v}_{\mathrm{F}}(\boldsymbol{k}_{\mathrm{F}})$ projected onto the plane perpendicular to $\boldsymbol{H}$ is finally obtained as

$$|\boldsymbol{v}_{\mathrm{F}\perp}(\phi_k, \theta_k)| = |\boldsymbol{v}_{\mathrm{F}}(\phi_k, \theta_k)| \Omega(\phi_k, \theta_k), \tag{3.8}$$

$$\Omega(\phi_k, \theta_k) = \sqrt{\cos^2 \theta_k + \sin^2(\phi_k - \alpha_{\mathrm{M}}) \sin^2 \theta_k}, \tag{3.9}$$

$$\cos \theta_v(\phi_k, \theta_k) = \frac{-|\boldsymbol{v}_{\mathrm{F}}(\phi_k, \theta_k)|}{|\boldsymbol{v}_{\mathrm{F}\perp}(\phi_k, \theta_k)|} \cos \theta_k, \tag{3.10}$$

$$\sin \theta_v(\phi_k, \theta_k) = \frac{|\boldsymbol{v}_{\mathrm{F}}(\phi_k, \theta_k)|}{|\boldsymbol{v}_{\mathrm{F}\perp}(\phi_k, \theta_k)|} \sin(\phi_k - \alpha_{\mathrm{M}}) \sin \theta_k. \tag{3.11}$$

(a) Line-node s-wave   (b) d-wave
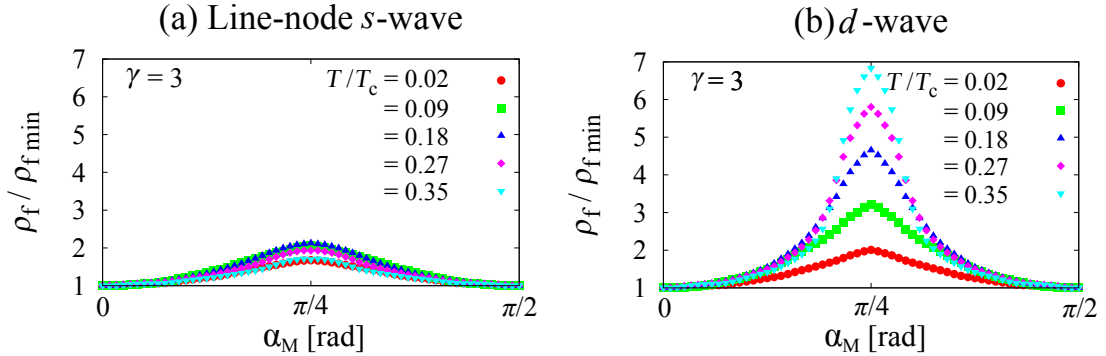
Figure 3.2: Field-angle (α_{M}) dependence of the flux-flow resistivity ρ_{f} in the case of (a) line-node s-wave and (b) d-wave pair for a spheroidal FS ($\gamma = 3$). Each curve indicates different temperature. The vertical axis is normalized by the minimum value of $\rho_{\mathrm{f\ min}}$ for each plot. Reprinted figure with permission from [Yoichi Higashi, Yuki Nagai, Masahiko Machida, and Nobuhiko Hayashi, Physical Review B **88**, 224511 (2013)] Copyright (2013) by the American Physical Society.

Thus, the relation between the vortex coordinate and the crystal coordinate is derived. Here we give the expression of the projected Fermi velocity for an arbitrary anisotropic FS (see Ref. [74] for the expression for a uniaxially anisotropic FS). We have now reached the position where we can perform the numerical integration on FS and calculate the field-angle dependence of Eq. (3.1).

We consider the following two types of the simple pair potential model. One is a line-node s-wave pair: $d(\boldsymbol{k}_{\mathrm{F}}) = |\cos 2\phi_k| \sin^2 \theta_k$. The other is a $d_{x^2-y^2}$-wave one: $d(\boldsymbol{k}_{\mathrm{F}}) = \cos 2\phi_k \sin^2 \theta_k$. Each one has gap nodes from the north pole of the FS to the south one in the $\phi_k = (1 + 2n)\pi/4$ [rad] directions (gap-node directions) with $n = 0, 1, 2, 3$. $\phi_k = n\pi/2$ [rad] directions correspond to anti-node directions. In the momentum space, these two pair potentials have the same anisotropy in their amplitude $|d(\boldsymbol{k}_{\mathrm{F}})|$. However, only the d-wave pair has the sign change and the s-wave pair does not.

Our calculations are performed for a uniaxially anisotropic FS with the mass anisotropy parameter $\gamma = \sqrt{m_c/m_{ab}}$ [74]. m_c and m_{ab} are masses characterizing charge transport along the c-axis and within the $a-b$ plane, respectively.

3.4 Results

3.4.1 Field-angular dependence of flux-flow resistivity

We show numerical results for a uniaxially anisotropic FS with $\gamma = 3$. In Fig. 3.2, we show the field-angle dependence of the flux-flow resistivity $\rho_{\mathrm{f}}(\alpha_{\mathrm{M}})$ for the two pair potential models. As shown in Fig. 3.2(a), in the case of the line-node s-wave pair, a broad maximum appears when $\boldsymbol{H}$ is applied parallel to the gap-node direction ($\alpha_{\mathrm{M}} = \pi/4$). Note that the field-angle dependence of the QP scattering rate $\Gamma(\alpha_{\mathrm{M}})$ has its minimum when $\boldsymbol{H}$ is parallel to the node direction.[73, 74] The oscillation amplitude of $\rho_{\mathrm{f}}(\alpha_{\mathrm{M}})$ remains small compared with the d-wave case when the temperature T is increased. $\rho_{\mathrm{f}}(\alpha_{\mathrm{M}})$ has little dependence on T in the case of the line-node s-wave pair.

On the other hand, in the d-wave case [Fig. 3.2(b)], a sharp maximum appears when $\boldsymbol{H}$ is applied to the gap-node direction. The oscillation amplitude grows with increasing T in contrast to the line-node s-wave pair. This behavior indicates that the peak of $\rho_{\mathrm{f}}(\alpha_{\mathrm{M}})$ has a strong temperature dependence in the d-wave case.

The field-angle dependence of ρ_{f} is quite contrasting between the line-node s-wave pair and the d-wave one. One would question what the reason for this prominent difference is. We consider
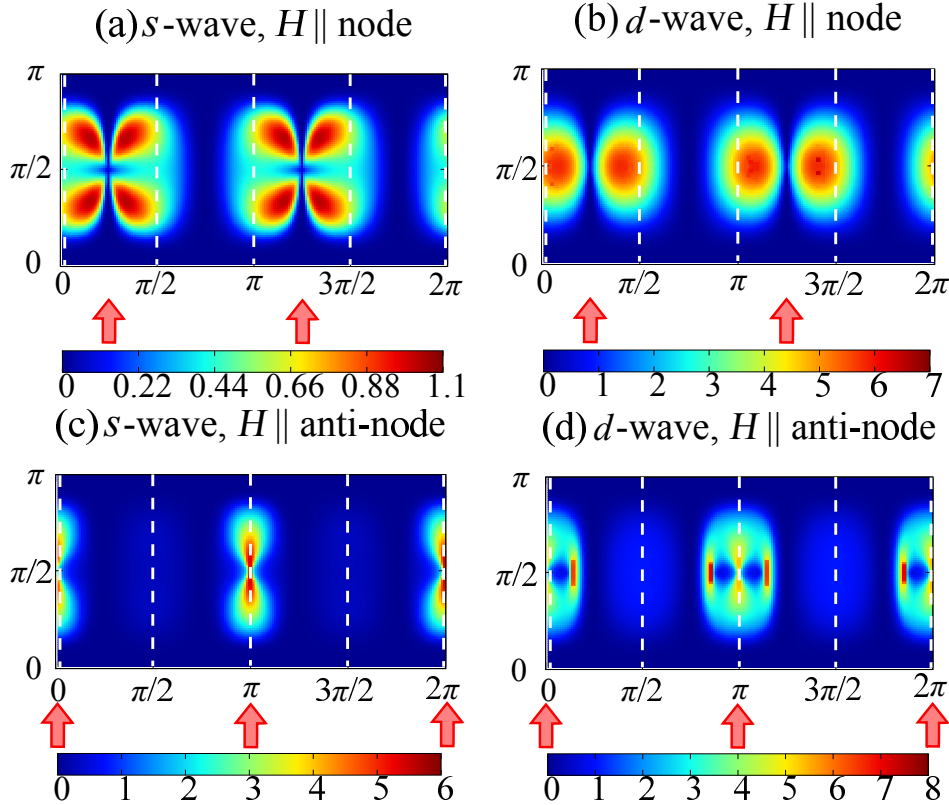
Figure 3.3: $\boldsymbol{k}_{\mathrm{F}}$ dependence of Γ in the case of (a) the line-node s-wave pair when $\boldsymbol{H} \parallel$ the gap-node direction, (b) d-wave pair when $\boldsymbol{H} \parallel$ the gap-node direction, (c) the line-node s-wave pair when $\boldsymbol{H} \parallel$ the anti-node direction and (d) d-wave pair when $\boldsymbol{H} \parallel$ the anti-node direction on a spheroidal FS ($\gamma = 3$). The quasiparticle energy ε is set to $0.2\Delta_0$ in each plot. The vertical and horizontal axes denote the polar angle θ_k and the azimuthal angle ϕ_k respectively. The dotted lines indicate the anti-node directions. The field directions are indicated by arrows. Reprinted figure with permission from [Yoichi Higashi, Yuki Nagai, Masahiko Machida, and Nobuhiko Hayashi, Physical Review B **88**, 224511 (2013)] Copyright (2013) by the American Physical Society.

that this difference comes from whether there is a sign change in the pair potential or not.

3.4.2 Quasiparticle scattering on the Fermi surface

First, we list the characteristics of the $\boldsymbol{k}_{\mathrm{F}}$ dependence of the QP scattering rate $\Gamma(\boldsymbol{k}_{\mathrm{F}})/\Gamma_{\mathrm{n}}$. $\Gamma(\boldsymbol{k}_{\mathrm{F}})/\Gamma_{\mathrm{n}}$ is obtained by integrating Eq. (3.3) with respect to $\boldsymbol{k}'_{\mathrm{F}}$. Next, we explain the behavior of $\Gamma(\alpha_{\mathrm{M}})$.

To clarify why $\rho_{\mathrm{f}}(\alpha_{\mathrm{M}})$ behaves contrastingly between the two pair potential models, we investigate the $\boldsymbol{k}_{\mathrm{F}}$ dependence of Γ first. $\Gamma(\boldsymbol{k}_{\mathrm{F}})/\Gamma_{\mathrm{n}}$ indicates which QPs are easy to be scattered on the FS. We find the following characteristics of the QP scattering: (i) The QPs in the vicinity of the anti-node direction predominantly contribute to Γ, as seen in Figs. 3.3(a)–3.3(d). $\Gamma(\boldsymbol{k}_{\mathrm{F}})/\Gamma_{\mathrm{n}}$ has a higher value around anti-node directions (see around the dotted lines). We describe the physical picture for this characteristics as follows. The QPs flowing in the direction of the gap nodes feel the small amplitude of the pair potential [i.e., small $\Delta_0|d(\boldsymbol{k}_{\mathrm{F}})|$] even in the bulk. Then, $\xi_{\mathrm{eff}}(\boldsymbol{k}_{\mathrm{F}}) = |\boldsymbol{v}_{\mathrm{F}\perp}|/[\Delta_0|d(\boldsymbol{k}_{\mathrm{F}})|]$ becomes large. Thus a vortex core spreads out effectively because of the large effective coherence length ξ_{eff}, and the QP wave function extends outside a vortex core. The wave function is damped exponentially by a factor $\exp[-u(s_0, \boldsymbol{k}_{\mathrm{F}})]$ and Γ for the QPs in the node directions becomes small [see Eq. (3.6)]. On the other hand, the QPs flowing

Table 3.1: The QP scattering types. Reprinted figure with permission from [Yoichi Higashi, Yuki Nagai, Masahiko Machida, and Nobuhiko Hayashi, Physical Review B **88**, 224511 (2013)] Copyright (2013) by the American Physical Society.

	Forward scattering $\Theta(\boldsymbol{k}_{\mathrm{F}}, \boldsymbol{k}'_{\mathrm{F}}) = 0$	Backward scattering $\Theta(\boldsymbol{k}_{\mathrm{F}}, \boldsymbol{k}'_{\mathrm{F}}) = \pi$
sign-conserved	suppressed	small
sign-reversed	enhanced	suppressed

in the direction of the anti-nodes feel the full amplitude of the pair potential (Δ_0). Then, a vortex core gets small effectively because ξ_{eff} becomes small. Hence, the QP wave function is strongly localized inside a vortex core and scattered inside it, giving a large contribution to Γ. (ii) There is the tendency that the QPs in the direction of $\boldsymbol{H}$ are easy to be scattered. As seen in Figs. 3.3(a) and 3.3(b), this property of the QP scattering is confirmed by the fact that the weight of Γ shifts a bit toward the field direction. The tendency is obvious in Figs. 3.3(c) and 3.3(d). The reason why the QPs have above tendency is because $|\boldsymbol{v}_{\mathrm{F}\perp}(\boldsymbol{k}_{\mathrm{F}})|$ of the QPs in the field direction is small and the contribution to Γ becomes large [see Eq. (3.6) and Fig. 3.5]. (iii) The other contribution to Γ is expressed by the coherence factor $C(\boldsymbol{k}_{\mathrm{F}}, \boldsymbol{k}'_{\mathrm{F}})$ [69], which reflects the sign of the pair potential in Eq. (3.4). This characteristic is discussed in detail in Ref. [69]. Here we summarize their results (i.e., the dependence of Γ on the QP scattering types) in Table 3.1.

3.5 Field-angular dependence of quasiparticle scattering rate

First of all, we consider Γ, which is a part of the contribution to ρ_{f} as shown in Eq.(3.1). In the case of the line-node s-wave pair, taking into account the characteristics of the QP scattering (i) – (iii), we can explain qualitatively the behavior of $\Gamma(\alpha_{\mathrm{M}})$. In the line-node s-wave pair, $\Gamma(\alpha_{\mathrm{M}})$ has its minimum when $\boldsymbol{H}$ is applied to the gap-node direction [73, 74]. In this case, according to the factor (iii), the effect of the coherence factor on $\Gamma(\boldsymbol{k}_{\mathrm{F}})/\Gamma_{\mathrm{n}}$ is small. In addition, in the line-node s-wave pair, we confirmed that the coherence factor has no field-angle dependence. Hence, we can neglect the factor (iii) in the line-node s-wave pair.

When $\boldsymbol{H}$ is parallel to the gap-node direction, the weight of $\Gamma(\boldsymbol{k}_{\mathrm{F}})/\Gamma_{\mathrm{n}}$ shifts toward the field direction (i.e., the gap-node direction) due to the factor (ii). Therefore, the QPs around the gap node become easier to be scattered. However, according to the factor (i), the contribution of the QPs in the vicinity of the gap nodes to $\Gamma(\boldsymbol{k}_{\mathrm{F}})/\Gamma_{\mathrm{n}}$ is small. Hence, the large contribution to $\Gamma(\boldsymbol{k}_{\mathrm{F}})/\Gamma_{\mathrm{n}}$ due to the factor (ii) gets small due to the factor (i).

On the other hand, when $\boldsymbol{H}$ is parallel to the anti-node direction, the QPs in the direction of $\boldsymbol{H}$ (i.e., the anti-node direction), which have small $\boldsymbol{v}_{\mathrm{F}\perp}(\boldsymbol{k}_{\mathrm{F}})$, can give a large contribution to $\Gamma(\boldsymbol{k}_{\mathrm{F}})/\Gamma_{\mathrm{n}}$ due to the factor (ii). In this case, contrary to the case of $\boldsymbol{H}$ parallel to the node direction, Γ remains large due to the factor (i). As a result of the above consideration, the minimum of $\Gamma(\alpha_{\mathrm{M}})$ appears when $\boldsymbol{H}$ is parallel to the gap-node direction.

In the case of the d-wave pair, the backward scattering is suppressed (see Table 3.1) since the coherence factor becomes zero and the scattering point is far from the vortex core. However, the forward scattering with the sign change of pair potential is enhanced (see Table 3.1). So the coherence factor gives the large contribution to $\Gamma(\boldsymbol{k}_{\mathrm{F}})/\Gamma_{\mathrm{n}}$. In Fig. 3.4, we show the field-angle dependences of $\langle\langle C(\boldsymbol{k}_{\mathrm{F}}, \boldsymbol{k}'_{\mathrm{F}})D(\boldsymbol{k}_{\mathrm{F}}, \boldsymbol{k}'_{\mathrm{F}})\rangle_{\mathrm{FS}'}\rangle_{\mathrm{FS}}$, which is the part of $\Gamma(\varepsilon)/\Gamma_{\mathrm{n}}$ containing the coherence factor $C(\boldsymbol{k}_{\mathrm{F}}, \boldsymbol{k}'_{\mathrm{F}})$. We also calculate the field-angle dependences of $\langle\langle F(\varepsilon, \boldsymbol{k}_{\mathrm{F}}, \boldsymbol{k}'_{\mathrm{F}})\rangle_{\mathrm{FS}'}\rangle_{\mathrm{FS}}$, which does not contain the coherence factor. When $\boldsymbol{H}$ is parallel to the node direction, $\langle\langle C(\boldsymbol{k}_{\mathrm{F}}, \boldsymbol{k}'_{\mathrm{F}})D(\boldsymbol{k}_{\mathrm{F}}, \boldsymbol{k}'_{\mathrm{F}})\rangle_{\mathrm{FS}'}\rangle_{\mathrm{FS}}$ shows a sharp maximum. On the other hand, $\langle\langle F(\varepsilon, \boldsymbol{k}_{\mathrm{F}}, \boldsymbol{k}'_{\mathrm{F}})\rangle_{\mathrm{FS}'}\rangle_{\mathrm{FS}}$ shows little field-angle dependence. This sharp maximum reproduces the behavior of $\Gamma(\alpha_{\mathrm{M}})$ in the d-wave case [73, 74].

Let us explain the physical picture of the QP scattering rate in the d-wave case. First of all, we should note that the intensity of the forward scattering is the important factor of the QP
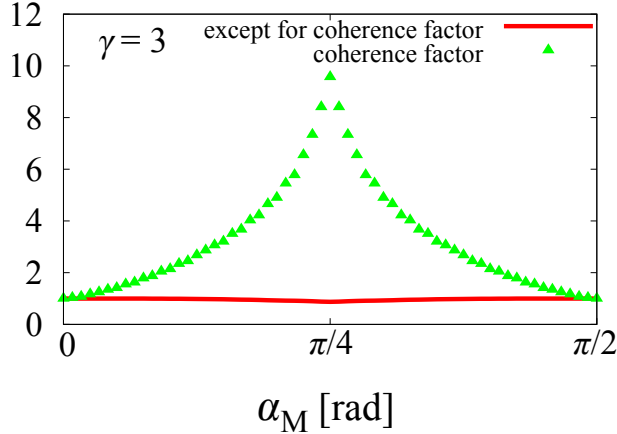
Figure 3.4: Field-angle (α_{M}) dependences of the part of Γ containing the coherence factor and the other part of it for the d-wave pair with the spheroidal FS. The vertical axis is normalized by the minimum value. Reprinted figure with permission from [Yoichi Higashi, Yuki Nagai, Masahiko Machida, and Nobuhiko Hayashi, Physical Review B **88**, 224511 (2013)] Copyright (2013) by the American Physical Society.

scattering around a vortex, since the forward scatterings occur when the scattering point is near the vortex center (i.e., the QP scattering occurs inside a vortex core), as shown in Fig. 3.1. Thus, we consider the field-angle dependence of the intensity of the forward scattering. We note that the intensity of the forward scattering becomes larger upon decreasing the effective coherence length $\xi_{\mathrm{eff}}(\boldsymbol{k}_{\mathrm{F}})$. The effective coherence length $\xi_{\mathrm{eff}}(\boldsymbol{k}_{\mathrm{F}})$ defined by Eq. (3.7) is proportional to the projected Fermi velocity $\boldsymbol{v}_{\mathrm{F}\perp}(\boldsymbol{k}_{\mathrm{F}})$ and is inversely proportional to the amplitude of a pair potential $\Delta_0|d(\boldsymbol{k}_{\mathrm{F}})|$. The minimum effective coherence length is zero when the Fermi velocity $\boldsymbol{v}_{\mathrm{F}}(\boldsymbol{k}_{\mathrm{F}})$ is parallel to $\boldsymbol{H}$ [i.e., $\boldsymbol{v}_{\mathrm{F}\perp}(\boldsymbol{k}_{\mathrm{F}})$ becomes zero]. As shown in Fig. 3.3, the intensity of $\Gamma(\boldsymbol{k}_{\mathrm{F}})$ becomes large in the region where $\boldsymbol{v}_{\mathrm{F}\perp}(\boldsymbol{k}_{\mathrm{F}})$ becomes small. This is the reason for the factor (ii).

The most important factor of the intensity of the forward scattering is the factor (iii). As shown in Table 3.1, the sign-conserved forward scattering is suppressed even when the effective coherence length becomes small. Therefore, the sign-reversed forward scatterings with the small effective coherence length dominantly contribute to the QP scattering rate in the d-wave case. When $\boldsymbol{H}$ is parallel to the gap-node direction, we have confirmed numerically that the forward scattering is realized by calculating the contribution of anti-nodal QPs to $\Gamma(\varepsilon, \boldsymbol{k}'_{\mathrm{F}}, \alpha_{\mathrm{M}} = \pi/4)$. As shown in Fig. 3.5, the forward scattering occurs through the QP scattering in the parallel direction of $\boldsymbol{H}$ when $\boldsymbol{H}$ is parallel to the gap-node direction. Moreover, this QP scattering process is sign-reversing, since the quasiparticles with $\boldsymbol{v}_{\mathrm{F}}$ are scattered across the gap-node perpendicular to $\boldsymbol{H}$. Hence, the sign-reversed forward scattering occurs when $\boldsymbol{H}$ is parallel to the gap-node direction even in a single-band superconductor.

On the other hand, when $\boldsymbol{H}$ is parallel to the anti-node direction, it was revealed through the same analysis that although the sign-reversed scattering occurs, not only the forward scattering but also the backward scattering occurs. As a result of the above discussion, the quasiparticle scattering rate is enhanced when $\boldsymbol{H}$ is parallel to the gap-node direction in the d-wave case.

3.6 Field-angular dependence of flux-flow resistivity

The other contribution to ρ_{f} is $\omega_0(\boldsymbol{k}_{\mathrm{F}})$. When $\Gamma(\varepsilon, \boldsymbol{k}_{\mathrm{F}}) = \mathrm{const.}$, the field angle dependence of $\omega_0(\boldsymbol{k}_{\mathrm{F}})$ for a spheroidal FS is not qualitatively different from that for an isotropic FS [64]. When $\omega_0(\boldsymbol{k}_{\mathrm{F}}) = \mathrm{const.}$, $\rho_{\mathrm{f}}(T) \propto \Gamma(\varepsilon = k_{\mathrm{B}}T)$. In the d-wave case, the dependence of $\omega_0(\boldsymbol{k}_{\mathrm{F}})$ on the field-angle makes the behavior of $\Gamma(\alpha_{\mathrm{M}})$ stand out. As a result, $\rho_{\mathrm{f}}(\alpha_{\mathrm{M}})$ has a sharp maximum when $\boldsymbol{H}$ is parallel to the gap-node direction. On the other hand, in the s-wave case, the field angle dependence of $\omega_0(\boldsymbol{k}_{\mathrm{F}})$ makes the oscillation amplitude of $\Gamma(\alpha_{\mathrm{M}})$ inverted and $\rho_{\mathrm{f}}(\alpha_{\mathrm{M}})$ has
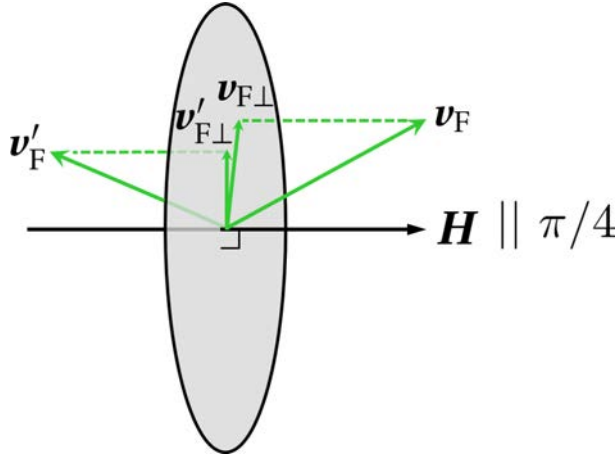
Figure 3.5: Schematic figure of the forward QP scattering, which is characterized by the angle between the projections of the Fermi velocities onto the plane perpendicular to an in-plane magnetic field $\boldsymbol{H}$. Reprinted figure with permission from [Yoichi Higashi, Yuki Nagai, Masahiko Machida, and Nobuhiko Hayashi, Physical Review B **88**, 224511 (2013)] Copyright (2013) by the American Physical Society.

its broad maximum when $\boldsymbol{H}$ is parallel to the gap-node direction.

3.7 Effect of anisotropic Fermi surface on the flux-flow resistivity

In this subsection, we investigate effects of in-plane FS anisotropy on the field-angle dependence of flux-flow resistivity $\rho_{\mathrm{f}}(\alpha_{\mathrm{M}})$. Most materials have the anisotropy in their FS reflecting the anisotropy of crystal structures. Thus, it is more realistic to investigate $\rho_{\mathrm{f}}(\alpha_{\mathrm{M}})$ in the case of anisotropic FS. We consider two model FSs with in-plane anisotropy and numerically calculate $\rho_{\mathrm{f}}(\alpha_{\mathrm{M}})$ for those FSs with changing the anisotropy of FS. Our numerical results show that one can detect the gap-node direction by measuring ρ_{f} under rotating magnetic field even if the FS has an anisotropy.

We consider two model FSs I, II with in-plane anisotropy depicted in Fig. 3.6. The model FS I is characterized by the energy dispersion $\epsilon_{\mathrm{I}}(\boldsymbol{k}) = -\mu_{\mathrm{I}} - 2t\left\{\cos(k_x a) + \cos(k_y a)\right\} + k_z^2/(2m)$ [see Fig. 3.6(a)], where t and a are the hopping integral and the lattice constant, respectively. μ_{I} is the chemical potential. The dispersion in the k_x-k_y plane is given by the the tight-binding (TB) model and that in the k_z direction is free electron model. As characteristics of the TB model, there are Van Hove singularities in the direction of $(\pi, 0)$ and $(0, \pi)$, at which $|\boldsymbol{\nabla}_{\boldsymbol{k}}\epsilon(\boldsymbol{k})| = 0$ [75, 76]. In addition to this point, the anisotropy of the FS grows larger gradually with increasing the chemical potential below the half filling. The model FS II is given by the anisotropic dispersion $\epsilon_{\mathrm{II}}(\boldsymbol{k}) = -\mu_{\mathrm{II}} + 1/(2m)\left\{k_x^2 + k_y^2 + a^2(k_x^4 + k_y^4)/2 + 3a^2 k_x^2 k_y^2 + k_z^2\right\}$ [77, 78] [see Fig. 3.6(b)]. m is the mass of charge. In numerical calculation, we set the parameter $mta^2 = 1$.

For an isotropic FS, the position on the FS is identified by the azimuthal and the polar angle (ϕ_k, θ_k). However, in anisotropic FSs, it is identified by ϕ_k, θ_k and the Fermi radius $|\boldsymbol{k}_{\mathrm{F}}(\phi_k, \theta_k)|$. We can parametrize the Fermi wave numbers in spherical coordinates: $k_{\mathrm{F}x} = |\boldsymbol{k}_{\mathrm{F}}(\phi_k, \theta_k)|\cos\phi_k \sin\theta_k$, $k_{\mathrm{F}y} = |\boldsymbol{k}_{\mathrm{F}}(\phi_k, \theta_k)|\sin\phi_k \sin\theta_k$, $k_{\mathrm{F}z} = |\boldsymbol{k}_{\mathrm{F}}(\phi_k, \theta_k)|\cos\theta_k$. Substituting these Fermi wave numbers into the above two dispersions $\epsilon_{\mathrm{I}}(\boldsymbol{k})$ and $\epsilon_{\mathrm{II}}(\boldsymbol{k})$, and using a bisection method, we can determine numerically $|\boldsymbol{k}_{\mathrm{F}}(\phi_k, \theta_k)|$ such that $\epsilon(\boldsymbol{k}) = 0$ (see Fig. 3.6).

For FS I, the absolute value of the Fermi velocity is

$$|\boldsymbol{v}_{\mathrm{F}}(\phi_k, \theta_k)| = 2ta\sqrt{\sin^2(k_{\mathrm{F}x}a) + \sin^2(k_{\mathrm{F}y}a) + \frac{1}{4(mta^2)^2}(k_{\mathrm{F}z}a)^2} \tag{3.12}$$
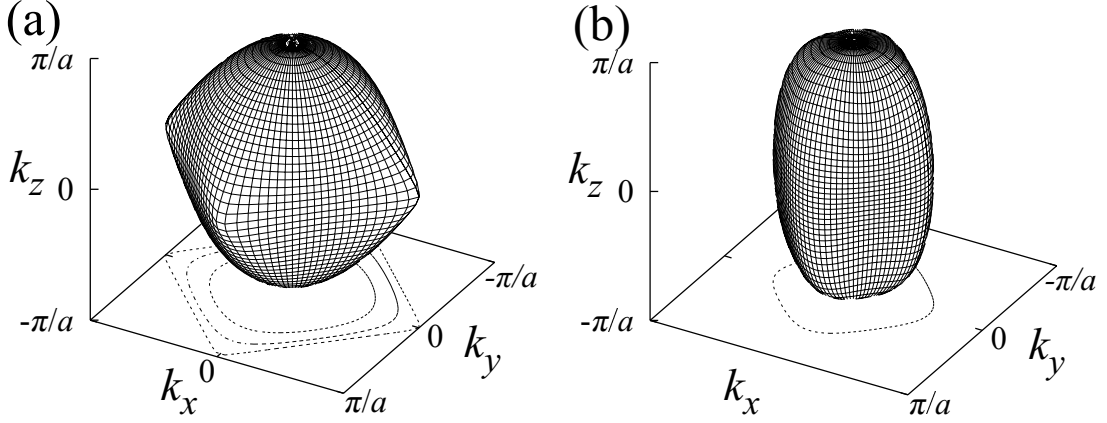
Figure 3.6: Anisotropic Fermi surfaces characterized by the energy dispersion $\epsilon_{\mathrm{I}}(\boldsymbol{k})$ (a) and $\epsilon_{\mathrm{II}}(\boldsymbol{k})$ (b). The contour plots projected on to the k_x-k_y plane indicate the Fermi surfaces at $k_z = 0$, which correspond to $\mu_{\mathrm{I}} = -0.01t, -0.5t$ and $-1.5t$ from the outside to the inside (a) and $\mu_{\mathrm{II}} = 9t$ (b).

and for FS II,

$$|\boldsymbol{v}_{\mathrm{F}}(\phi_k, \theta_k)| = \frac{1}{m} \sqrt{k_{\mathrm{F}x}^2 \left(1 + a^2 k_{\mathrm{F}x}^2 + 3a^2 k_{\mathrm{F}y}^2\right)^2 + k_{\mathrm{F}y}^2 \left(1 + a^2 k_{\mathrm{F}y}^2 + 3a^2 k_{\mathrm{F}x}^2\right)^2 + k_{\mathrm{F}z}^2}. \quad (3.13)$$

When integrating Eq. (3.1) numerically, we need a relation between $\boldsymbol{v}_{\mathrm{F}\perp}(\phi_k, \theta_k)$ and $\boldsymbol{v}_{\mathrm{F}}(\phi_k, \theta_k)$ [73]. The component of $\boldsymbol{v}_{\mathrm{F}}(\phi_k, \theta_k)$ projected onto the plane perpendicular to $\boldsymbol{H}$ is given by the same formulae as Eq. (3.8)-(3.11),

$$|\boldsymbol{v}_{\mathrm{F}\perp}(\phi_k, \theta_k)| = |\boldsymbol{v}_{\mathrm{F}}(\phi_k, \theta_k)| \sqrt{\cos^2 \theta_k + \sin^2 \theta_k \sin^2(\phi_k - \alpha_{\mathrm{M}})}, \quad (3.14)$$

$$\cos \theta_v(\boldsymbol{k}_{\mathrm{F}}) = -\frac{|\boldsymbol{v}_{\mathrm{F}}(\phi_k, \theta_k)|}{|\boldsymbol{v}_{\mathrm{F}\perp}(\phi_k, \theta_k)|} \cos \theta_k, \quad (3.15)$$

$$\sin \theta_v(\boldsymbol{k}_{\mathrm{F}}) = \frac{|\boldsymbol{v}_{\mathrm{F}}(\phi_k, \theta_k)|}{|\boldsymbol{v}_{\mathrm{F}\perp}(\phi_k, \theta_k)|} \sin \theta_k \sin(\phi_k - \alpha_{\mathrm{M}}), \quad (3.16)$$

where $\theta_v(\boldsymbol{k}_{\mathrm{F}})$ is the angle of the QP trajectory measured from the $\boldsymbol{a}_{\mathrm{M}}$-axis. The $\boldsymbol{a}_{\mathrm{M}}$ - $\boldsymbol{b}_{\mathrm{M}}$ plane is perpendicular to $\boldsymbol{H}$ ($\boldsymbol{c}_{\mathrm{M}} \parallel \boldsymbol{H}$). α_{M} is the magnetic field angle measured from the $(\pi, 0)$ direction.

In order to investigate the relation between the anisotropy of the pair potential and that of the FSs, we consider the following four model pair potentials: (i) Line-node $s_{|x^2-y^2|}$-wave: $d(\boldsymbol{k}_{\mathrm{F}}) = |\cos(2\phi_k) \sin^2 \theta_k|$, (ii) Line-node $s_{|xy|}$-wave: $d(\boldsymbol{k}_{\mathrm{F}}) = |\sin(2\phi_k) \sin^2 \theta_k|$, (iii) $d_{x^2-y^2}$-wave: $d(\boldsymbol{k}_{\mathrm{F}}) = \cos(2\phi_k) \sin^2 \theta_k$, and (iv) d_{xy}-wave: $d(\boldsymbol{k}_{\mathrm{F}}) = \sin(2\phi_k) \sin^2 \theta_k$. While $s_{|x^2-y^2|}$ ($s_{|xy|}$)-wave and $d_{x^2-y^2}$ (d_{xy})-wave pair potentials have the same anisotropy, only $d_{x^2-y^2}$ (d_{xy})-wave one has the sign change. $s_{|x^2-y^2|}$ ($d_{x^2-y^2}$)-wave pair potential coincides with $s_{|xy|}$ (d_{xy})-wave one when the pair potential is rotated by $\pi/4$ [rad].

In Figs. 3.7 and 3.8, we show the numerical results of the field-angle α_{M} dependence of the flux-flow resistivity ρ_{f} for the model FS I and II. The inset shows the schematic figure of the pair potential on the anisotropic FS. We fix the temperature in this calculation at $T = 0.35 T_{\mathrm{c}}$. Each plot corresponds to different chemical potential. For the energy dispersion II, the chemical potential μ_{II} is fixed to $\mu_{\mathrm{II}} = 9t$.

In Figs. 3.7(a) and 3.7(b), we can see that ρ_{f} has the maximum value when $\boldsymbol{H}$ is applied parallel to the gap-node direction. This behavior in the $s_{|x^2-y^2|}$-wave pair is consistent with the result for both an isotropic [64] and an uniaxially anisotropic FS (Fig. 3.2). The same behavior is seen also for the $d_{x^2-y^2}$ and the d_{xy}-wave pair [see Fig. 3.8(a) and 3.8(b)]. However, the oscillation amplitude of $\rho_{\mathrm{f}}(\alpha_{\mathrm{M}})$ for the $d_{x^2-y^2}$ and the d_{xy}-wave pair becomes larger than that
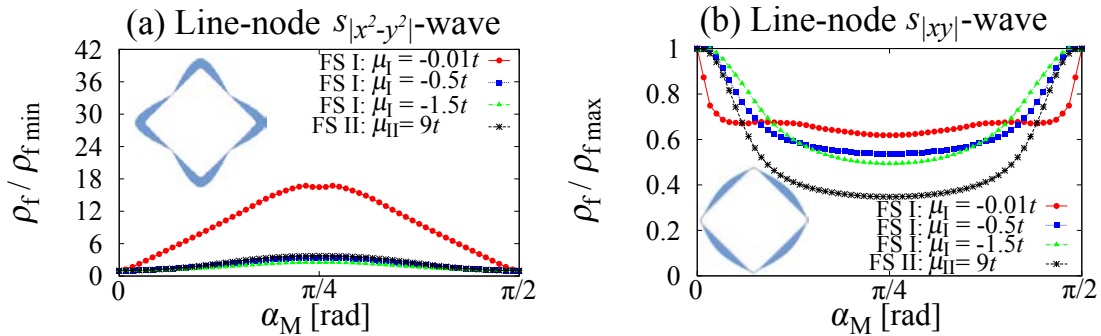
Figure 3.7: The field angle α_{M} dependence of the flux-flow resistivity ρ_{f} in the case of the (a) line-node $s_{|x^2-y^2|}$-wave pair and the (b) line-node $s_{|xy|}$-wave one. The temperature is set to $T = 0.35 T_{\mathrm{c}}$. Each curve is plotted for the different chemical potential. For FS II, the chemical potential is set to $\mu_{\mathrm{II}} = 9t$. The vertical axis is normalized by (a) minimum value and (b) maximum value for each curve. Reprinted figure with permission from [Yoichi Higashi, Yuki Nagai, Masahiko Machida, and Nobuhiko Hayashi, Physics Procedia **45**, 137-140 (2013)] Copyright (2013) by Elsevier.

for the $s_{|x^2-y^2|}$ and the $s_{|xy|}$-wave one. In addition, for the $d_{x^2-y^2}$-wave pair, a rather sharper peak appears when $\boldsymbol{H} \parallel \pi/4$. These characteristics originate from the sign-change in the pair potential because its amplitude is the same between the $s_{|x^2-y^2|}$ and the $d_{x^2-y^2}$ (or the $s_{|xy|}$ and the d_{xy})-wave pair.

We notice that the curve of $\rho_{\mathrm{f}}(\alpha_{\mathrm{M}})$ for FS I approaches the curve for FS II with decreasing the FS anisotropy ($\mu_{\mathrm{I}} = -0.01t \to -1.5t$) in Figs. 3.7 and 3.8. The anisotropy of FS II with $\mu_{\mathrm{II}} = 9t$ is almost the same as that of FS I with $\mu_{\mathrm{I}} = -1.5t$. The cusp-like sharp peak appearing in an isotropic FS for the $d_{x^2-y^2}$-wave pair [64] is not observed in the case of these in-plane anisotropic FSs. For any pairing states, when $\boldsymbol{H} \parallel$ gap node, the peak becomes sharp with increasing the anisotropy of the FS. We consider that this behavior comes from the anisotropy of the FS. The important point is that one can detect the gap-node direction from the field-angle dependence of the flux-flow resistivity even if there is an anisotropy of a FS. That is, a peak of $\rho_{\mathrm{f}}(\alpha_{\mathrm{M}})$ appears in the gap-node direction irrespective of a FS anisotropy.

3.8 Discussions

Finally, we comment on the experimental condition for measuring the flux-flow resistivity under a rotating magnetic field. Our theory is based on the vortex bound states formed inside a vortex core. Therefore, an extremely two-dimensional system, in which a Josephson vortex is formed parallel to the layer, is beyond our theoretical framework. However, we should note that our method can be applied to iron-pnictides, which have a warped cylindrical Fermi surface such as that found in 11-compounds (FeSe or FeTe) and 122-compounds [BaFe$_2$(As$_{1-x}$P$_x$)$_2$], since the angular-resolved specific heat and thermal conductivity measurements have successfully detected the gap minima in FeSe$_{0.45}$Te$_{0.55}$ [79] and the position of the gap-nodes in BaFe$_2$(As$_{0.67}$P$_{0.33}$)$_2$ [80], respectively, under a rotated magnetic field within the basal plane. In layered organic compounds κ-(ET)$_2$Cu(NCS)$_2$, in-plane field angular dependence of the Josephson-vortex flow resistance has already been measured by Yasuzuka *et al.* [22, 23], but in a three-dimensional system, measurement of the flux-flow resistivity has not been performed yet. An anisotropic FS might affect the $\rho_{\mathrm{f}}(\alpha_{\mathrm{M}})$. However, as shown in Ref. [81] (Section 3.7), the behavior of $\rho_{\mathrm{f}}(\alpha_{\mathrm{M}})$ in the case of the in-plane anisotropic FS is not qualitatively different from that in the isotropic FS case within the range of our model calculations. When considering multiband superconductors such as iron-based superconductors, we need to take into account the contribution from holelike FS to the flux-flow resistivity in addition to that from electronlike FS [60]. In this study, we consider the contribution only from electronlike FS. The multiband effect on the flux-flow resistivity
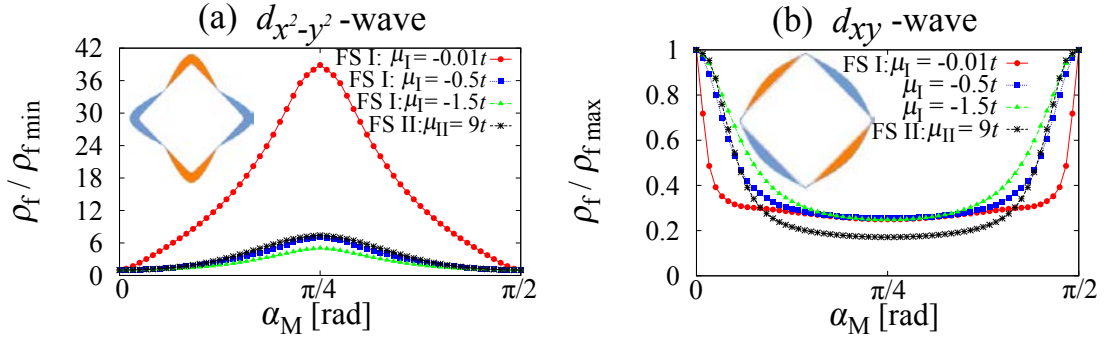
Figure 3.8: The field angle α_{M} dependence of the flux-flow resistivity ρ_{f} in the case of the (a) $d_{|x^2-y^2|}$-wave pair and the (b) $d_{|xy|}$-wave one. The temperature is set to $T = 0.35T_{\mathrm{c}}$. Each curve is plotted for the different chemical potential. For FS II, the chemical potential is set to $\mu_{\mathrm{II}} = 9t$. The vertical axis is normalized by (a) minimum value and (b) maximum value for each curve. Reprinted figure with permission from [Yoichi Higashi, Yuki Nagai, Masahiko Machida, and Nobuhiko Hayashi, Physics Procedia **45**, 137-140 (2013)] Copyright (2013) by Elsevier.

is left for future study.

3.9 Conclusion

In conclusion, we theoretically studied the in-plane magnetic field-angle dependence of the flux-flow resistivity for both a uniaxially anisotropic FS and an in-plane anisotropic one. We showed that the measurement of the flux-flow resistivity changing the field direction within the a-b plane can detect both the position of the gap nodes and the sign change of the pairing potential. One can estimate the flux-flow resistivity by means of microwaves. Instead of fabricating a junction, one can obtain the information on the phase of the pair potential by measuring the microwave surface impedance under a rotating magnetic field.

Chapter 4

Impurity Effect on the Local Density of States around a Vortex in Noncentrosymmetric Superconductors

We numerically study the effect of non-magnetic impurities on the vortex bound states in non-centrosymmetric systems. The local density of states (LDOS) around a vortex is calculated by means of the quasiclassical Green's function method. We find that the zero energy peak of the LDOS splits off with increasing the impurity scattering rate in the non-self-consistent Born approximation. We also demonstrate that the mixing of the p-wave component of the order parameter causes the impurity effect different from that in the bulk, in which the impurity effect on the LDOS dependes on the spin-orbit coupling due to the interband scattering.

4.1 Introduction

Much attention has been focused on the superconductivity in noncentrosymmetric systems because of its novel superconductivity due to spin-orbit coupling (SOC). Recently, active investigations have been conducted on the inhomogeneous superconducting state in noncentrosymmetric systems such as the helical phase in a magnetic field [45, 82, 83, 84], the vortex state [85, 10, 86, 30], and the exotic superconducting state in locally noncentrosymmetric systems [87, 42, 43].

In this study, we investigate the non-magnetic impurity scattering effect on the local density of states (LDOS) around a single vortex. Impurity effects on the vortex core structure in noncentrosymmetric systems can differ from the simple two-gap systems because there is SOC in this system. So unusual phenomena are expected in the LDOS inside a vortex core. There are several previous studies for the impurity effect on the noncentrosymmetric superconductivity in the bulk without vortices [28, 34, 32, 31, 33]. However, there is no research on the impurity effect in spatially inhomogeneous situations such as vortex state in noncentrosymmetric systems.

Through our formulation using the quasiclassical Green's function method, it turned out that the form of the impurity self-energy around a vortex is quite different from that in the bulk. This comes from the effect of the superflow on the impurity self-energy. In addition, the Green's function cannot be separated with respect to each Fermi surface (FS) split due to the Rashba-type SOC in the presence of both impurities and vortices. This fact might also influence the impurity effect on the vortex core structure.

In this study, we numerically investigated the effect of non-magnetic impurities on the LDOS around a vortex. We found that the zero-energy peak (ZEP) of the LDOS splits off with increasing the impurity scattering rate. We give the rough physical interpretation for the numerical results.

4.2 Formulation

The noncentrosymmetricity of the system induces the anitisymmetric SOC and permits the mixing of the Cooper pair wave function with different parity. We assume the Rashba-type SOC, which is described as $\boldsymbol{g}_k = \sqrt{3/2}(-k_y, k_x, 0)/k_F$ by the orbital vector $\boldsymbol{g}_k$. k_F is the Fermi wave number. We consider a single vortex line along the z axis situated at the origin ($\boldsymbol{r} = 0$). We assume that the FS is spherical. The lack of spatial inversion symmetry of the system is detrimental to spin-triplet state [20]. However, the spin-triplet state is not suppressed under the particular situation in which $\boldsymbol{d}_k \parallel \boldsymbol{g}_k$ [17]. Then we consider the parity mixing of the Cooper pair.

The parity-mixed pairing state is expressed as $\hat{\Delta}(\boldsymbol{r}, \tilde{\boldsymbol{k}}) = [\Psi(\boldsymbol{r})\hat{\sigma}_0 + \boldsymbol{d}_k(\boldsymbol{r}) \cdot \hat{\boldsymbol{\sigma}}] i\hat{\sigma}_y = [\Psi\hat{\sigma}_0 + \Delta(-\tilde{k}_y\hat{\sigma}_x + \tilde{k}_x\hat{\sigma}_y)]f(r)\exp[i\phi_r]i\hat{\sigma}_y$, where the spin-singlet s-wave component $\Psi(\boldsymbol{r})$, the d vector $\boldsymbol{d}_k = \Delta(\boldsymbol{r})(-\tilde{k}_y, \tilde{k}_x, 0)$ with the unit vector $\tilde{\boldsymbol{k}} = (\tilde{k}_x, \tilde{k}_y, \tilde{k}_z) = (\cos\phi_k \sin\theta_k, \sin\phi_k \sin\theta_k, \cos\theta_k)$, $\Psi(\Delta)$ is the bulk amplitude of the pair potential for singlet (triplet) component, $\hat{\boldsymbol{\sigma}} = (\hat{\sigma}_x, \hat{\sigma}_y, \hat{\sigma}_z)$ is the vector consisting of the Pauli spin matrices and $\hat{\sigma}_0$ is the unit matrix in the spin space. We assume that the both components of the pair potential have the same real space profile around a vortex and set $f(r) = r/\sqrt{r^2 + \xi_0^2}$. Here, $\xi_0 = v_F/T_c$ is the coherence length, T_c is the superconducting critical temperature, $v_F(= |\boldsymbol{v}_F|)$ is the Fermi velocity. In this study, we does not solve the gap equations for the pair potentials $\Psi(\boldsymbol{r})$ and $\Delta(\boldsymbol{r})$ self-consistently. We conduct the numerical calculation for zero temperature and take into account the effect of temperature through the energy smearing factor η.

In order to obtain the LDOS and the impurity self-energy, we consider the following quasiclassical Green's function, which is defined in the particle-hole space.

$$\check{g}(\boldsymbol{r}, \tilde{\boldsymbol{k}}, i\omega_n) = -i\pi \begin{pmatrix} \hat{g} & i\hat{f} \\ -i\hat{\bar{f}} & -\hat{\bar{g}} \end{pmatrix}. \tag{4.1}$$

Here, ω_n is the Matsubara frequency. $\hat{}$ denotes the 2×2 matrix in the spin space and $\check{}$ denotes the 4×4 matrix in the particle-hole and spin space. The Eilenberger equation with the SOC term and impurity self-energy is given as [49, 88, 89, 90, 91]

$$i\boldsymbol{v}_F(\tilde{\boldsymbol{k}}) \cdot \boldsymbol{\nabla}\check{g}(\boldsymbol{r}, \tilde{\boldsymbol{k}}, i\omega_n) + \left[i\omega_n\check{\tau}_3 - \check{\Delta} - \check{\Sigma} - \alpha\check{\boldsymbol{g}}_k \cdot \check{\boldsymbol{S}}, \ \check{g}(\boldsymbol{r}, \tilde{\boldsymbol{k}}, i\omega_n)\right] = \check{0}, \tag{4.2}$$

where

$$\check{\tau}_3 = \begin{pmatrix} \hat{\sigma}_0 & \hat{0} \\ \hat{0} & -\hat{\sigma}_0 \end{pmatrix}, \quad \check{\boldsymbol{S}} = \begin{pmatrix} \hat{\boldsymbol{\sigma}} & \hat{0} \\ \hat{0} & \hat{\boldsymbol{\sigma}}^{\mathrm{tr}} \end{pmatrix}, \quad \hat{\boldsymbol{\sigma}}^{\mathrm{tr}} = -\hat{\sigma}_y\hat{\boldsymbol{\sigma}}\hat{\sigma}_y, \tag{4.3}$$

$$\check{\boldsymbol{g}}_k = \begin{pmatrix} \boldsymbol{g}_k\hat{\sigma}_0 & \hat{0} \\ \hat{0} & \boldsymbol{g}_{-k}\hat{\sigma}_0 \end{pmatrix}, \quad \check{\Delta} = \begin{pmatrix} \hat{0} & \hat{\Delta}(\boldsymbol{r}, \tilde{\boldsymbol{k}}) \\ -\hat{\Delta}^\dagger(\boldsymbol{r}, \tilde{\boldsymbol{k}}) & \hat{0} \end{pmatrix}. \tag{4.4}$$

Here, α is the strength of the SOC. $\boldsymbol{g}_k = \sqrt{3/2}(-\tilde{k}_y, \tilde{k}_x, 0)$, which is odd in k (i.e., $\boldsymbol{g}_{-k} = -\boldsymbol{g}_k$). We use the units in which $\hbar = k_B = 1$. The quasiclassical Green's function satisfies the normalization condition $\check{g}^2 = -\pi^2\check{\tau}_0$ with the 4×4 unit matrix $\check{\tau}_0$. The bracket $[\cdots, \cdots]$ is a commutator.

The Eilenberger equation is separated into two equations without spin degree of freedom using the band basis both in the clean vortex state [30] and in the bulk clean system [29, 92]. The normal-state Hamiltonian in the clean limit, which is a 2×2 matrix in the spin space, becomes diagonal in the band basis. The off-diagonal components of the quasiclassical Green's function decay to zero around a vortex and the quasiclassical Green's function in the band basis becomes diagonal in the spin space (see the appendix of Ref. [29]). Each diagonal component obeys the Eilenberger equation, which is defined on the two FSs split due to the SOC. Then, we can solve the Eilenberger equation without the SOC term with respect to each FS in the clean limit. This situation is not changed in the presence of impurities in the bulk.

However, the quasiclassical Green's function is not diagonal in the band basis in the presence of both impurities and vortices. Therefore the Eilenberger equation is not separated into two

equations with respect to each FS. Thus, we use the orbital basis, in which the spin quantization axis is oriented parallel to the z axis. Under this basis, we transform Eq. (4.2) into the two matrix Riccati type differential equations, which is the first-order differential equations (see Appendix C). Then we obtain the stable numerical solution solving the Eq. (C.9) and (C.10) by means of the adaptive stepsize control Runge-Kutta method [93].

In this study, we investigate the s-wave non-magnetic impurity scattering in the Born limit (We set the scattering phase shift exactly zero). In this limit, the impurity self-energy is given as [27, 72]

$$\check{\Sigma}(\boldsymbol{r}, E) = \frac{\Gamma_{\mathrm{n}}}{\pi} \left\langle \check{g}(\boldsymbol{r}, \tilde{\boldsymbol{k}}, i\omega_n \rightarrow E + i\eta) \right\rangle_{\tilde{\boldsymbol{k}}}, \tag{4.5}$$

$$= \Gamma_{\mathrm{n}} \begin{pmatrix} -i\langle \hat{g} \rangle_{\tilde{\boldsymbol{k}}} & \langle \hat{f} \rangle_{\tilde{\boldsymbol{k}}} \\ -\langle \hat{\bar{f}} \rangle_{\tilde{\boldsymbol{k}}} & i\langle \hat{\bar{g}} \rangle_{\tilde{\boldsymbol{k}}} \end{pmatrix}, \tag{4.6}$$

where Γ_{n} is the impurity scattering rate in the normal state, $\langle \cdots \rangle_{\tilde{\boldsymbol{k}}}$ denotes the average over the FS and $\check{\Sigma} \equiv \{\hat{\Sigma}_{ij}\}_{i,j=1,2}$. Now we consider the system with the rotational symmetry about a vortex line. In the clean limit, the parity mixing pair potential has a form $\Delta_{\mathrm{I,II}}(r, \phi_r; \theta_k) = [\Psi(r) \pm \Delta(r) \sin\theta_k] \exp[i\phi_r]$ around a vortex using the band basis [30]. These forms of the pair potentials have the θ_k dependence only. We assume that the pairing state does not change with non-magnetic impurities. Under an axial rotation about a vortex line, the pair potential has the azimuthal angle dependence in the form of the phase factor in the real space. From Eq. (C.9) and (C.10), we can see that the anomalous self-energies $\hat{\Sigma}_{12,21}$ have the same phase factor as the pair potentials, whereas the normal self-energies $\hat{\Sigma}_{11,22}$ are invariant under the axial rotation. Thus the anomalous self-energies $\hat{\Sigma}_{12,21}$ have the following ϕ_r dependence [72]: $\hat{\Sigma}_{12,21}(r, \phi_r, E) = \hat{\Sigma}_{12,21}(r, E) \exp[\pm i\phi_r]$. The plus (minus) sign corresponds to $\hat{\Sigma}_{12}(\hat{\Sigma}_{21})$. In the actual numerical calculation, the self-energies are discretely calculated in a radial r direction. Thus they are linearly-interpolated in this direction. As for the direction of an azimuthal angle, the self-energies have the continuous ϕ_r dependence.

The LDOS per spin is obtained from

$$N(\boldsymbol{r}, E) = -\frac{N_{\mathrm{F}}}{2} \frac{1}{\pi} \left\langle \mathrm{Im} \left[\mathrm{Tr}\ \hat{g}(\boldsymbol{r}, \tilde{\boldsymbol{k}}, i\omega_n \rightarrow E + i\eta) \right] \right\rangle_{\tilde{\boldsymbol{k}}}, \tag{4.7}$$

where N_{F} is the density of states per spin at the Fermi level in the normal state.

4.3 Results

Throughout this section, we set $\alpha'/T_{\mathrm{c}} = 1$ with $\alpha' = \sqrt{3/2}\alpha$. We call the Born approximation using the quasiclassical Green's function in the clean limit the *bare Born approximation*. Besides, we call the Born approximation in which the spatial profiles of the self-energies are determined self-consistetly the *self-consistent Born approximation* in this study.

4.3.1 Bare Born approximation with equal point spacing

We show in Fig. 4.1(a) the energy dependence of the LDOS at the vortex center for several values of the impurity scattering rate Γ_{n} for the s-wave case ($\Psi/T_{\mathrm{c}} = 1, \Delta/T_{\mathrm{c}} = 0$). $\Gamma_{\mathrm{n}}/T_{\mathrm{c}}$ is roughly estimated of the order of ξ_0/l. l is the mean free path. In the clean limit ($\Gamma_{\mathrm{n}}/T_{\mathrm{c}} = 0$), the peak of the LDOS is seen at the zero energy. In the presence of impurities, the ZEP splits into two peaks. We confirmed that the split of the ZEP does not occur for $\alpha'/T_{\mathrm{c}} = 0$. The splitting width becomes larger and the peak height decreases with increasing the impurity scattering rate Γ_{n}. For $\Gamma_{\mathrm{n}} = 0.7T_{\mathrm{c}}$, the value of the zero energy LDOS at the vortex center equals to the normal state density of states N_{F}. In Fig. 4.1(b), we show the energy and the spatial profile of the LDOS inside a vortex core for $\Gamma_{\mathrm{n}} = 0.3T_{\mathrm{c}}$. We see clearly that the ZEP of the LDOS splits off at the vortex center. Far from the vortex center, the zero energy density of states decays to zero and the fully opened superconducting energy gap appears in the bulk, which is understood from the
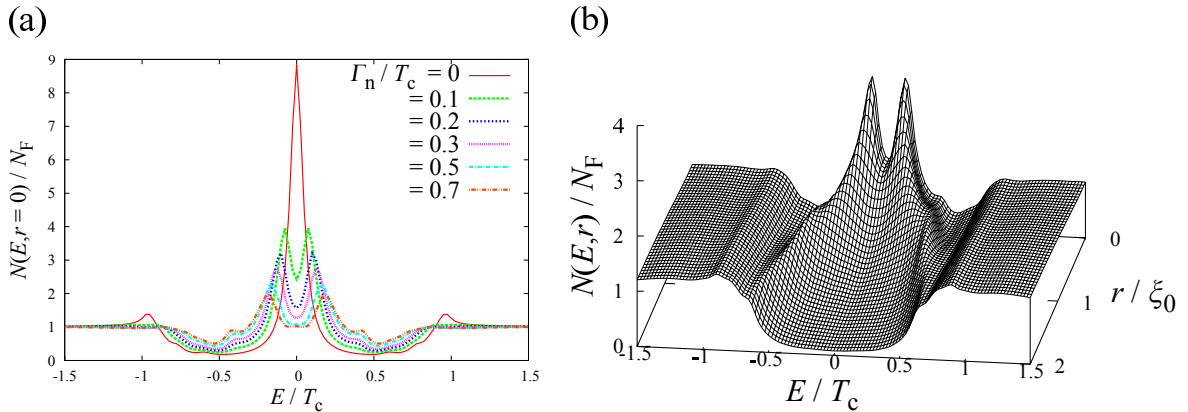
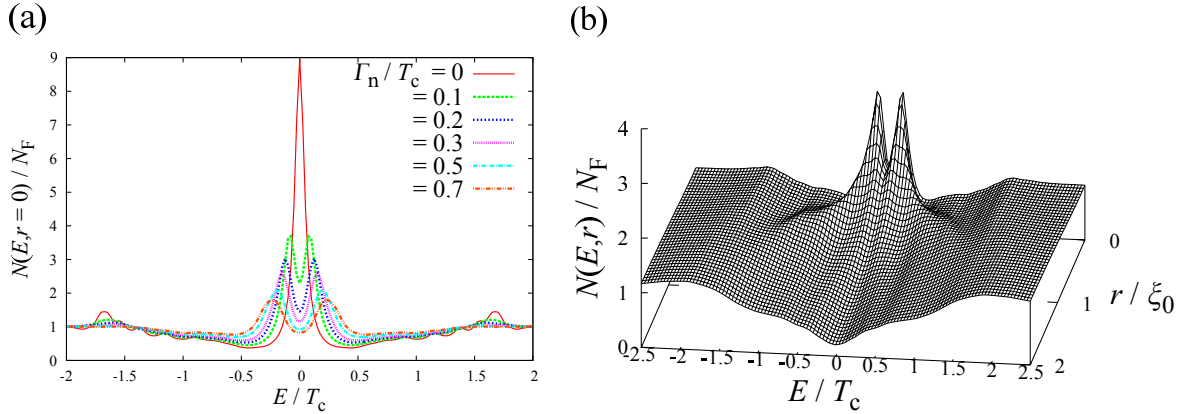(a)   (b)

Figure 4.1: s-wave case. The energy smearing factor η is set to $0.05T_c$. (a) The energy dependence of the local density of states at the vortex center for several values of the impurity scattering rate Γ_n. (b) The local density of states within a vortex core for $\Gamma_n = 0.3T_c$. Reprinted figure with permission from [Yoichi Higashi, Yuki Nagai, and Nobuhiko Hayashi, JPS Conference Proceedings **3**, 015003 (2014)] Copyright (2014) by the Physical Society of Japan.

Anderson's theorem for non-magnetic impurities [19, 94]. We can see that the ridge lines of the vortex bound states approach the gap edges of the s-wave component $E/T_c = \Psi/T_c = \pm 1$.

As shown in Fig. 4.2(a), the ZEP splits off also in the case of the $s + p$-wave ($\Psi/T_c : \Delta/T_c = 0.7 : 1.4$). The ridge lines related to the vortex bound states of the quasiparticles on the split FS are broaden due to impurity scattering [see Fig. 4.2(b)]. We cannot observe the two-gap like quasiparticle spectra within a core, which is seen in the clean limit [30]. Within the superconducting gap energy, there exists the non-zero density of states which comes from excitations in the vicinity of the horizontal line nodes. Nodes can appear under $\Psi < \Delta$ [92], which corresponds to the present condition.

4.3.2 Bare Born approximation with dense point spacing near the vortex center

In the subsection 4.3.1, we calculated the impurity self-energies at equally-spaced discrete points along the radial line. However, we calculated the impurity self-energy on only a few points within a vortex core ($r < \xi_0$). We could not calculate the impurity self-energy around a vortex core with sufficient accuracy. Then, we take the dense point spacing near the vortex center and take the sparse point spacing far from a vortex in subsections 4.3.2 and 4.3.3. In the same way as Ref. [95], we adopt $r_i = \tilde{r}[\exp(R_i) - 1]$ as the function producing non-equally-spaced discrete points r_i. Here, R_i is equally-spaced discrete point. We set $\tilde{r} = 0.001\xi_0$ and the cutoff distance $r_c = 10\xi_0$.

We show the LDOS around a vortex core for s-wave [Fig. 4.3(a)], $s + p$-wave ($\Psi/T_c : \Delta/T_c = 0.7 : 1.4$) [Fig. 4.3(b)] and $s + p$-wave ($\Psi/T_c : \Delta/T_c = 0.2 : 0.8$) pair [Figs. 4.3(c) and 4.3(d)]. The impurity scattering rate is set to $\Gamma_n/T_c = 0.3$. The zero energy peak is split in the bare Born approximation (BBA) with non-equally point spacing. This feature is the same as that in the BBA with equal point spacing (Figs. 4.1 and 4.2), but the detailed structure of the LDOS is different between them. The split zero energy peak is seen when changing the mixing ratio of the order parameter [Fig. 4.3(b) and 4.3(c)]. The splitting width becomes larger with increasing Γ_n. The LDOS structure in the $s + p$-wave case for $\alpha'/T_c = 1$ [Fig. 4.3(c)] is subtly different from that for $\alpha'/T_c = 30$ [Fig. 4.3(d)] and not altered qualitatively for two dimensional Fermi surface. This α dependence is discussed in section 4.4.

(a)   (b)

Figure 4.2: $s + p$-wave case. The energy smearing factor η is set to $0.05 T_{\rm c}$. (a) The energy dependence of the local density of states at the vortex center for several values of the impurity scattering rate $\Gamma_{\rm n}$. (b) The local density of states within a vortex core for $\Gamma_{\rm n} = 0.3 T_{\rm c}$. Reprinted figure with permission from [Yoichi Higashi, Yuki Nagai, and Nobuhiko Hayashi, JPS Conference Proceedings **3**, 015003 (2014)] Copyright (2014) by the Physical Society of Japan.

4.3.3 Self-consistent Born approximation

Figs. 4.4(a)-4.4(c) and Figs. 4.4(d)-4.4(f) show the LDOS around a vortex core for s-wave and $s+p$-wave, respectively. The split zero energy peak disappears in the self-consistent Born approximation for both pairing states. The zero energy peak is suppressed gradually with increasing the impurity scattering rate from $\Gamma_{\rm n}/T_{\rm c} = 0.01$ to 1 for both pairing states. These LDOS structures are not altered for $\alpha'/T_{\rm c} = 50$ for the s-wave pair. However, for $s + p$-wave pair, the impurity effect on the LDOS depends on α. The LDOS profile in the $s + p$-wave case for $\alpha/T_{\rm c} = 30$ is nearly identical to that for $\alpha/T_{\rm c} = 1$, but there is a difference. The zero energy LDOS value at the vortex center for $\alpha/T_{\rm c} = 30$ is $N(E = 0, r = 0)/N_{\rm F} \approx 2.232$, whereas that for $\alpha/T_{\rm c} = 1$ is $N(E = 0, r = 0)/N_{\rm F} \approx 2.218$. This α dependence is discussed in section 4.4.

4.4 Discussions

4.4.1 Dependence of the spin-orbit coupling strength

The impurity self-energies around a vortex core with use of the bare Born approximation are expressed by the Green's function in the clean limit. The normal and anomalous self-energies in the orbital basis are given as

$$\hat{\Sigma}^0_{11} = -i\Gamma_{\rm n}\frac{1}{2}\left[\langle g_{\rm I} + g_{\rm II}\rangle_{\tilde{\boldsymbol{k}}}\hat{\sigma}_0 + \langle (g_{\rm I} - g_{\rm II})\bar{\boldsymbol{g}}_k \cdot \hat{\boldsymbol{\sigma}}\rangle_{\tilde{\boldsymbol{k}}}\right], \tag{4.8}$$

$$\hat{\Sigma}^0_{12} = \Gamma_{\rm n}\frac{1}{2}\left[\langle f_{\rm I} + f_{\rm II}\rangle_{\tilde{\boldsymbol{k}}}\hat{\sigma}_0 + \langle (f_{\rm I} - f_{\rm II})\bar{\boldsymbol{g}}_k \cdot \hat{\boldsymbol{\sigma}}\rangle_{\tilde{\boldsymbol{k}}}\right], \tag{4.9}$$

which are different from the formulae in the bulk (see Appendix D), but are identical with those if there is no p-wave component (i.e., there is the s-wave component only) and the difference of the DOS between FS I and II. In this case, $g_{\rm I} = g_{\rm II}$ and $f_{\rm I} = f_{\rm II}$. Here $g_{\rm I,II}$ and $f_{\rm I,II}$ are the normal and anomalous quasiclassical Green's function in the band basis, respectively. $\bar{\boldsymbol{g}}_k = \boldsymbol{g}_k/|\boldsymbol{g}_k|$. Thus, the impurity self-energies are proportional to $\hat{\sigma}_0$,

$$\hat{\Sigma}^0_{11} = -i\Gamma_{\rm n}\frac{1}{2}\langle g_{\rm I} + g_{\rm II}\rangle_{\tilde{\boldsymbol{k}}}\hat{\sigma}_0 = -i\Gamma_{\rm n}\langle g_{\rm I}\rangle_{\tilde{\boldsymbol{k}}}\hat{\sigma}_0 = -i\Gamma_{\rm n}\langle \hat{g}_0\rangle_{\tilde{\boldsymbol{k}}}, \tag{4.10}$$

$$\hat{\Sigma}^0_{12} = \Gamma_{\rm n}\frac{1}{2}\langle f_{\rm I} + f_{\rm II}\rangle_{\tilde{\boldsymbol{k}}}\hat{\sigma}_0 = \Gamma_{\rm n}\langle f_{\rm I}\rangle_{\tilde{\boldsymbol{k}}}\hat{\sigma}_0 = \Gamma_{\rm n}\langle \hat{f}_0\rangle_{\tilde{\boldsymbol{k}}}, \tag{4.11}$$
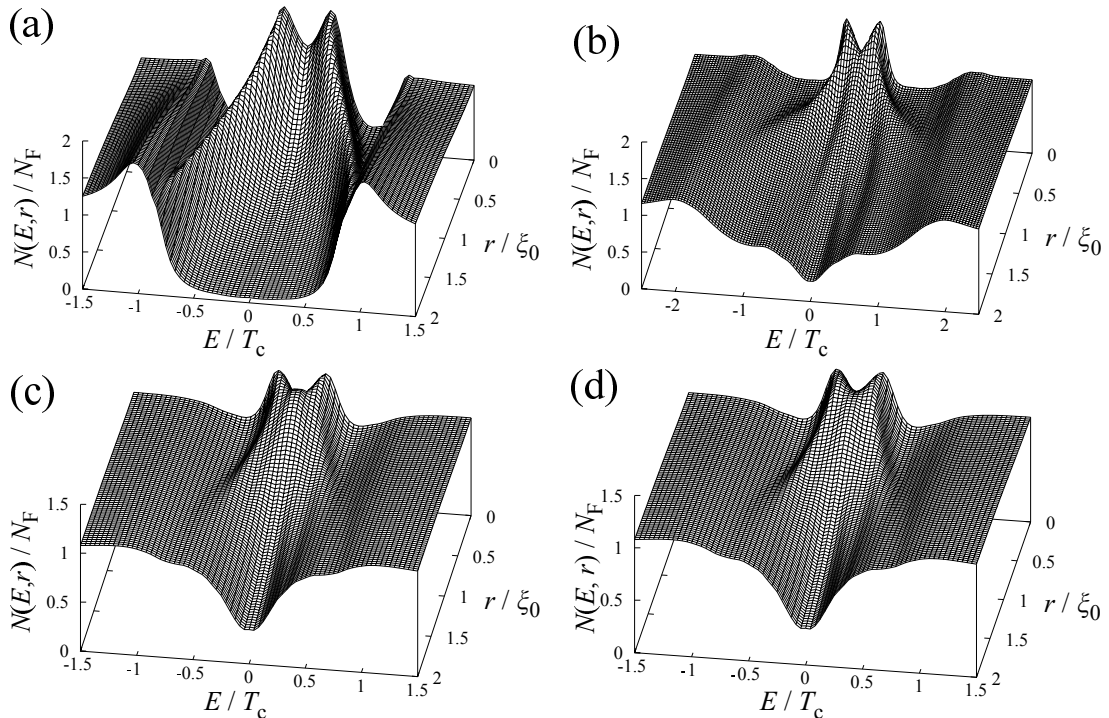
Figure 4.3: The local density of states within a vortex core for s-wave ($\Psi/T_c = 1$) (a), $s+p$-wave ($\Psi/T_c : \Delta/T_c = 0.7 : 1.4$) (b), $s+p$-wave ($\Psi/T_c : \Delta/T_c = 0.2 : 0.8$) case (c) and (d). The impurity scattering rate is set to $\Gamma_n/T_c = 0.3$. Other parameters are $\alpha'/T_c = 1$ (a)-(c), $\alpha'/T_c = 30$ (d) and $\eta/T_c = 0.05$.

which are same as the impurity self-energies in the bulk (see Appendix D). We have confirmed also numerically that the impurity self-energies become diagonal in spin space. g_I, f_I and g_{II}, f_{II} are the solutions of the Eilenberger equation on the split FSs I and II, respectively. The solutions are obtained by the Riccati transformation as $g_{I,II} = (1 - a_{I,II}b_{I,II})(1 + a_{I,II}b_{I,II})^{-1}$, $f_{I,II} = 2a_{I,II}(1 + a_{I,II}b_{I,II})^{-1}$. Hence, in the case of the s-wave pair, the Eilenberger equations are separated into the two equations defined on the split FSs I and II, respectively in the band basis. The procedure is the same as Appendix D. So the SOC strength α does not appear in the Eilenberger equation and then the impurity effect on the LDOS is independent of α in the s-wave case.

However, in the presence of the p-wave component, the second terms in Eqs. (4.8) and (4.9) do not disappear. Then the finite off-diagonal components in spin space appear, which we have confirmed also by numerical calculations (see Appendix E). The finite off-diagonal components result in the appearance of the off-diagonal components of the impurity self-energies in the band basis for $s+p$-wave pairing. Thereby the Eilenberger equations are not separated with respect to each band split due to the SOC. In this case the SOC terms remain in the Eilenberger equations. So it is expected that the impurity effect on the LDOS depends on α for $s+p$-wave pair. Indeed, as shown in Figs. 4.3(c) and 4.3(d), the impurity effect on the LDOS depends on α. The zero energy values of the LDOS at the vortex center are $N(E = 0, r = 0)/N_F \approx 0.980$ for $\alpha'/T_c = 1$ [Fig. 4.3(c)] and $N(E = 0, r = 0)/N_F \approx 1.033$ for $\alpha'/T_c = 30$ [Fig. 4.3(c)], respectively. The α dependence of the zero energy peak is understood as follows. Now the FS is split due to the SOC, which is described by the two band picture in the band basis (see subsection 1.3.2). As discussed above, there is the interband scattering for $s+p$-wave pairing. For small α, the splitting width of the FS is small. Then, the interband scattering easily occurs. However, for larger α, the splitting width of the FS becomes larger, since it is proportional to α. Then, the quasiparticles cannot be easily scattered between the largely split FSs, which are away from each other in momentum space. Thus, the interband scattering is suppressed. Consequently, the effect of the impurity
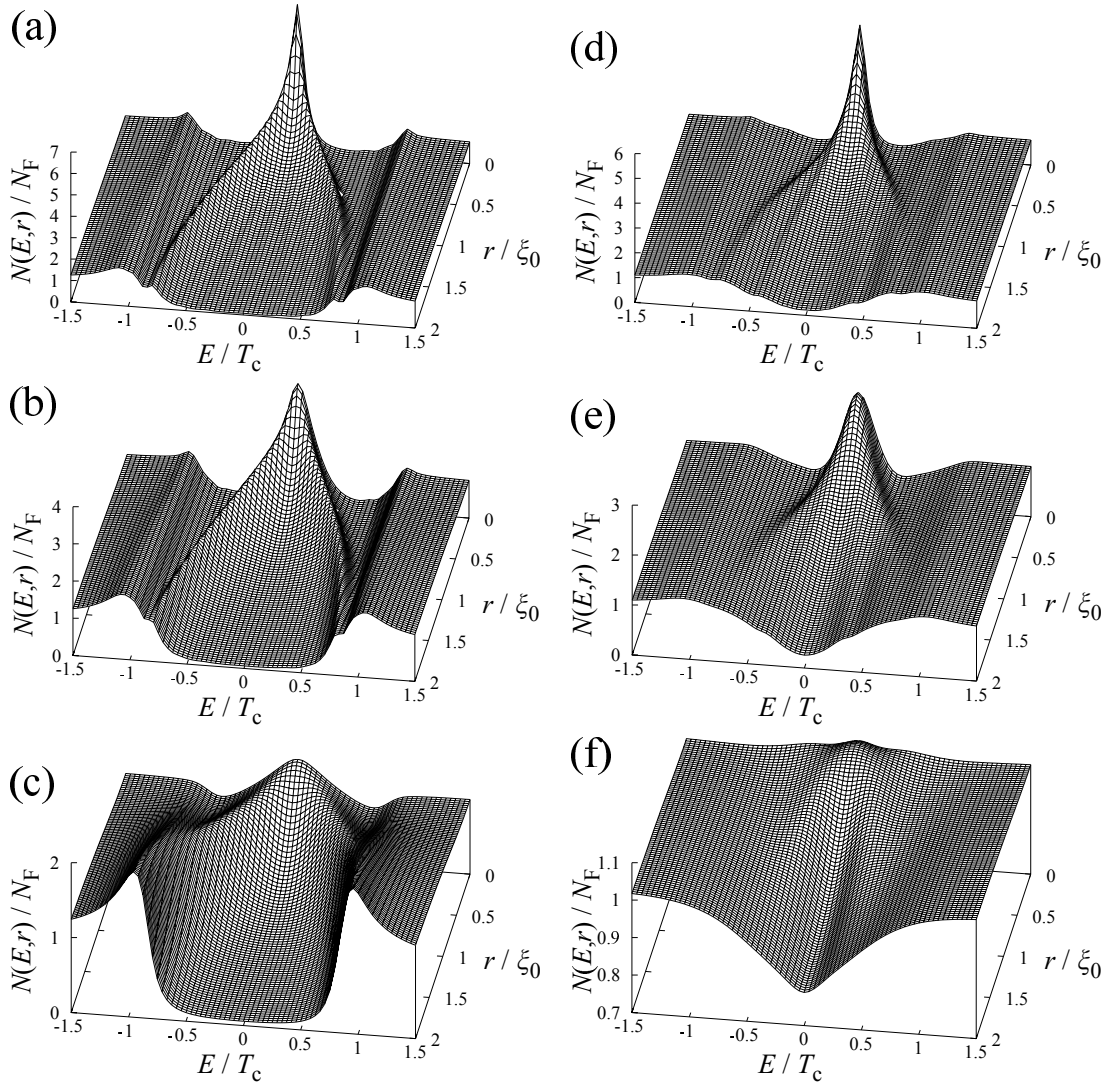
Figure 4.4: The local density of states within a vortex core for s-wave case ($\Psi/T_\mathrm{c} = 1$) (a)-(c) and for $s + p$-wave case ($\Psi/T_\mathrm{c} : \Delta/T_\mathrm{c} = 0.2 : 0.8$) (d)-(f). The impurity scattering rate is set to $\Gamma_\mathrm{n}/T_\mathrm{c} = 0.01$ (a), (d); 0.1 (b), (e); and 1 (c), (f). Other parameters are $\alpha'/T_\mathrm{c} = 1$, $\eta/T_\mathrm{c} = 0.05$.

scattering on the LDOS around a vortex core becomes small for large α, and then the suppression of the zero energy peak due to impurity scattering also becomes small.

The α dependence of the impurity scattering effect for $s + p$-wave pair is seen also in the self-consistent Born approximation. However, α dependence of the impurity scattering effect on the LDOS structure is subtle. In the quasiclassical regime, the Fermi energy E_F is sufficiently large measured from the bottom of energy bands, and then $T_\mathrm{c} \ll \alpha \ll E_\mathrm{F}$ in general. So the energy scale of the FS splitting α is much smaller than that of the electron system E_F. Thus, the effect of the FS splitting is limited. We consider that this might be a reason of the subtle α dependence of the impurity scattering effect on the LDOS structure for $s + p$-wave pair.

4.4.2   Split of the zero energy peak in the bare Born approximation

As shown in Fig. 4.3, the p-wave component of the order parameter is not essential for the split of the ZEP, since the ZEP splits even in the case of the s-wave pairing. Then, we consider the impurity effect in the case of the s-wave. As shown in the subsection 4.4.1, in this case, the
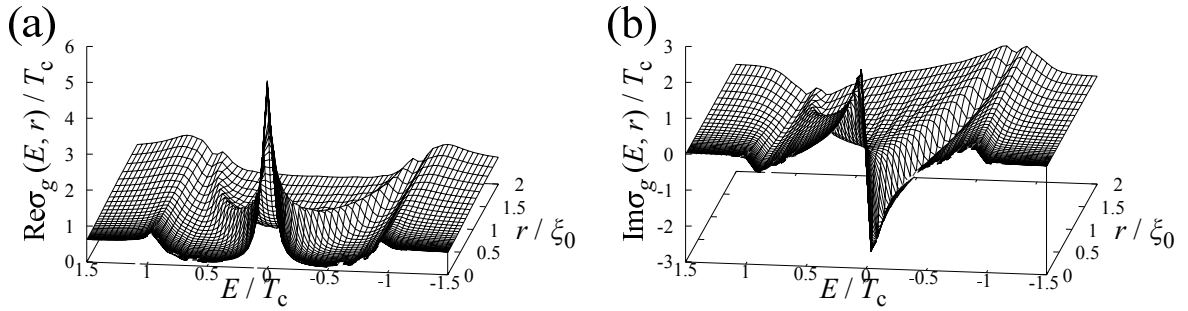
Figure 4.5: The real part (a) and the imaginary part (b) of the normal self-energy $\sigma_g(E, r)$ for s-wave pair. The impurity scattering rate is set to $\Gamma_\mathrm{n} = 0.7 T_\mathrm{c}$ and the energy smearing factor η is set to $0.05 T_\mathrm{c}$.

impurity self-energy is the same as that in the bulk (see Appendix D). The normal self-energies couple with the Matsubara frequency in the Eilenberger equation. At the electron (hole) side, the Matsubara frequency is modified to $\omega_n + \sigma_g(E, r)$ $[-(\omega_n + \sigma_g(E, r))]$, where

$$\sigma_g(i\omega_n \to E + i\eta, r) = \Gamma_\mathrm{n}\left[\langle g_\mathrm{I}(E, r, \tilde{\boldsymbol{k}})\rangle_{\tilde{\boldsymbol{k}}} - \langle \bar{g}_\mathrm{I}(E, r, \tilde{\boldsymbol{k}})\rangle_{\tilde{\boldsymbol{k}}}\right]. \tag{4.12}$$

We assume that the density of states at the Fermi level in the normal state is the same on each split FS. We show the numerically calculated $\sigma_g(E, r)$ in Fig.4.5. Considering from $i(\omega_n + \sigma_g) \to E - \mathrm{Im}\sigma_g + i(\eta + \mathrm{Re}\sigma_g)$, the imaginary part of σ_g [Fig. 4.5(b)] contributes to the energy shift and the real part [Fig. 4.5(a)] contributes to the broadening of the quasiparticle spectra. In Fig. 4.5(a), at the zero energy, the large value of $\mathrm{Re}\sigma_g$ gives the large broadening of the zero energy LDOS, and the peak of $\mathrm{Im}\sigma_g$ at the low energy region contributes to the energy shift of the zero energy peak. Then, the zero energy peak splits into the broad two peaks in Fig. 4.3(a).

4.5 Conclusion

In conclusion, we calculated the local density of states around a vortex core in the presence of non-magnetic impurities in noncentrosymmetric systems. We found that the zero-energy peak of the vortex bound states splits off with increasing the impurity scattering rate for both s-wave and $s + p$-wave pairing state in the bare Born approximation. We also showed that the impurity effect in the vicinity of a vortex core is independent of the spin-orbit coupling (SOC) for an s-wave pairing in the bare Born approximation, which is the same feature as that in the bulk, namely, the Eilenberger equation is separated into the two equations defined on the each split Fermi surface. This is the case with the impurity scattering effect in the self-consistent Born approximation. On the other hand, in an $s + p$-wave pairing, we found that the impurity effect can depend on the SOC in the bare and the self-consistent Born approximation. This means that the Eilenberger equation is not separated into the two equations, since the interband impurity scattering occurs around a vortex core for the $s + p$-wave pairing.

Chapter 5

Vortex Core Structure in Multilayered Rashba Superconductors

We numerically study the electronic structure of a single vortex in two dimensional superconducting bilayer systems within the range of the mean-field theory. The lack of local inversion symmetry in the system is taken into account through the layer dependent Rashba spin-orbit coupling. The spatial profiles of the pair potential and the local quasiparticle density of states are calculated in the clean spin-singlet superconductor on the basis of the quasiclassical theory. In particular, we discuss the characteristic core structure in the pair-density wave state, which is spatially modulated exotic superconducting phase in a high magnetic field.

5.1 Introduction

Intensive studies on locally noncentrosymmetric systems (LNCS) has been conducted [39, 40]. The LNCS are realized in various materials such as multilayered cuprates [96], the doped topological insulator $Cu_xBi_2Se_3$ [97], the pnictide superconductor SrPtAs [98] and so on. Especially, the heavy-fermion $CeCoIn_5/YbCoIn_5$ superlattice is fabricated [99] and the artificial control of the inversion symmetry breaking was realized recently [100]. Therefore, one can seek experimentally the theoretically predicted exotic superconducting phase in a magnetic field [42, 43]. The inhomogeneity due to a magnetic field is not taken into account in the existing theoretical researches on the superconductivity in LNCS [42, 43]. However, the exotic superconducting phase stabilizes in a magnetic field. So understanding the vortex states in LNCS is necessary. The observation of quasiparticle states in the vicinity of a vortex gives us a lot of information on the exotic superconducting phase. We focus on the exotic superconducting phase called the pair-density wave (PDW) phase, which is stabilized in a high magnetic field perpendicular to the layers [42]. In the PDW phase, the phase of the superconducting order parameter changes by π between the two layers, whereas no phase difference of the order parameter in the BCS phase in a low magnetic field. In this study, we investigate the vortex core structure of the PDW and the BCS phases, and try to obtain the characteristics of the PDW phase.

5.2 Formulation

We consider the multilayered system characterized by the layer-dependent spin-orbit coupling (SOC) strength α_m with the layer index m. In this paper, the number of the layer is fixed to $N = 2$. The layer dependence of the SOC $(\alpha_1, \alpha_2) = (\alpha, -\alpha)$ reflects the local noncentrosymmetricity of the system [87]. We assume the simple form of the Rashba type SOC described by $\boldsymbol{g}(\boldsymbol{k}) = (-k_y, k_x, 0)/k_F$, which satisfies the normalization condition $\langle \boldsymbol{g}(\boldsymbol{k}) \rangle_{\boldsymbol{k}} = 1$ on the two dimensional

Fermi surface (FS). k_F is the Fermi wave number and $\langle \cdots \rangle_{\boldsymbol{k}}$ is the average over the FS.

We consider spin-singlet s-wave pairing states within the layer. The pairing potential in spin space is expressed as $\Delta_{s_1 s_2}(\boldsymbol{r}) = \Delta(\boldsymbol{r})(i\sigma_y)_{s_1 s_2}$. We assume that the spatial variation of the pair potential $\Delta(\boldsymbol{r})$ is the same in each layer. Then, the pair potential is expressed as $\hat{\Delta}(\boldsymbol{r}) = \Delta(\boldsymbol{r})i\sigma_y \otimes D$, where D is the $N \times N$ diagonal matrix in the space composed of the layer (band) degree of freedom. In the case of $N = 2$, $D = \mathrm{diag}(1, s)$ with $s = 1$ for the BCS state and $s = -1$ for the PDW one. $\hat{\cdot}$ denotes the $2N \times 2N$ matrix in the spin and band space. A vortex line perpendicular to the two dimensional superconducting layer has the form, $\Delta(\boldsymbol{r}) = |\Delta(r)|\exp(i\phi_r)$ in each layer.

In this study, we consider the superconductor in which the paramagnetic pair breaking effect is dominant. In addition, we assume the system is in the type-II limit and neglect the vector potential. Then, we incorporate only the paramagnetic pair breaking effect into the quasiclassical theory through the Zeeman term. There is three factors which split the 4-fold degenerated FS. The spin degeneracy is lifted by both the SOC and the Zeeman field $\mu_B H$, and the band degeneracy is lifted by the interlayer hopping $t_\perp$. We assume that the strength of these three factors is sufficiently weak and incorporate them into the quasiclassical theory as perturbations. In this situation, the split of the FS is small and the difference of the Fermi velocity between the weakly split FS is negligibly small. So we can put $\boldsymbol{v}_F = v_F \tilde{\boldsymbol{k}}$. Then, we can expand the quasiclassical approximation described in Ref. [29] into the multilayered system.

The quasiclassical Green's function depends on the direction $\tilde{\boldsymbol{k}} = (\cos \phi_k, \sin \phi_k)$ with the azimuthal angle ϕ_k and is written as a $4N \times 4N$ matrix in the particle-hole space:

$$\check{g}(\boldsymbol{r}, \tilde{\boldsymbol{k}}, i\omega_n) = -i\pi \begin{pmatrix} \hat{g} & i\hat{f} \\ -i\hat{\bar{f}} & -\hat{\bar{g}} \end{pmatrix}, \tag{5.1}$$

where ω_n is the Matsubara frequency. The quasiclassical Green's function obeys the following Eilenberger equation with the spin quantization axis parallel to the z axis [49, 88, 89, 90, 91].

$$i\boldsymbol{v}_F(\tilde{\boldsymbol{k}}) \cdot \boldsymbol{\nabla} \check{g}(\boldsymbol{r}, \tilde{\boldsymbol{k}}, i\omega_n) + \left[i\omega_n \check{\tau}_3 - \check{\Delta}(\boldsymbol{r}) - \check{K}(\tilde{\boldsymbol{k}}), \check{g}(\boldsymbol{r}, \tilde{\boldsymbol{k}}, i\omega_n) \right] = \check{0}, \tag{5.2}$$

$$\check{K}(\tilde{\boldsymbol{k}}) \equiv \begin{pmatrix} t_\perp \hat{H}_{\mathrm{inter}} + \mu_B H \hat{H}_Z & \hat{0} \\ \hat{0} & t_\perp \hat{H}_{\mathrm{inter}} + \mu_B H \hat{H}_Z \end{pmatrix} + \alpha \begin{pmatrix} \hat{H}_{\mathrm{SO}}(\tilde{\boldsymbol{k}}) & \hat{0} \\ \hat{0} & \hat{H}_{\mathrm{SO}}^*(-\tilde{\boldsymbol{k}}) \end{pmatrix}, \tag{5.3}$$

with

$$\check{\tau}_3 = \begin{pmatrix} \sigma_0 \otimes I_{N \times N} & \hat{0} \\ \hat{0} & -\sigma_0 \otimes I_{N \times N} \end{pmatrix}, \quad \check{\Delta}(\boldsymbol{r}) = \begin{pmatrix} \hat{0} & \hat{\Delta}(\boldsymbol{r}) \\ -\hat{\Delta}^\dagger(\boldsymbol{r}) & \hat{0} \end{pmatrix}, \tag{5.4}$$

$$\hat{H}_Z = -\sigma_z \otimes I_{N \times N}, \quad \hat{H}_{\mathrm{inter}} = \sigma_0 \otimes T_\perp, \quad \hat{H}_{\mathrm{SO}}(\tilde{\boldsymbol{k}}) = \boldsymbol{g}(\tilde{\boldsymbol{k}}) \cdot \boldsymbol{\sigma} \otimes S_d. \tag{5.5}$$

Here, $I_{N \times N}$ is the unit matrix, $T_\perp = \mathrm{offdiag}(1, 1)$ and $S_d = \mathrm{diag}(1, -1)$. $\mathrm{offdiag}(\cdot, \cdot)$ indicates the 2×2 matrix which has the offdiagonal component only. $\hat{H}_{\mathrm{SO}}^*(-\tilde{\boldsymbol{k}}) = -\boldsymbol{g}(\tilde{\boldsymbol{k}}) \cdot \boldsymbol{\sigma}^{\mathrm{tr}} \otimes S_d$, which is obtained from the relation, $\boldsymbol{g}(-\tilde{\boldsymbol{k}}) = -\boldsymbol{g}(\tilde{\boldsymbol{k}})$. μ_B is the Bohr magneton. We use the unit in which $\hbar = k_B = 1$.

In the presence of the Zeeman term, the Eilenberger equation cannot be decomposed into the two equations defined on the each split Fermi surface due to the SOC even if we use the band basis. So we take the orbital basis, in which the spin quantization axis is parallel to the z-axis. In the orbital basis, one can transform Eq. (5.2) into the two matrix Riccati equations in the same manner described in Ref. [101] by regarding $\check{K}(\tilde{\boldsymbol{k}})$ as the *self energy*:

$$\boldsymbol{v}_F(\tilde{\boldsymbol{k}}) \cdot \boldsymbol{\nabla} \hat{a} + 2\omega_n \hat{a} + \hat{a}\hat{\Delta}^\dagger \hat{a} - \hat{\Delta} + i \left(\hat{K}_{11} \hat{a} - \hat{a}\hat{K}_{22} \right) = \hat{0}, \tag{5.6}$$

$$\boldsymbol{v}_F(\tilde{\boldsymbol{k}}) \cdot \boldsymbol{\nabla} \hat{b} - 2\omega_n \hat{b} - \hat{b}\hat{\Delta}\hat{b} + \hat{\Delta}^\dagger - i \left(\hat{b}\hat{K}_{11} - \hat{K}_{22}\hat{b} \right) = \hat{0}. \tag{5.7}$$

Here we have defined $\check{K} = \mathrm{diag}(\hat{K}_{11}, \hat{K}_{22})$ with $\hat{K}_{11} \equiv -\mu_B H \sigma_z \otimes I_{N \times N} + \alpha \boldsymbol{g}(\tilde{\boldsymbol{k}}) \cdot \boldsymbol{\sigma} \otimes S_d + t_\perp \sigma_0 \otimes T_\perp$

and $\hat{K}_{22} \equiv -\mu_{\mathrm{B}} H \sigma_z \otimes I_{N \times N} - \alpha \boldsymbol{g}(\tilde{\boldsymbol{k}}) \cdot \boldsymbol{\sigma}^* \otimes S_{\mathrm{d}} + t_\perp \sigma_0 \otimes T_\perp$. Introducing the following quantity

$$\hat{a} = \hat{a}_0(i\sigma_y \otimes I_{N \times N}), \ \hat{b} = (i\sigma_y \otimes I_{N \times N})\hat{b}_0, \tag{5.8}$$

$$\hat{K}_{11} = \hat{K}_{11}^0, \ \hat{K}_{22} = (-\sigma_y \otimes I_{N \times N})\hat{K}_{22}^0(\sigma_y \otimes I_{N \times N}), \tag{5.9}$$

$$\hat{\Delta} = \hat{\Delta}_0(i\sigma_y \otimes I_{N \times N}), \ \hat{\Delta}^\dagger = (i\sigma_y \otimes I_{N \times N})\hat{\Delta}_0^\dagger, \tag{5.10}$$

we obtain

$$\boldsymbol{v}_{\mathrm{F}}(\tilde{\boldsymbol{k}}) \cdot \boldsymbol{\nabla} \hat{a}_0 + 2\omega_n \hat{a}_0 + \hat{a}_0 \hat{\Delta}_0^\dagger \hat{a}_0 - \hat{\Delta}_0 + i\left(\hat{K}_{11}^0 \hat{a}_0 + \hat{a}_0 \hat{K}_{22}^0\right) = \hat{0}, \tag{5.11}$$

$$\boldsymbol{v}_{\mathrm{F}}(\tilde{\boldsymbol{k}}) \cdot \boldsymbol{\nabla} \hat{b}_0 - 2\omega_n \hat{b}_0 - \hat{b}_0 \hat{\Delta}_0 \hat{b}_0 + \hat{\Delta}_0^\dagger - i\left(\hat{b}_0 \hat{K}_{11}^0 + \hat{K}_{22}^0 \hat{b}_0\right) = \hat{0}. \tag{5.12}$$

Starting from the pairing interaction in Ref. [28], the gap equation for the spin-singlet pair potential $\Delta(\boldsymbol{r})$ is given by [1] (see Appendix F)

$$\Delta(\boldsymbol{r}) = \lambda \pi T \frac{1}{2} \sum_{-n_{\mathrm{c}}(T)-1 < n < n_{\mathrm{c}}(T)} \sum_{s_1' s_2'} (i\sigma_y)_{s_2' s_1'}^\dagger \left\langle f_{s_1' s_2'}^0(\boldsymbol{r}, \tilde{\boldsymbol{k}}', i\omega_n)(i\sigma_y)_{s_1' s_2'} \right\rangle_{\tilde{\boldsymbol{k}}'}. \tag{5.13}$$

$\langle \cdots \rangle_{\tilde{\boldsymbol{k}}}$ denotes the average on the circular arc with its radius 1. The coupling constant is determined from

$$\frac{1}{\lambda} = \ln\left(\frac{T}{T_{\mathrm{c}0}}\right) + \sum_{0 \le n < n_c(T)} \frac{2}{2n+1}, \tag{5.14}$$

where $T_{\mathrm{c}0}$ is the superconducting transition temperature for $\alpha = t_\perp = \mu_{\mathrm{B}} H = 0$ and $n_{\mathrm{c}}(T) = (\omega_{\mathrm{c}}/\pi T - 1)/2$. We fix the cut off frequency to $\omega_{\mathrm{c}} = 7\pi T_{\mathrm{c}0}$.

The local density of states per spin and layer is given by

$$N(E, \boldsymbol{r}) = -\frac{N_{\mathrm{F}}}{2N} \frac{1}{\pi} \left\langle \mathrm{Im}\left[\mathrm{Tr}\hat{g}(\boldsymbol{r}, \tilde{\boldsymbol{k}}, i\omega_n \to E + i\eta)\right] \right\rangle_{\tilde{\boldsymbol{k}}}, \tag{5.15}$$

where N_{F} is the density of states per spin and layer at the Fermi level in the normal state.

5.3 Results and discussions

In this section, we display the self-consistently calculated numerical results of the pair potential profiles and the local density of states (LDOS). We fix the temperature and the interlayer hopping to $T/T_{\mathrm{c}0} = 0.1$ and $t_\perp/T_{\mathrm{c}0} = 1$, respectively.

5.3.1 Pair potential

In Fig. 5.1, we show the spatial variations of the pair potential amplitude around a vortex in (a) the BCS and (b) the PDW states for $\alpha/T_{\mathrm{c}0} = 2$. The horizontal axis is normalized by the coherence length $\xi_0 = v_{\mathrm{F}}/T_{\mathrm{c}0}$. Each plot corresponds to the different magnetic field. The amplitude of the pair potential gets smaller with increasing the Zeeman field due to the paramagnetic pair breaking effect in both pairing states. One can notice that the pair potential amplitude of the PDW state is smaller than that of the BCS state. It is because the PDW state stabilizes in a high magnetic field under the influence of the paramagnetic depairing. Though the amplitude of the pair potential in the PDW state is smaller than that in the BCS state, the core size in the PDW state does not spread (compare the profiles for $\mu_{\mathrm{B}} H/T_{\mathrm{c}0} = 1.5$). The core size in the PDW state for $\mu_{\mathrm{B}} H/T_{\mathrm{c}0} = 1.5$ and 2 is smaller than that in the BCS state for $\mu_{\mathrm{B}} H/T_{\mathrm{c}0} = 1.5$. Thus, the sudden decrease in the core radius with increasing the magnetic field is a signature of the BCS-PDW phase transition. The BCS state is completely destroyed for $\mu_{\mathrm{B}} H/T_{\mathrm{c}0} \gtrsim 2$, whereas in the PDW state, the nonzero self-consistent solutions of the pair potential exist even for the high magnetic field $\mu_{\mathrm{B}} H/T_{\mathrm{c}0} \gtrsim 2$. The profiles of the pair potential is not altered for $\alpha/T_{\mathrm{c}0} = 50$ for $\mu_{\mathrm{B}} H = 0$.
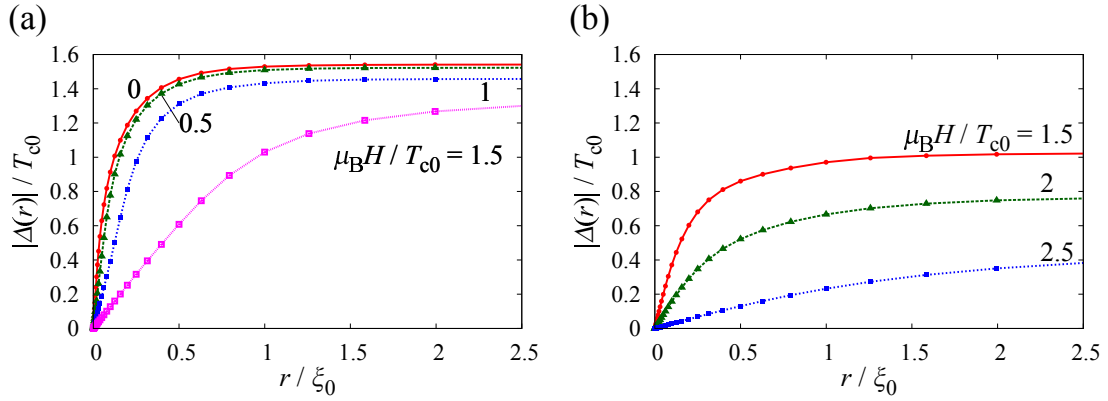
Figure 5.1: Spatial profiles of the pair potential amplitude $|\Delta(r)|$ for (a) the BCS state and (b) the PDW one. The horizontal axis represents the radial distance from a vortex center $r = 0$. We set $T/T_{c0} = 0.1$, $\alpha/T_{c0} = 2$ and $t_\perp/T_{c0} = 1$. The data is plotted for each Zeeman field $\mu_B H/T_{c0}$. Reprinted figure with permission from [Yoichi Higashi, Yuki Nagai, Tomohiro Yoshida, and Youichi Yanase, Journal of Physics: Conference Series **568**, 022018 (2014)] Copyright (2014) by IOP Publishing.

Figure 5.2 shows the spatial profiles of the pair potential amplitude $|\Delta(r)|$ around a vortex for (a) the BCS state and (b) the PDW one, respectively. The BCS state [Fig. 5.2(a)] is destroyed due to the paramagnetic depairing for $\alpha/T_{c0} \lesssim 1$. On the other hand, the PDW state survives even if the SOC is small $\alpha/T_{c0} \lesssim 1$ [Fig. 5.2(b)]. In the PDW state, the pair potential amplitude gets larger monotonically with increasing the SOC strength α. In Fig. 5.2 (b), each curve shows the pair potential profile for $\alpha/T_{c0} = 0.2$-2 from bottom to top by 0.2 step. This is because the Rashba type SOC locks the spin quantization axis within the x-y plane and then the paramagnetic depairing effect is suppressed. In contrast, in the BCS state, the pair potential amplitude behaves non-monotonically with respect to the SOC strength. Another feature is seen in the vortex core radius. As shown is Fig. 5.2 (b), the core radius in the PDW state is smaller than that in the BCS state. This feature gets prominent with increasing the SOC strength.

In the uniform system without vortices, the stable pairing state prefers the larger bulk amplitude of the pair potential. In this study, though there is a vortex in the system, we consider that the pair potential with the larger bulk amplitude is the more stable solution of the gap equation for a given magnetic field. The T-H phase diagram of bilayer system is displayed in Ref. [42], which is not altered qualitatively in the vortex state when the system belongs to type-II limit and has the large Maki parameter [42, 102]. According to the field dependence of the pair potential amplitude in the bulk obtained by the quasiclassical theory, the non-zero self-consistent solution of the gap equation exists only in the PDW state for $\mu_B H/T_{c0} \gtrsim 1.8$. This is consistent with the results calculated from the Bogoliubov-de Gennes equation [42].

5.3.2 Local density of states

In Fig. 5.3, we display the energy and spatial dependence of the local density of states (LDOS) around a vortex core. On the basis of the consideration in the subsection 5.3.1, the calculation of the LDOS is conducted for (a) $\mu_B H/T_{c0} = 1.5$ in the BCS state and (b) $\mu_B H/T_{c0} = 2$ in the PDW one. As shown in Fig. 5.3(a), the zero energy peak (ZEP) splits off due to the Zeeman field. The Zeeman split of the ZEP gets suppressed with increasing the SOC strength α for a fixed magnetic field, since the spin quantization axis is locked within the x-y plane by the Rashba SOC.

Contrastingly, though the PDW state emerges in a high magnetic field, the zero energy peak exists, which is quite different from the LDOS structure in the BCS state. If the zero energy quasiparticle states within a core are experimentally observed by scanning tunneling
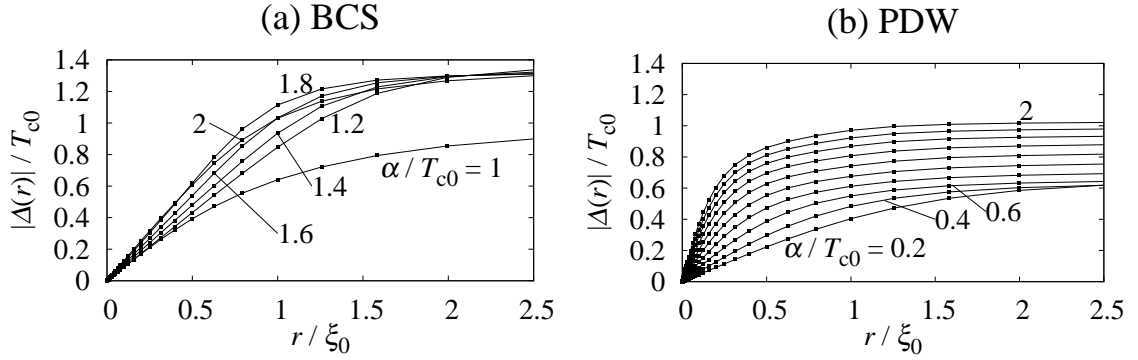
Figure 5.2: Spatial profiles of the pair potential amplitude $|\Delta(r)|$ for (a) the BCS state and (b) the PDW one. The horizontal axis represents the radial distance from a vortex center $r = 0$. We set $T/T_{c0} = 0.1$, $\mu_B H/T_{c0} = 1.5$ and $t_\perp/T_{c0} = 1$. Each curve indicates different spin-orbit coupling strength.

microscopy/spectroscopy (STM/STS), the STM/STS image of a vortex in the PDW state can be drastically different from that in the BCS state. To obtain the clue to the LDOS structure in the PDW state, we start from the case with $\alpha/T_{c0} = 0$ for simplicity. In this case, the four folding ZEP splits into the four peaks. First, for $\mu_B H/T_{c0} = 0$, the band degeneracy is lifted by the interlayer hopping and the ZEP splits into the two peaks. This split of the ZEP is regarded as the level repulsion of the zero energy bound states. In the BCS state, the band degeneracy is not lifted only by the interlayer hopping. Then, the π phase difference between the layers is essential for the repulsion of the zero energy bound states. Second, each peak is split off due to the Zeeman field. Hence the four peaks appear due to the interlayer hopping and the Zeeman field. Further increasing the magnetic field, the two peaks in the low energy side shift to the lower energy side and those in the high energy side shift to the higher energy one. Eventually the two peaks in the low energy side get combined and a single zero energy peak appears. This scenario gives the interpretation for the appearance of the zero energy peak in the PDW state, but that is not sufficient when changing the SOC strength.

Let us consider the LDOS structure including the vortex bound states in the high energy side. Figure 5.4 shows the energy and the spatial dependence of the LDOS around the vortex core for $\alpha/T_{c0} = 2$ and $\mu_B H/T_{c0} = 1.5$. The LDOS is plotted up to the high energy $E = 4T_{c0}$. The calculation is conducted for the BCS state [Fig. 5.4(a)] and the PDW state [Fig. 5.4(b)] with use of the self-consistent solutions for the gap equation displeyed in Fig. 5.2. In the BCS states, as shown in Fig. 5.4(a), the zero energy vortex bound states split into the four peaks due to the interlayer hopping and the Zeeman field. On the other hand, in the PDW state, the large quasiparticle states appear at the zero energy [see Fig. 5.4(b)]. This is quite contrasting with the LDOS structure in the BCS state, whereas the vortex bound states peaks in the high energy side exist as well as in the BCS state.

In the PDW state without the SOC (The PDW state is indeed unstable in the absence of the SOC.), the four LDOS peaks appear as well as that in the BCS state due to the interlayer hopping and the Zeeman field. The two peaks at the low energy side shift to the lower energy side with increasing the Zeeman field. Further increasing the Zeeman field, the two peaks get combined and cross the zero energy each other. In the absence of the SOC, it appears that the quasiparticle structure in the PDW state is similar to the low field quasiparticle structure in the BCS state. One might consider that the crossed two peaks get combined with increasing the SOC strength. However, we should note that there is another origin of the appearance of the zero energy vortex bound states in the PDW state, which is described in the following subsections.
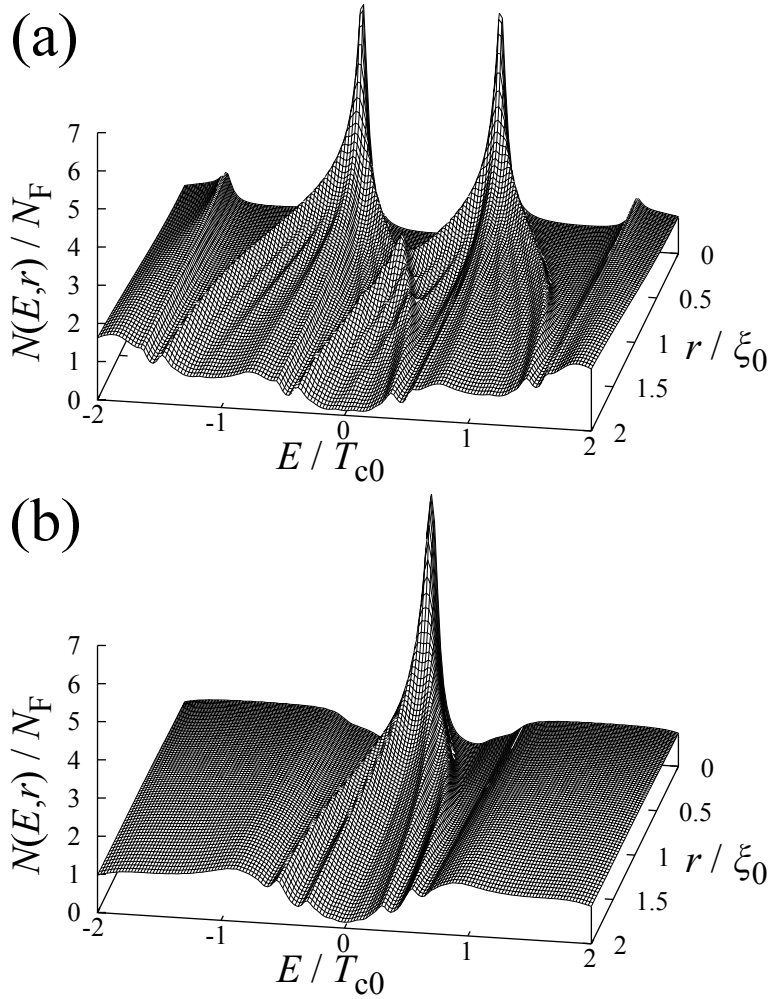
Figure 5.3: The local density of states $N(E, r)$ for (a) the BCS state and (b) the PDW one. The Zeeman field is set to (a) $\mu_B H/T_{c0} = 1.5$ and (b) $\mu_B H/T_{c0} = 2$. Other conditions are $T/T_{c0} = 0.1$, $\alpha/T_{c0} = 2$, $t_\perp/T_{c0} = 1$ and $\eta = 0.05 T_{c0}$. Reprinted figure with permission from [Yoichi Higashi, Yuki Nagai, Tomohiro Yoshida, and Youichi Yanase, Journal of Physics: Conference Series **568**, 022018 (2014)] Copyright (2014) by IOP Publishing.

5.3.3 Dependence of zero energy peak on spin-orbit coupling

In this subsection, we investigate the SOC strength dependence of the vortex bound states. As discussed in the previous subsection, in the absence of the SOC, the quasiparticle structure around the vortex is similar between the PDW and BCS states. However, in the presence of the SOC, the internal structure of the Cooper pair changes. Thereby the quasiparticle structure also changes. As shown in Fig. 5.3 and Fig. 5.4, the zero energy quasiparticle structure around a vortex core in the PDW state is quite contrasting with that in the BCS state in the presence of the SOC. To see clearly the difference of the quasiparticle structure, we show in Fig. 5.5 the SOC strength and the energy dependences of the LDOS at the vortex center for $\mu_B H/T_{c0} = 1.5$. In the BCS state, superconductivity is destroyed due to the paramagnetic depairing for $\alpha/T_{c0} \lesssim 1$. As shown in Fig. 5.5(a), the zero energy LDOS splits almost independent of the SOC strength. The peaks in the low energy shift a bit to lower energy with increasing the SOC strength, whereas those in the high energy move to higher energy.

On the other hand, in the PDW state, the zero energy LDOS gradually appears with increasing the SOC strength [see Fig. 5.5(b)]. At $\alpha = 2T_{c0}$, the LDOS structure at the vortex center
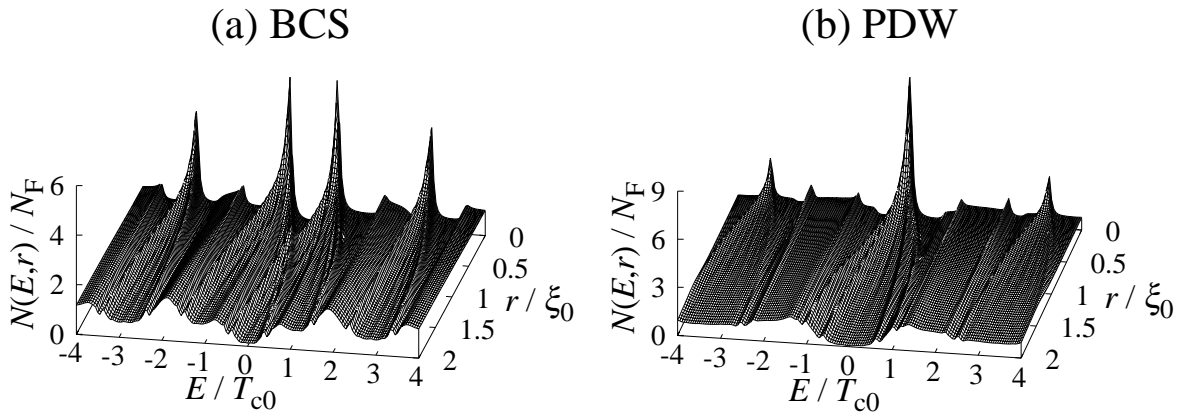
(a) BCS

(b) PDW

Figure 5.4: The local density of states $N(E, r)$ for (a) the BCS state and (b) the PDW one. The Zeeman field is set to $\mu_B H/T_{c0} = 1.5$ and the spin-orbit coupling is $\alpha/T_{c0} = 2$ for both pairing states. Other parameters are $T/T_{c0} = 0.1$, $t_\perp/T_{c0} = 1$ and $\eta = 0.05 T_{c0}$.

(a) BCS, $N(r = 0, E, \alpha)/N_F$

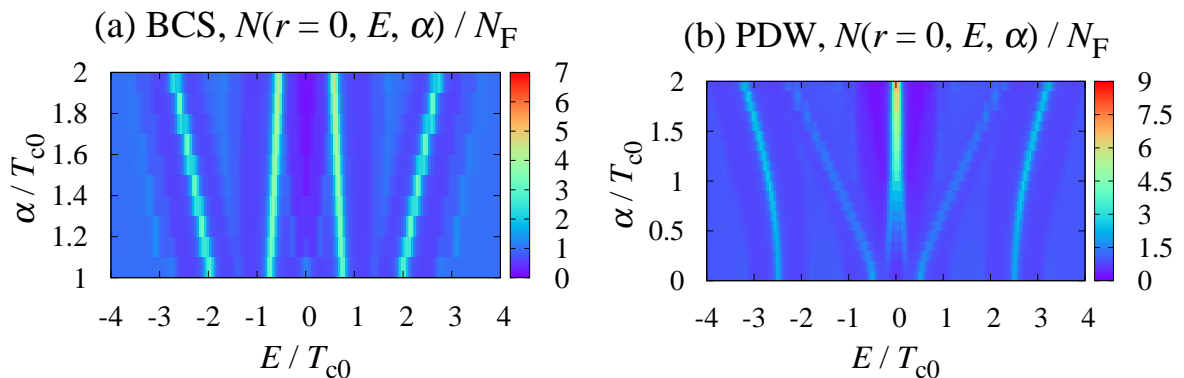## (b) PDW, $N(r = 0, E, \alpha)/N_F$

Figure 5.5: (Color online) The energy and the spin-orbit coupling strength dependences on the local density of states at the vortex center $N(r = 0, E, \alpha)$ for the BCS state (a) and the PDW state (b) for $\mu_B H/T_{c0} = 1.5$. Other parameters are $T/T_{c0} = 0.1$, $t_\perp/T_{c0} = 1$ and $\eta = 0.05 T_{c0}$.

coincide with that in Fig. 5.4(b). Thus, the SOC plays the crucial role in understanding the contrasting low energy LDOS structure between the BCS and the PDW state.

In the real materials, for example, the CeCoIn$_5$/YbCoIn$_5$ superlattice, the superconducting layer is CeCoIn$_5$, which is experimentally identified as a d-wave superconductor [52, 53, 103]. The LDOS structure obtained in this study changes considerably, since the quasiparticle states around a vortex are sensitive to the pairing symmetry. The more realistic calculation assuming the d-wave pairing symmetry is the future work.

In the next section, we show the energy spectra in the bulk to investigate the effect of the SOC on the energy dispersion structure.

5.3.4 Energy spectra

In this section, we show the energy spectra in the bulk to investigate the effect of the SOC on the energy dispersion structure, and discuss the relation between the bulk gap and the vortex
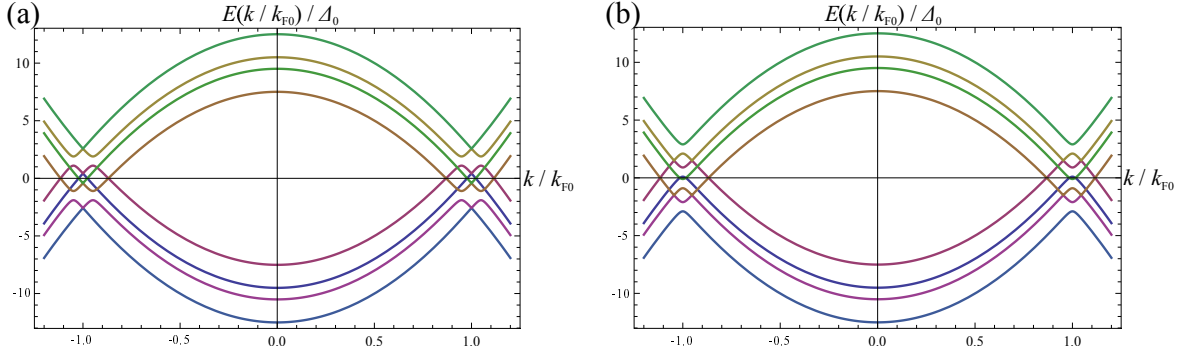
Figure 5.6: Energy spectra in the BCS state (a) and the PDW state (b) for $\alpha = 0$. The horizontal axis denotes the wave number normalized by the Fermi wave number k_{F0} for $\alpha = t_\perp = \mu_B H = 0$. The superconducting gap energy is set to $|\Delta|/\Delta_0 = 0.4$. Other parameters are set to $\mu_B H/\Delta_0 = 1.5$, $t_\perp/\Delta_0 = 1$, $E_F/\Delta_0 = 10$.
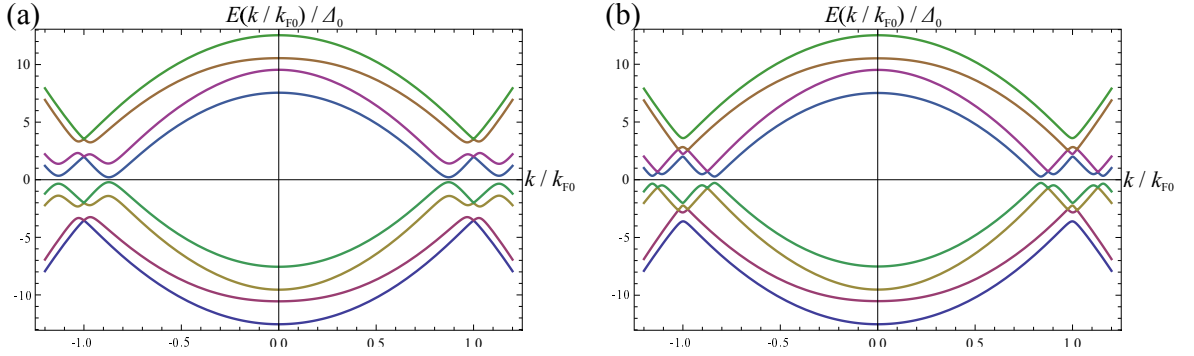

Figure 5.7: Energy spectra in the BCS state (a) and the PDW state (b) for $\alpha/\Delta_0 = 2$. The horizontal axis denotes the wave number normalized by the Fermi wave number k_{F0} for $\alpha = t_\perp = \mu_B H = 0$. The superconducting gap energy is set to $|\Delta|/\Delta_0 = 1$ (a) and $|\Delta|/\Delta_0 = 0.5$ (b). Other parameters are set to $\mu_B H/\Delta_0 = 1.5$, $t_\perp/\Delta_0 = 1$, $E_F/\Delta_0 = 10$.

bound states. We diagonalize the following 8×8 BdG Hamiltonian to obtain the energy spectra.

$$\check{\mathscr{H}}_{\mathrm{BdG}} = \begin{pmatrix} \hat{\mathscr{H}}_0(\boldsymbol{k}) & \hat{\Delta} \\ \hat{\Delta}^\dagger & -\hat{\mathscr{H}}_0^*(-\boldsymbol{k}) \end{pmatrix}, \tag{5.16}$$

$$\hat{\mathscr{H}}_0(\boldsymbol{k}) = \begin{pmatrix} \xi(\boldsymbol{k})\sigma_0 + \alpha\boldsymbol{g}(\boldsymbol{k})\cdot\boldsymbol{\sigma} - \mu_B\boldsymbol{H}\cdot\boldsymbol{\sigma} & t_\perp\sigma_0 \\ t_\perp\sigma_0 & \xi(\boldsymbol{k})\sigma_0 - \alpha\boldsymbol{g}(\boldsymbol{k})\cdot\boldsymbol{\sigma} - \mu_B\boldsymbol{H}\cdot\boldsymbol{\sigma} \end{pmatrix}, \tag{5.17}$$

$$-\hat{\mathscr{H}}_0^*(-\boldsymbol{k}) = \begin{pmatrix} -\xi(\boldsymbol{k})\sigma_0 + \alpha\boldsymbol{g}(\boldsymbol{k})\cdot\boldsymbol{\sigma}^* + \mu_B\boldsymbol{H}\cdot\boldsymbol{\sigma} & -t_\perp\sigma_0 \\ -t_\perp\sigma_0 & -\xi(\boldsymbol{k})\sigma_0 - \alpha\boldsymbol{g}(\boldsymbol{k})\cdot\boldsymbol{\sigma}^* + \mu_B\boldsymbol{H}\cdot\boldsymbol{\sigma} \end{pmatrix}, \tag{5.18}$$

$$\hat{\Delta} = \begin{pmatrix} \Delta i\sigma_y & 0_{2\times2} \\ 0_{2\times2} & s\Delta i\sigma_y \end{pmatrix}. \tag{5.19}$$

Here we have used $\xi(-\boldsymbol{k}) = \xi(\boldsymbol{k})$ and $\boldsymbol{g}(-\boldsymbol{k}) = -\boldsymbol{g}(\boldsymbol{k})$ with the orbital vector $\boldsymbol{g}(\boldsymbol{k}) = (-k_y, k_x, 0)/k_{F0} = (k/k_{F0})(-\sin\phi_k, \cos\phi_k, 0)$ in two dimensional layers. k_{F0} is the Fermi wave number in the absence of the SOC, the Zeeman field and the interlayer hopping. We do not consider the parity mixing of the order parameter. $s = 1$ (-1) corresponds to the BCS (PDW) state.

In general, the SOC strength α is much larger than the superconducting gap energy Δ_0 and much smaller than the Fermi energy E_F. Thus, in the quasiclassical regime, namely, $k_F\xi_0 \sim E_F/\Delta_0 \gg 1$, the energy scale of the SOC can satisfy the condition $\Delta_0 \ll \alpha \ll E_F$. In this
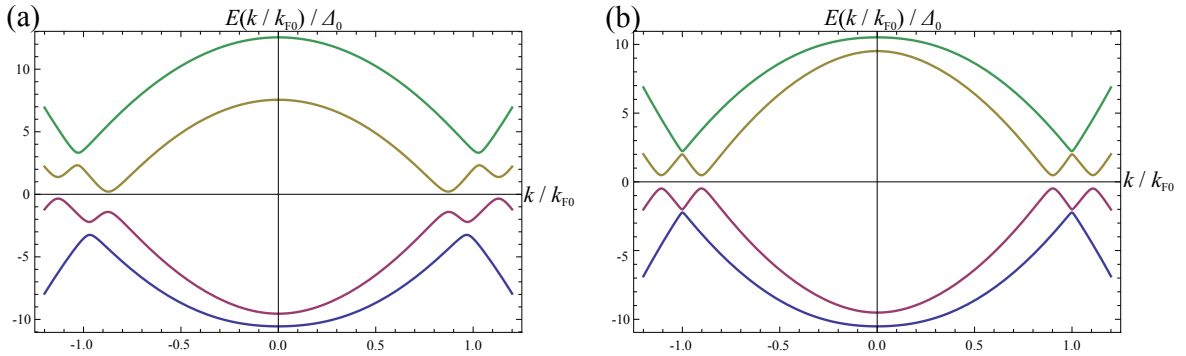
Figure 5.8: Energy spectra of the mirror sector in the BCS state (a) and the PDW state (b) for $\alpha/\Delta_0 = 2$. The horizontal axis denotes the wave number normalized by the Fermi wave number k_{F0} for $\alpha = t_\perp = \mu_\mathrm{B} H = 0$. The superconducting gap energy is set to $|\Delta|/\Delta_0 = 1$ (a) and $|\Delta|/\Delta_0 = 0.5$ (b). Other parameters are set to $\mu_\mathrm{B} H/\Delta_0 = 1.5$, $t_\perp/\Delta_0 = 1$, $E_\mathrm{F}/\Delta_0 = 10$.

situation, the split of the Fermi surface due to the SOC, the Zeeman field and the inter-layer hopping is sufficiently small, and then we can approximate the energy dispersion by that of free electrons. Thus, we used the free electron dispersion $\xi(k)/\Delta_0 = (k_{\mathrm{F0}}\xi_0)[(k/k_{\mathrm{F0}})^2 - 1]/2$ with the coherence length $\xi_0 = v_{\mathrm{F0}}/\Delta_0$.

On the other hand, in the quantum limit (low particle density limit), namely $k_{\mathrm{F0}}\xi_0 \sim E_\mathrm{F}/\Delta_0 \sim 1$, the SOC energy is of the order of the Fermi energy ($\alpha \sim E_\mathrm{F} \sim \Delta_0$). So we cannot neglect the split of the Fermi surface due to the SOC, the Zeeman field and the inter layer hopping. We displayed above the quasiparticle local density of states calculated by the quasiclassical theory, but here we show the bulk energy spectra deviated away from the quasiclassical regime [$E_\mathrm{F}/\Delta_0 = 10$ ($k_{\mathrm{F0}}\xi_0 = 20$)] for viewability of figures. We confirmed that the structure of the bulk energy spectra in the quantum regime is not altered qualitatively compared with that in the quasiclassical regime.

We show below the energy spectra for the BCS and the PDW state in the bulk obtained by diagonalizing the 8×8 BdG Hamiltonian matrix in the absence and the presence of the SOC. To see clearly the energy spectra in the presence of the SOC, we also display the energy spectra of the mirror sector of the block-diagonalized BdG Hamiltonian with use of the mirror symmetry [104].

As investigated in Ref. [87] and pointed out in Ref. [42], in the absence of the SOC, intraband quasiparticle states form the Cooper pairs in the BCS state, but interband pairing states is realized in the PDW state. The superconducting energy gap can be viewed as the hybridization gap between electron and hole bands in a certain basis, and in this study, we assume the spin singlet pairing state. Thus, the superconducting gap opens at the point where electron and hole branches intersect with opposite spin in the real spin basis within the band for $\alpha = 0$. The inter layer hopping $t_\perp$ acts as an effective Zeeman magnetic field $(\mu_\mathrm{B} H \pm t_\perp)\sigma_z$, which can be understood by block-diagonalyzing the BdG Hamiltonian using the mirror symmmetry in the bilayer system [105]. Then, electron and hole bands split due to an effective Zeeman field $(\mu_\mathrm{B} H \pm t_\perp)\sigma_z$ lifting the four fold degeneracy. As a result, four energy bands appear in the electron and hole branches, respectively. In Figs. 5.6(a) and 5.6(b), the branches convex downward are the electron bands, $E_{2\uparrow}(k)$, $E_{1\uparrow}(k)$, $E_{2\downarrow}(k)$ and $E_{1\downarrow}(k)$ from bottom to top at $k = 0$ and those convex upward are the hole bands, $-E_{2\uparrow}(k)$, $-E_{1\uparrow}(k)$, $-E_{2\downarrow}(k)$ and $-E_{1\downarrow}(k)$ from top to bottom at $k = 0$.

Thus, in the BCS state for $\alpha = 0$, there are four intra band spin-singlet pairing states, namely four intersections: $[E_{1\uparrow}(k), -E_{1\downarrow}(k)]$, $[E_{1\downarrow}(k), -E_{1\uparrow}(k)]$, $[E_{2\uparrow}(k), -E_{2\downarrow}(k)]$ and $[E_{2\downarrow}(k), -E_{2\uparrow}(k)]$, where $[E_{ms}(k), -E_{ms'}(k)]$ indicates the crossing point of electron band $E_{ms}(k)$ and hole band $-E_{ms'}(k)$. m and s indicate the indices of layer and spin, respectively. On the other hand, in the PDW state for $\alpha = 0$, there are four inter band spin-singlet pairing state: $[E_{1\uparrow}(k), -E_{2\downarrow}(k)]$, $[E_{1\downarrow}(k), -E_{2\uparrow}(k)]$, $[E_{2\uparrow}(k), -E_{1\downarrow}(k)]$ and $[E_{2\downarrow}(k), -E_{1\uparrow}(k)]$.

43

Figs. 5.6(a) and 5.6(b) show the energy spectra in the absence of the SOC for the BCS state and the PDW state, respectively. We choose the parameter $\mu_{\mathrm{B}}H/T_{\mathrm{c}0} = 1.5$ and $t_{\perp}/T_{\mathrm{c}0} = 1$. The superconducting gap size is set to $|\Delta|/\Delta_0 = 0.4$ for viewability. The superconducting gaps open symmetrically with respect to the Fermi energy, which comes from the particle-hole symmetry and do not open at the Fermi energy. The difference of the energy spectral structure between the BCS and the PDW state comes from the internal structure of the Cooper pairing discussed above. Indeed, however, the BCS state for $\alpha = 0$ is completely destroyed due to the paramagnetic depairing for $\mu_{\mathrm{B}}H/T_{\mathrm{c}0} = 1.5$, and the PDW state for $\alpha = 0$ is unstable, since inter band pairing brings a loss of energy.

On the other hand, in the presence of the SOC, intraband quasiparticle states form the Cooper pairs both in the BCS and PDW state. We notice that the superconducting gaps open at the four intersection of the energy bands in the vicinity of the Fermi energy in Figs. 5.7(a) and 5.7(b), respectively. The energy spectral structure changes from that for $\alpha = 0$, which comes from the change of the Cooper pairing structure due to the SOC.

First, in the BCS state [Fig. 5.7(a)], the center of the superconducting gap energy is dislocated from E_{F} [$E(k) = 0$]. To see clearly this point, in Fig. 5.8(a), we show the energy spectra for the mirror sector of the block-diagonalized BdG Hamiltonian in the BCS state. There is an asymmetry between electron bands and hole bands, leading to the shift of the superconducting gaps center from E_{F}. This is because there is no particle-hole symmetry in the mirror sector for even parity superconductivity [104]. The BCS state is indeed an even parity superconducting state [42]. The other mirror sector also gives the energy spectra without particle-hole symmetry. When the superconducting gap opens in the bulk, large quasiparticle bound states (Andreev bound states) are formed at the center of a singly quantized vortex at the Fermi level. Thus, in the BCS state, the peaks of Andreev bound states at the vortex core moves from E_{F} to the finite energy, which corresponds to the split of the zero energy peak into the two peaks at low energy side in Figs. 5.3(a) and 5.4(a). The superconducting gaps at the high energy side in Fig. 5.7(a) corresponds to the peaks at high energy in Fig. 5.4(a). As shown in Fig. 5.8(a), inside the superconducting gap, another energy band is located, and so there is non-zero local density of states inside the gap in the bulk in Fig. 5.4(a), reflecting finite density of states on another Fermi surface. The small superconducting gap at E_{F} in Fig. 5.7(a) is produced by the overlap of the superconducting gap dislocated from E_{F}, which appears as the BCS like gap in the quasiparticle spectrum at the zero energy in Figs. 5.3(a) and 5.4(a).

Next, in the PDW state [Fig. 5.7(b)], the superconducting gaps open at E_{F}. The PDW state is an odd parity superconducting state. For odd parity superconductivity, there is particle-hole symmetry in the mirror sector [104]. As shown in Fig. 5.8(b), particle-hole symmetry is observed in the energy spectra for the mirror sector of the block-diagonalized BdG Hamiltonian in the PDW state. If the superconducting gap opens at E_{F}, the center of the gap necessarily locates at E_{F} due to particle-hole symmetry. Regarding the Zeeman field as a perturbation [106, 107] and using the band basis, the order parameter in the band basis is obtained in the same form as Ref. [87] (In the present study, we neglect the spin-triplet component). In Fig. 5.7(b), the superconducting gaps at E_{F} comes from the intra band equal pseudo-spin Cooper pairing [87]. This superconducting states certainly appears in the presence of the SOC [87]. The superconducting gaps at high energy in Fig. 5.7(b) are due to the inter band pairing, which is neglected in Ref. [87]. As a result of above discussion, the zero energy peak of the vortex bound states appears in the PDW state in Figs. 5.3(b) and 5.4(b).

5.4   Summary

We have numerically investigated the electronic structure of a vortex core in bilayer Rashba superconductors by means of the self-consistent quasiclassical calculation. We found that the local density of states (LDOS) structure in the pair-density wave (PDW) state is quite different from that in the BCS state. The zero energy vortex bound state exists in the PDW state, whereas it is absent in the BCS state due to the Zeeman effect. This prominent difference stems from (i) whether or not there is particle-hole symmetry in the mirror sector of the block-diagonalized BdG Hamiltonian and (ii) the change of the internal structure of the Cooper pair due to the SOC.

Another feature of the PDW state is that the core size is small compared with that in the BCS state in the vicinity of the BCS-PDW phase transition. The characteristic vortex core structure in the PDW state can be observed by scanning tunneling spectroscopy at low temperature. These features in a magnetic field can be a key to identify the exotic superconducting phase.

Chapter 6

Excitation spectra and wave functions of quasiparticle bound states in bilayer Rashba superconductors

We study the excitation spectra and the wave functions of quasiparticle bound states at a vortex and an edge in bilayer Rashba superconductors under a magnetic field. In particular, we focus on the quasiparticle states at the zero energy in the pair-density wave state in a topologically non-trivial phase. We numerically demonstrate that the quasiparticle wave functions with zero energy are localized at both the edge and the vortex core if the magnetic field exceeds the critical value.

6.1   Introduction

Superconductivity in locally noncentrosymmetric systems has recently attracted considerable interest [39, 40]. In such systems, a variety of anti-symmetric spin-orbit coupling arises depending on the local inversion symmetry breaking. A lot of materials have the local noncentrosymmetricity in their crystal structures, one of which is the artificially fabricated heavy Fermion superlattice $CeCoIn_5/YbCoIn_5$ [99]. Some experiments have been conducted under a magnetic field, focusing on the role of the noncentrosymmetric superconductivity in the superlattice $CeCoIn_5/YbCoIn_5$ [108, 100]. From the experiment on the angular dependence of the H_{c2}, Goh *et al.* obtained the evidence that the FFLO like inhomogeneous superconductivity realizes under the parallel field in the $CeCoIn_5/YbCoIn_5$ superlattice [108]. The superconductivity in multilayered systems as a simple model of the superlattice of $CeCoIn_5$ is investigated also theoretically [87] and the spatially inhomogeneous exotic superconducting phase is proposed under a high magnetic field [42].

In our previous study, we analyzed the electronic structure of a single vortex in the pair-density wave (PDW) state, in which the order parameter phase changes its sign in bilayer systems. Then we found the salient feature of the PDW state, that is, the zero energy quasiparticle states at the vortex core exist even in a high magnetic field, using the quasiclassical theory [101]. However, we could not obtain the more microscopic information on the vortex core structure such as the excitation spectra and the wave functions, in principle, in the framework of the quasiclassical theory.

In this study, we do not touch the BCS phase, in which the order parameter phase does not change its sign, and focus on the PDW state. We obtain the microscopic information on the quasiparticle states in the PDW state with use of the Bogoliubov-de Gennes theory. We present the excitation spectra and the Bogoliubov quasiparticle wave functions of bound states at the

vortex core and the edge.

6.2 Formulation

First of all, we characterize multilayer Rashba systems under a magnetic field. We incorporate the effect of the magnetic field into the theory through the Zeeman term reflecting the dominant paramagnetic effect and the spatial inhomogeneity of the order parameter due to a vortex line. Reflecting the lacking of mirror symmetry about each layer, the antisymmetric spin-orbit coupling (ASOC) strength has the layer dependence α_m with the layer index m. The layer dependence of the ASOC is $(\alpha_1, \alpha_2) = (\alpha, -\alpha)$ in the bilayer system. The net ASOC is zero due to the mirror symmetry of the entire system.

We start with the following Bogoliubov-de Gennes equation for bilayer Rashba superconductors.

$$\left(\begin{array}{cc} \hat{H}\left(-i\boldsymbol{\nabla}\right) & \hat{\Delta}(\boldsymbol{r}) \\ \hat{\Delta}^{\dagger}(\boldsymbol{r}) & -\hat{H}^{*}\left(i\boldsymbol{\nabla}\right)) \end{array} \right) \left(\begin{array}{c} \boldsymbol{u}_{jn}(\boldsymbol{r}) \\ \boldsymbol{v}_{jn}(\boldsymbol{r}) \end{array} \right) = E_{jn} \left(\begin{array}{c} \boldsymbol{u}_{jn}(\boldsymbol{r}) \\ \boldsymbol{v}_{jn}(\boldsymbol{r}) \end{array} \right),$$

with the normal state Hamiltonian in the real space representation

$$\hat{H}\left(-i\boldsymbol{\nabla}\right) = \left(\begin{array}{cc} h_1(-i\boldsymbol{\nabla}) & t_{\perp}\sigma_0 \\ t_{\perp}\sigma_0 & h_2(-i\boldsymbol{\nabla}) \end{array} \right), \tag{6.1}$$

$$h_1(-i\boldsymbol{\nabla}) = \xi\left(-i\boldsymbol{\nabla}\right)\sigma_0 - \mu_{\mathrm{B}}\boldsymbol{H}\cdot\boldsymbol{\sigma} + \alpha_1\boldsymbol{g}\left(-i\boldsymbol{\nabla}\right)\cdot\boldsymbol{\sigma}, \tag{6.2}$$

$$h_2(-i\boldsymbol{\nabla}) = \xi\left(-i\boldsymbol{\nabla}\right)\sigma_0 - \mu_{\mathrm{B}}\boldsymbol{H}\cdot\boldsymbol{\sigma} + \alpha_2\boldsymbol{g}\left(-i\boldsymbol{\nabla}\right)\cdot\boldsymbol{\sigma}, \tag{6.3}$$

where $\boldsymbol{u}_{jn}(\boldsymbol{r})$ and $\boldsymbol{v}_{jn}(\boldsymbol{r})$ are the wave functions of Bogoliubov quasiparticles with n and j the angular momentum (azimuthal) and the radial quantum number, respectively, and $\xi(-i\boldsymbol{\nabla}) = (-i\boldsymbol{\nabla})^2/(2m) - \mu$ with the mass of electron m and the chemical potential μ. h_1 and h_2 are the normal state Hamiltonian for the layer 1 and 2, respectively. μ_{B} is the Bohr magneton, $\boldsymbol{H}$ is the magnetic field vector, $\boldsymbol{\sigma} = (\sigma_x, \sigma_y, \sigma_z)^{\mathrm{T}}$ is the vector of the Pauli spin matrices, σ_0 is the unit matrix in the spin space and $t_{\perp}$ is the interlayer hopping strength. We take the Rasba type ASOC characterized by the orbital vector $\boldsymbol{g}(-i\boldsymbol{\nabla}) = (i\partial_y, -i\partial_x, 0)/k_{\mathrm{F}}$ with the Fermi wave number k_{F}. We use the unit in which $\hbar = 1$.

We consider a single vortex in a spin-singlet s-wave disk-shaped superconductor with its radius r_{c}. The magnetic field is applied perpendicular to the layer $\boldsymbol{H} = (0, 0, H)$ and the vortex line is parallel to the z axis. The pair potential in the bilayer system is expressed as $\hat{\Delta}(\boldsymbol{r}) = \Delta_0 f(r)e^{i\phi_{\mathrm{r}}}\mathrm{diag}(i\sigma_y, si\sigma_y)$ where $s = 1$ ($s = -1$) denotes the BCS (PDW) state. The vortex center is situated at the origin $\boldsymbol{r} = \boldsymbol{0}$. We assume the spatial profile of the pair potential as the same in each layer and put $f(r) = \tanh(r/a)$ around a vortex. Here, a is the lattice constant, which is introduced as follows. Expanding the tight-binding model for the two dimensional square lattice, $\varepsilon(\boldsymbol{k}) = -2t[\cos(k_x a) + \cos(k_y a)]$ with respect to k_x and k_y up to the power of two and comparing with the free electron dispersion $\varepsilon(k) = k^2/2m$, we have the relation, $t = 1/(2ma^2)$. We have introduced the lattice constant a as a unit of length and the nearest neighbor hopping integral t as a unit of energy. The characteristic length scale of superconductivity is the coherence length, but in the present study, a Fermi surface is split due to the SOC, the Zeeman field and the inter layer hopping, and then the coherence length depends on them. To avoid this difficulty, we use a and t as the unit of length and energy, respectively. They are independent of the SOC, the Zeeman field and the inter layer hopping.

The system has the rotational symmetry about a vortex line. So we can introduce the cylindrical coordinates. In this situation, we can separate the quasiparticle wave functions into the angular and the radial parts: $\boldsymbol{u}_{jn_i}^i(\boldsymbol{r}) = \exp(in_i\phi_{\mathrm{r}})\boldsymbol{u}_j^i(r)$, $\boldsymbol{v}_{jl_i}^i(\boldsymbol{r}) = \exp(il_i\phi_{\mathrm{r}})\boldsymbol{v}_j^i(r)$ ($1 \le i \le 4$, $i = \{\sigma, m\}$) with the spin index σ. Substituting these wave functions into the BdG equation (6.1) in the cylindrical coordinates, one can find the relation with respect to the quantum number of the orbital angular momentum such that $n_1 = n_3 = l_1 = l_3 \equiv n$, $n_2 = n_4 = n+1$, $l_2 = l_4 = n-1$. Then, we obtain the following dimensionless BdG equation.

$$\left(\begin{array}{cc} \hat{H}_n(r, \partial_r) & \hat{\Delta}(r) \\ -\hat{\Delta}(r) & -\hat{H}_{-n}(r, \partial_r) \end{array} \right) \left(\begin{array}{c} \boldsymbol{u}_j(r) \\ \boldsymbol{v}_j(r) \end{array} \right) = E_{jn} \left(\begin{array}{c} \boldsymbol{u}_j(r) \\ \boldsymbol{v}_j(r) \end{array} \right),$$

with

$$\hat{H}_n(r, \partial_r) = \xi_{n_i}(r, \partial_r)\sigma_0 \otimes I_{N \times N} + \hat{A}_n(r, \partial_r), \tag{6.4}$$

$$-\hat{H}_{-n}(r, \partial_r) = -\xi_{l_i}(r, \partial_r)\sigma_0 \otimes I_{N \times N} - \hat{A}_{-n}(r, \partial_r), \tag{6.5}$$

$$\xi_{n_i}(r, \partial_r) = -\left(\partial_r^2 + \frac{1}{r}\partial_r - \frac{n_i^2}{r^2}\right) - \mu, \tag{6.6}$$

$$\hat{\Delta}(r) = \begin{pmatrix} f(r)i\sigma_y & 0 \\ 0 & sf(r)i\sigma_y \end{pmatrix}, \tag{6.7}$$

and

$$\hat{A}_n(r, \partial_r) = \begin{pmatrix} -h & -\frac{\alpha}{k_{\rm F}a}\left(\partial_r + \frac{n+1}{r}\right) & t_\perp & 0 \\ \frac{\alpha}{k_{\rm F}a}\left(\partial_r - \frac{n}{r}\right) & h & 0 & t_\perp \\ t_\perp & 0 & -h & \frac{\alpha}{k_{\rm F}a}\left(\partial_r + \frac{n+1}{r}\right) \\ 0 & t_\perp & -\frac{\alpha}{k_{\rm F}a}\left(\partial_r - \frac{n}{r}\right) & h \end{pmatrix}, \tag{6.8}$$

where we have put $\mu/t \to \mu$, $\mu_{\rm B}H/t \to h$, $\alpha/t \to \alpha$, $r/a \to r$, $t_\perp/t \to t_\perp$, $E/t \to E$ and $k_{\rm F}a = 1$.

We take the cut-off radius as $r_{\rm c} = 250a$ and discretize the BdG equation in the real space by the mesh size $0.625a$ (mesh number $N = 400$). Then, we diagonalize the $2^3N \times 2^3N$ BdG Hamiltonian with respect to each quantum number of the angular momentum n. For each n, we arrange the eigen energy E_{jn} $(0 < |j| < 2^3N)$ in ascending order for later discussions.
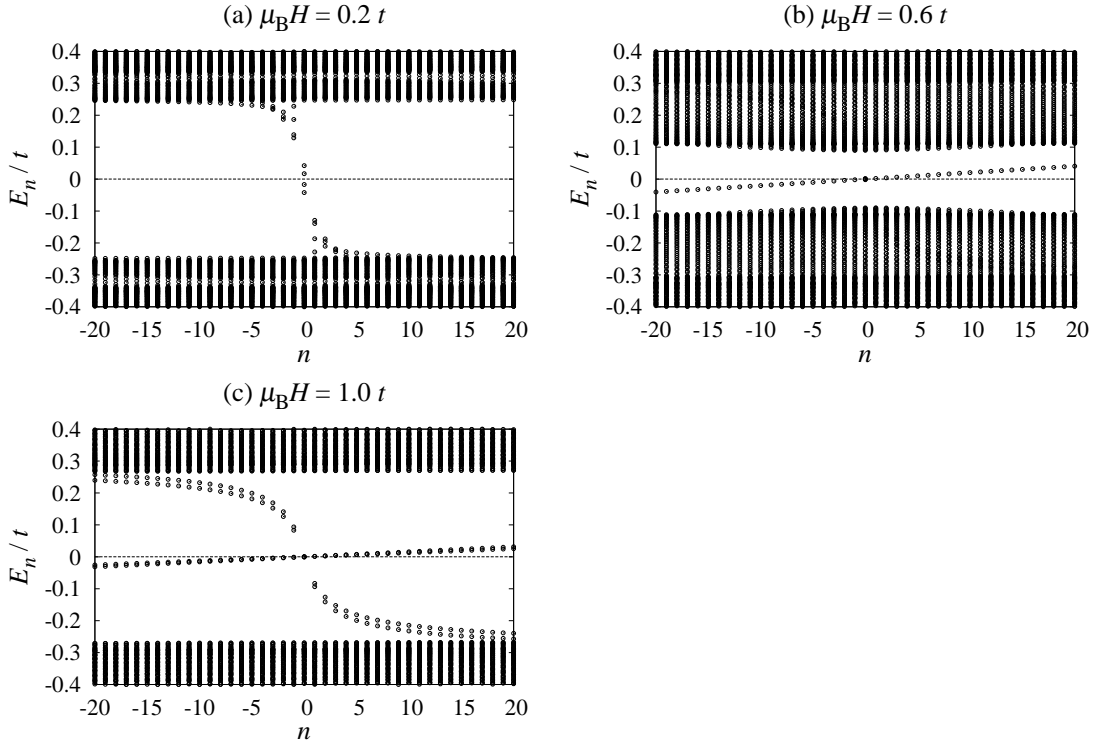
6.3   Results and discussions

Figure 6.1: Energy spectra of Bogoliubov quasiparticles in the PDW state for (a) $\mu_{\rm B}H/t = 0.2$, (b) 0.6 and (c) 1. The horizontal axis n is the quantum number of the angular momentum. We set $\alpha/t = 1$, $t_\perp/t = 0.1$, $\Delta_0/t = 0.35$ and $\mu/t = 0.5$. The dotted lines indicate the zero energy.
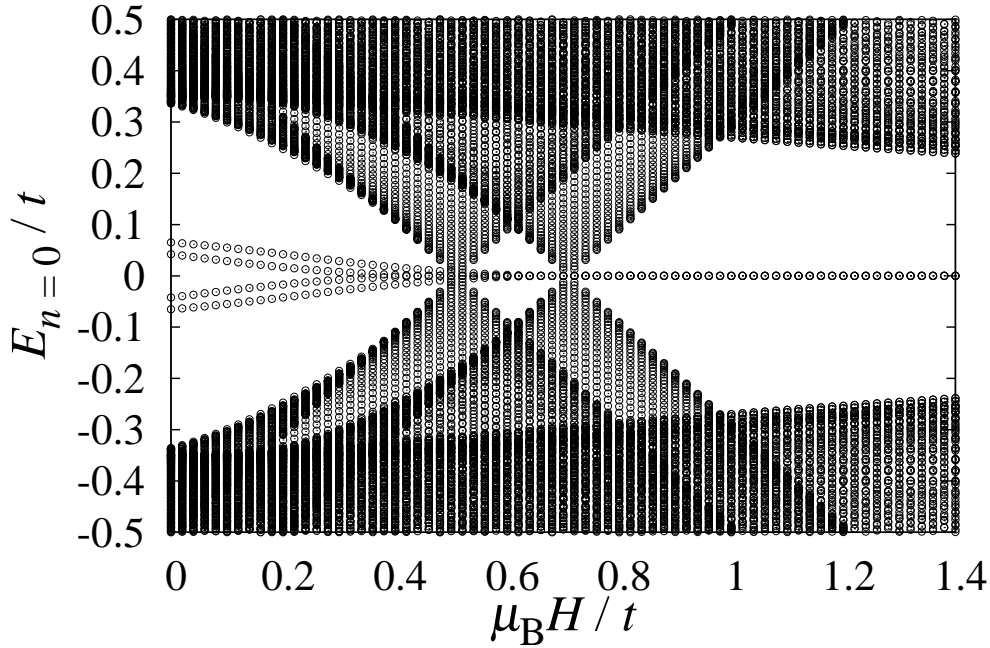
Figure 6.2: Magnetic field dependence of the energy spectra of Bogoliubov quasiparticles with $n = 0$ in the PDW state. We set $\alpha/t = 1$, $t_\perp/t = 0.1$, $\Delta_0/t = 0.35$ and $\mu/t = 0.5$.

Using the mirror symmetry of the system, the BdG Hamiltonian is block-diagonalized [104] and each subsector becomes the Hamiltonian of the noncentrosymmetric superconductor with the Rashba ASOC under effective magnetic fields $\mu_B H \pm t_\perp$ [105]. This system undergoes a topologically non-trivial phase under the sufficiently large effective magnetic field $|\mu_B H \pm t_\perp| > \sqrt{\mu^2 + \Delta_0^2}$ [105, 109, 110]. There are two critical magnetic field values, $h_c^+ \approx 0.5$ and $h_c^- \approx 0.7$ for $\mu/t = 0.5$, $\Delta_0/t = 0.35$ and $t_\perp/t = 0.1$.

First, we show in Fig. 6.1 the energy spectra of Bogoliubov quasiparticles in the PDW state for $\alpha/t = 1$, $t_\perp/t = 0.1$, $\mu/t = 0.5$ and $\Delta_0/t = 0.35$. In the intermediate magnetic field $[h_c^+ < h \ (= 0.6) < h_c^-]$, as shown in Fig. 6.1(b), a single branch of the edge mode appears inside the gap. This is because one mirror sector with the effective magnetic field $\mu_B H + t_\perp$ enters the topologically non-trivial phase. For the low field [e.g., $h \ (= 0.2) < h_c^+$], no edge mode appears [See Fig. 6.1(a)]. On the other hand, in the high magnetic field $[h_c^- < h \ (= 1)]$, two branches of the edge mode appear inside the gap as displayed in Fig. 6.1(c). This indicates that both mirror sectors satisfy the condition of the topologically non-trivial phase. We can also see the vortex bound states [Caroli-de Gennes-Matricon (CdGM) modes] within the superconducting gap in Figs. 6.1(a) and 6.1(c). In Fig. 6.1(b), the CdGM modes are hidden in the continuum spectra except for $E_{1,0}$, since the superconducting gap becomes small in the vicinity of the two critical magnetic fields. The negative slopes of CdGM modes reflect the direction of a magnetic field $[\Delta(\boldsymbol{r}) = \Delta_0(r) \exp(i\phi_r)]$.

Fig. 6.2 shows the magnetic field dependence of the energy spectra for $n = 0$. At the critical field values $[h_c^+ \approx 0.5$ and $h_c^- \approx 0.7]$, the superconducting gap closes. In the low field $h < h_c^+$, there are two finite eigen energies inside the gap in the positive energy side. The lowest one comes from the mirror sector under the effective magnetic field $\mu_B H + t_\perp$ and the other one comes from that with $\mu_B H - t_\perp$. Then, at $h_c^+ \approx 0.5$, the mirror sector under the effective magnetic field $\mu_B H + t_\perp$ enters the topological phase. Subsequently, at $h_c^- \approx 0.7$, the mirror sector under the effective magnetic field $\mu_B H - t_\perp$ undergoes the phase transition into the topological phase. In $h_c^+ < h < h_c^-$, the mirror sector with $\mu_B H + t_\perp$ has the strictly zero eigen energy and in $h > h_c^-$, the both mirror sectors have the strictly zero eigen energy.

Next, we investigate the wave functions belonging to the two lowest eigen energy with $n = 0$.
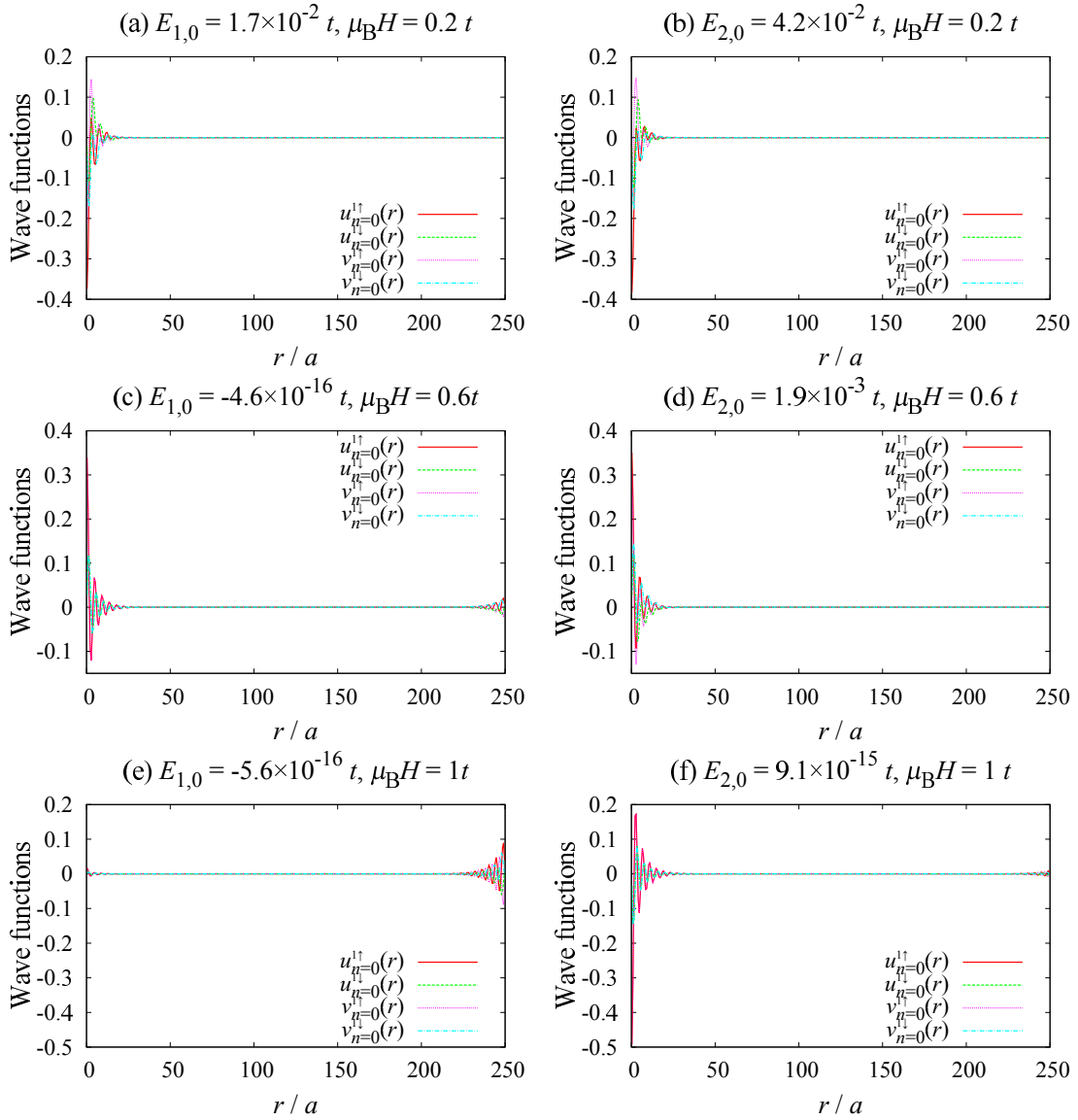
Figure 6.3: Wave functions of Bogoliubov quasiparticles in the PDW state belonging to the lowest eigen energy $E_{1,0}$ and $E_{2,0}$ for $\mu_{\rm B}H/t = 0.2$ [(a), (b)], $\mu_{\rm B}H/t = 0.4$ [(c), (d)] and $\mu_{\rm B}H/t = 1$ [(e), (f)]. We set $\alpha/t = 1$, $t_\perp/t = 0.1$, $\Delta_0/t = 0.35$ and $\mu/t = 0.5$.

Figs. 6.3(a) and 6.3(b) show the wave functions with their eigen energy $E_{1,0} \approx 1.7 \times 10^{-2}t$ and $E_{2,0} \approx 4.2 \times 10^{-2}t$, respectively for $\mu_{\rm B}H/t = 0.2$. We show the wave functions of quasiparticles in the layer 1 only. The quasiparticle wave functions are localized around the vortex and have no amplitude at the edge. This is consistent with Fig. 6.1(a), in which only the vortex bound states appear inside the gap. Then, we consider the intermediate magnetic field regime $[h_{\rm c}^+ < h \ (= 0.6) < h_{\rm c}^-]$. In Fig. 6.3(d), the wave functions with the energy $E_{2,0} \approx 1.9 \times 10^{-3}t$ are localized at the vortex core and have no amplitude at the edge for $\mu_{\rm B}H/t = 0.6$. We can consider that these wave functions are the eigen states of one mirror sector with the effective magnetic field $\mu_{\rm B}H - t_\perp$, that is, the eigen states of the mirror sector in the topologically trivial phase. On the other hand, as show in Fig. 6.3(c), the wave functions with the energy $E_{1,0} \approx -4.6 \times 10^{-16}t$ (i.e., zero energy) are localized both at the vortex core and at the edge. These eigen wave functions correspond to those of one mirror sector with the effective field $\mu_{\rm B}H + t_\perp \approx 0.7t$, which is in the topologically non-trivial phase. The edge bound states appear also in the energy spectra in

Fig. 6.1(b). Next, we consider the high magnetic field regime $[h_c^- < h \ (= 1.0)]$. In this situation, both the mirror sectors are in the topologically non-trivial phase, and so the wave functions with the lowest eigen energies $E_{1,0} \approx -5.6 \times 10^{-16} t$ and $E_{2,0} \approx 9.1 \times 10^{-15} t$ (i.e., zero energies) have the amplitude both at the vortex core and at the edge [see Figs. 6.3(e) and (f)].

6.4 Summary

We have formulated the bilayer Rashba superconductors in the presence of a vortex by means of Bogoliubov-de Gennes theory. We have investigated the energy spectra and the wave functions of bound Bogoliubov quasiparticles at a vortex and an edge in the pair-density wave state. Our calculations of the energy spectra confirm that the branches of the edge mode appear inside the gap if satisfying the condition of the topologically non-trivial phase. We can confirm the appearance of the zero energy vortex and edge quasiparticle states also from the spatial profiles of the zero energy eigen wave functions under the magnetic field above the critical values.

Chapter 7

Conclusions

We have experienced that a variety of superconducting properties appears through vortex core bound states reflecting the internal degree of freedom of the Cooer pair. The experimental approaches to identify the internal degree of freedom of the Cooer pair are proposed in the present dissertation. One is the field-angle dependent flux-flow resistivity measurement by microwaves to probe the phase structure of the Cooper pair and the other is scanning tunneling spectroscopy/microscopy experiment on the vortex core in noncentrosymmetric and locally noncentrosymmetric systems to identify the exotic pairing state due to the spin-orbit coupling. These proposals are based on the microscopically calculated results of the experimentally observable physical quantities. Superconducting materials with their pairing states yet to be identified will be found in the future. It is indispensable to compare the experimental results with the theoretically calculated ones for various physical quantities under various situations to identify the unconventional or exotic superconducting phase. The present dissertation provides the theoretical foundations to identify unconventional superconductivity through vortex core bound states. Unknown exotic superconducting phases and their vortex states will keep exciting our interest.

Bibliography

[1] M. Sigrist and K. Ueda, Rev. Mod. Phys. **63**, 239 (1991).

[2] Y. Yanase, Bussei Kenkyu **3**, 033206 (2014), in Japanese.

[3] C. Caroli, P. G. de Gennes, and J. Matricon, Phys. Lett. **9**, 307 (1964).

[4] L. Kramer and W. Pesch, Z. Physik **269**, 59 (1974).

[5] H. F. Hess, R. B. Robinson, R. C. Dynes, Jr. J. M. Valles, and J. V. Waszczak, Phys. Rev. Lett. **62**, 214 (1989).

[6] F. Gygi and M. Schlüter, Phys. Rev. B **43**, 7609 (1991).

[7] H. F. Hess, R. B. Robinson, and J. V. Waszczak, Phys. Rev. Lett. **64**, 2711 (1990).

[8] N. Hayashi, M. Ichioka, and K. Machida, Phys. Rev. Lett. **77**, 4047 (1996).

[9] N. Hayashi, M. Ichioka, and K. Machida, Phys. Rev. B **56**, 9052 (1997).

[10] Y. Nagai, Y. Ueno, Y. Kato, and N. Hayashi, J. Phys. Soc. Jpn. **75**, 104701 (2006), and references therein.

[11] P. G. de Gennes, *Superconductivity of Metals and Alloys*, Addison-Wesley, 1966.

[12] M. Tinkham, *Introduction to Superconductivity*, McGraw-Hill, 1996.

[13] K. Yamada and T. Ohmi, *Superfluidity*, Baifu-kan, 1995, in Japanese.

[14] N. Hayashi and M. Sigrist, Kotaibutsuri (Solid State Physics) **41**, 631 (2006), in Japanese.

[15] Y. Yanase and H. Harima, Kotaibutsuri (Solid State Physics) **46**, 283 (2011), in Japanese.

[16] P. A. Frigeri, D. F. Agterberg, and M. Sigrist, New J. Phys. **6**, 115 (2004).

[17] P. A. Frigeri, D. F. Agterberg, A. Koga, and M. Sigrist, Phys. Rev. Lett. **92**, 097001 (2004).

[18] J. J. Sakurai, *Modern Quantum Mechanics*, Addison-Wesley, 1994.

[19] P. W. Anderson, J. Phys. Chem. Solids **11**, 26 (1959).

[20] P. W. Anderson, Phys. Rev. B **30**, 4000 (1984).

[21] S. Yasuzuka, S. Uji, Y. Yamamura, K. Saitoh, and J. Yamada, Abstract of the 16th Domestic Workshop on Vortex Physics, Dec. 2008.

[22] S. Yasuzuka, S. Uji, H. Satsukawa, M. Kimata, T. Terashima, H. Koga, Y. Yamamura, K. Saito, H. Akutsu, and J. Yamada, Physica B **405**, S288 (2010).

[23] S. Yasuzuka, K. Saito, S. Uji, M. Kimata, H. Satsukawa, T. Terashima, and J. Yamada, J. Phys. Soc. Jpn. **82**, 064716 (2013).

[24] S. Yasuzuka, S. Uji, T. Terashima, S. Tsuchiya, K. Sugii, B. Zhou, A. Kobayashi, and H. Kobayashi, J. Phys. Soc. Jpn. **83**, 013705 (2014).

[25] K. Takanaka and K. Kuboya, Phys. Rev. Lett. **75**, 323 (1995).

[26] P. Miranović, N. Nakai, M. Ichioka, and K. Machida, Phys. Rev. B **68**, 052501 (2003).

[27] Y. Kato, J. Phys. Soc. Jpn. **69**, 3378 (2000).

[28] P. A. Frigeri, D. F. Agterberg, I. Milat, and M. Sigrist, Eur. Phys. J. B **54**, 435 (2006).

[29] N. Hayashi, K. Wakabayashi, P. A. Frigeri, and M. Sigrist, Phys. Rev. B **73**, 024504 (2006).

[30] N. Hayashi, Y. Kato, P. A. Frigeri, K. Wakabayashi, and M. Sigrist, Physica C **437**, 96 (2006).

[31] H. Yavari and M. Nemati, J. Low Temp. Phys. **166**, 90 (2012).

[32] V. M. Edelstein, Phys. Rev. B **78**, 094514 (2008).

[33] H. Yavari and M. Erfan, Solid State Commun. **150**, 2049 (2010).

[34] V. P. Mineev and K. V. Samokhin, Phys. Rev. B **75**, 184529 (2007).

[35] G Bao, Y. Inada, S. Harada, and G. q. Zheng, J. Phys: Conf. Ser. **391**, 012084 (2012).

[36] G Bao, Y. Inada, G. Eguchi, Y. Maeno, M. Ichioka, and G. q. Zheng, J. Phys: Conf. Ser. **391**, 012084 (2012).

[37] As pointed out by Hayashi [111], the condition that the Green's functions are invariant under $\bm{k} \to -\bm{k}$ is satisfied at least in spatially uniform systems, when the superconducting order parameters on the split two Fermi surfaces, $\Delta_{\mathrm{I,II}}$, are invariant under $\bm{k} \to -\bm{k}$. Now the superconducting order parameters, $\Delta_{\mathrm{I,II}}$, have the rotational symmetry about the k_z axis ($k_z \parallel z$), and the mirror symmetry about the k_x-k_y plane [92]. Then, the bulk Green's functions satisfy the condition. However, the condition is not satisfied in systems in the presence of the superflow (for instance, around a vortex core) or in the helical vortex phase (the helicity $\bm{q}$ violates the isotropy of the system) [45, 82], namely the Green's functions are not invariant under $\bm{k} \to -\bm{k}$ in such systems.

[38] Z. Sun, M. Enayat, A. Maldonado, C. Lithgow, E. Yelland, D. C. Peets, A. Yaresko, A. P. Schnyder, and P. Wahl, arXiv:1407.5667.

[39] T. Yoshida, D. Maruyama, and Y. Yanase, Kotaibutsuri (Solid State Physics) **49**, 109 (2014), in Japanese.

[40] M. Sigrist, D. F. Agterberg, M. H. Fischer, J. Goryo, F. Loder, S. H. Rhim, D. Maruyama, Y. Yanase, T. Yoshida, and S. J. Youn, J. Phys. Soc. Jpn. **83**, 061014 (2014).

[41] Y. Yanase, J. Phys. Soc. Jpn. **79**, 084701 (2010).

[42] T. Yoshida, M. Sigrist, and Y. Yanase, Phys. Rev. B **86**, 134514 (2012).

[43] T. Yoshida, M. Sigrist, and Y. Yanase, J. Phys. Soc. Jpn. **82**, 074714 (2013).

[44] Y. Matsuda and H. Shimahara, J. Phys. Soc. Jpn. **76**, 051005 (2007).

[45] R. P. Kaur, D. F. Agterberg, and M. Sigrist, Phys. Rev. Lett. **94**, 137002 (2005).

[46] M. Mugikura, Ph.D. thesis, Tohoku University, 2007.

[47] Y. Nagai, unpublished.

[48] U. Eckern and A. Schmid, J. Low. Temp. Phys. **45**, 137 (1981).

[49] J. W. Serene and D. Rainer, Phys. Rep. **101**, 221 (1983), and references cited therein.

[50] N. B. Kopnin, J. Low. Temp. Phys. **97**, 157 (1994).

[51] N. B. Kopnin, *Theory of Nonequilibrium Superconductivity*, Oxford University Press, 2001.

[52] T. Sakakibara, A. Yamada, J. Custers, K. Yano, T. Tayama, H. Aoki, and K. Machida, J. Phys. Soc. Jpn. **76**, 051004 (2007).

[53] Y. Matsuda, K. Izawa, and I. Vekhter, J. Phys.: Condens. Matter **18**, R705 (2006).

[54] A. B. Vorontsov and I Vekhter, Physical Review B **75**, 224501 (2007).

[55] A. B. Vorontsov and I Vekhter, Physical Review B **75**, 224502 (2007).

[56] C. C. Tsuei, J. R. Kirtley, C. C. Chi, L. S. Yu-Jahnes, A. Gupta, T. Shaw, J. Z. Sun, and M. B. Ketchen, Phys. Rev. Lett. **73**, 593 (1994).

[57] T. Hanaguri, S. Nittaka, K. Kuroki, and H. Takagi, Science **328**, 474 (2010).

[58] D. J. Van Harlingen, Rev. Mod. Phys. **67**, 515 (1995).

[59] C. C. Tsuei and J. R. Kirtley, Rev. Mod. Phys. **72**, 969–1016 (2000).

[60] N. B. Kopnin and G. E. Volovik, Phys. Rev. Lett. **79**, 1377 (1997).

[61] Yu. G. Makhlin, Phys. Rev. B **56**, 11872 (1997).

[62] N. B. Kopnin, G. E. Volovik, and Ü. Parts, Europhys. Lett. **32**, 651 (1995).

[63] Alan T. Dorsey, Phys. Rev. B **46**, 8376 (1992).

[64] Y. Higashi, Y. Nagai, M. Machida, and N. Hayashi, J. Phys: Conf. Ser. **400**, 022025 (2012).

[65] G. E. Volovik, Pis'ma Zh. Eksp. Teor. Fiz. **58**, 444 (1993).

[66] G. E. Volovik, Pis'ma Zh. Eksp. Teor. Fiz. **70**, 601 (1999).

[67] N. B. Kopnin and G. E. Volovik, Pis'ma Zh. Eksp. Teor. Fiz. **64**, 641 (1996).

[68] Y. Nagai and N. Hayashi, Phys. Rev. Lett. **101**, 097001 (2008).

[69] Y. Nagai and Y. Kato, Phys. Rev. B **82**, 174507 (2010).

[70] L. J. Buchholtz and G. Zwicknagl, Phys. Rev. B **23**, 5788 (1981).

[71] E. V. Thuneberg, J. Kurkijärvi, and D. Rainer, Phys. Rev. B **29**, 3913 (1984).

[72] N. Hayashi, Y. Kato, and M. Sigrist, J. Low Temp. Phys. **139**, 79 (2005).

[73] Y. Higashi, Y. Nagai, M. Machida, and N. Hayashi, Physica C **471**, 828 (2011).

[74] Y. Higashi, Y. Nagai, M. Machida, and N. Hayashi, Physica C **484**, 97 (2013).

[75] J. Sadowski, Master thesis, University of Saskatchewan, 2011.

[76] N. W. Ashcroft and N. D. Mermin, *Solid State Physics*, Thomson Learning, 1976.

[77] I. Vekhter and A. Vorontsov, Physica B **403**, 958 (2008).

[78] We rotate the model FS given in Ref. [77] by $\pi/4$ [rad] within the k_x-k_y plane in order to compare the result for FS II with that for FS I.

[79] B. Zeng, G. Mu, H. Q. Luo, T. Xiang, I. I. Mazin, H. Yang, L. Shan, C. Ren, P. C. Dai, and H.-H. Wen, Nat. Commun. **1**, 112 (2010).

[80] M. Yamashita, Y. Senshu, T. Shibauchi, S. Kasahara, K. Hashimoto, D. Watanabe, H. Ikeda, T. Terashima, I. Vekhter, A. B. Vorontsov, and Y. Matsuda, Phys. Rev. B **84**, 060507(R) (2011).

[81] Y. Higashi, Y. Nagai, M. Machida, and N. Hayashi, Phys. Proc. **45**, 137 (2013).

[82] D. F. Agterberg and R. P. Kaur, Phys. Rev. B **75**, 064511 (2007).

[83] Y. Matsunaga, N. Hiasa, and R. Ikeda, Phys. Rev. B **78**, 220508(R) (2008).

[84] K. Aoyama and M. Sigrist, Phys. Rev. Lett. **109**, 237007 (2012).

[85] S. K. Yip, J. Low Temp. Phys. **140**, 67 (2005).

[86] C. K. Liu and S. Yip, Phys. Rev B **82**, 104501 (2010).

[87] D. Maruyama, M. Sigrist, and Y. Yanase, J. Phys. Soc. Jpn. **81**, 034702 (2012).

[88] N. Schopohl, J. Low Temp. Phys. **41**, 409 (1980).

[89] J. A. X. Alexander, T. P. Orlando, D. Rainer, and P. M. Tedrow, Phys. Rev. B **31**, 5811 (1985).

[90] C. T. Rieck, K. Scharnberg, and N. Schopohl, J. Low Temp. Phys. **84**, 381 (1991).

[91] C. H. Choi and J. A. Sauls, Phys. Rev. B **48**, 13684 (1993).

[92] N. Hayashi, K. Wakabayashi, P. A. Frigeri, and M. Sigrist, Phys. Rev. B **73**, 092508 (2006).

[93] W. H. Press, S. A. Teukolsky, W. T. Vetterling, and B. P. Flannery, *Numerical Recipes in FORTRAN 77*, Cambridge University Press, second edition.

[94] N. Hayashi and Y. Kato, J. Low Temp. Phys. **130**, 193 (2003).

[95] N. Hayashi, Y. Higashi, N. Nakai, and H. Suematsu, Physica C **484**, 69 (2013).

[96] H. Mukuda, S. Shimizu, A. Iyo, and Y. Kitaoka, J. Phys. Soc. Jpn **81**, 011008 (2012), and references cited therein.

[97] Y. S. Hor, A. J. Williams, J. G. Checkelsky, P. Roushan, J. Seo, Q. Xu, H. W. Zandbergen, A. Yazdani, N. P. Ong, and R. J. Cava, Phys. Rev. Lett. **104**, 057001 (2010).

[98] Y. Nishikubo, K. Kudo, and M. Nohara, J. Phys. Soc. Jpn. **80**, 055002 (2011).

[99] Y. Mizukami, H. Shishido, T. Shibauchi, M. Shimozawa, S. Yasumoto, D. Watanabe, M. Yamashita, H. Ikeda, T. Terashima, H. Kontani, , and Y. Matsuda, Nat. Phys. **7**, 849 (2011).

[100] M. Shimozawa, S. K. Goh, R. Endo, R. Kobayashi, T. Watashige, Y. Mizukami, H. Ikeda, H. Shishido, Y. Yanase, T. Terashima, T. Shibauchi, and Y. Matsuda, Phys. Rev. Lett. **112**, 156404 (2014).

[101] Y. Higashi, Y. Nagai, and N. Hayashi, JPS Conf. Proc. **3**, 015003 (2014).

[102] T. Yoshida, M. Sigrist, and Y. Yanase, JPS Conf. Proc. **3**, 015026 (2014).

[103] K. An, T. Sakakibara, R. Settai, Y. Onuki, M. Hiragi, M. Ichioka, and K. Machida, Phys. Rev. Lett. **104**, 037202 (2010).

[104] Y. Ueno, A. Yamakage, Y. Tanaka, and M. Sato, Phys. Rev. Lett. **111**, 087002 (2013).

[105] T. Yoshida, M. Sigrist, and Y. Yanase, unpublished.

[106] M. Ichioka, H. Adachi, T. Mizushima, and K. Machida, Phys. Rev. B **76**, 014503 (2007).

[107] M. Ichioka and K. Machida, Phys. Rev. B **76**, 064502 (2007).

[108] S. K. Goh, Y. Mizukami, H. Shishido, D. Watanabe, S. Yasumoto, M. Shimozawa, M. Yamashita, T. Terashima, Y. Yanase, T. Shibauchi, A. I. Buzdin, and Y. Matsuda, Phys. Rev. Lett. **109**, 157006 (2012).

[109] M. Sato, Y. Takahashi, and S. Fujimoto, Phys. Rev. Lett. **103**, 020401 (2009).

[110] S. Tewari, T. D. Stanescu, J. D. Sau, and S. Das Sarma, New J. Phys. **13**, 065004 (2011).

[111] N. Hayashi, unpublished.

[112] M. Eschrig, Phys. Rev. B **61**, 9061 (2000).

[113] Y. Nagai, Master thesis, The University of Tokyo, 2007, in Japanese.

Appendix A

Spin-triplet Pairing: Vector Order Parameter

In this appendix, we see how the order parameter is changed by the rotation in spin space. We know that the angular momentum is the generator of a rotation. Consider the following unitary matrix for a rotation about the axis characterized by a unit vector $\tilde{\boldsymbol{n}}$ by an infinitesimal angle $\delta\phi$:

$$\mathscr{D}(\tilde{\boldsymbol{n}}, \delta\phi) = 1 - i\frac{\boldsymbol{J}\cdot\tilde{\boldsymbol{n}}}{\hbar}\delta\phi. \tag{A.1}$$

$\boldsymbol{J}$ is the angular momentum operator. For spin $1/2$ particles, we have the rotation operator of the order parameter in spin space

$$\hat{\mathscr{D}}(\tilde{\boldsymbol{n}}, \delta\phi) = \hat{\sigma}_0 - \frac{i}{2}\delta\phi\tilde{\boldsymbol{n}}\cdot\hat{\boldsymbol{\sigma}}, \tag{A.2}$$

where $\hat{\ }$ indicates the 2×2 matrix in spin space. For the order parameter in spin space

$$\hat{\Delta} = \begin{pmatrix} \Delta_{\uparrow\uparrow} & \Delta_{\uparrow\downarrow} \\ \Delta_{\downarrow\uparrow} & \Delta_{\downarrow\downarrow} \end{pmatrix}, \tag{A.3}$$

we conduct the rotational transformation.

$$
\begin{aligned}
\hat{\mathscr{D}}(\tilde{\boldsymbol{n}}, \delta\phi)\hat{\Delta}\hat{\mathscr{D}}^{\mathrm{T}}(\tilde{\boldsymbol{n}}, \delta\phi) &= \left[\hat{\sigma}_0 - \frac{i}{2}\delta\phi\tilde{\boldsymbol{n}}\cdot\hat{\boldsymbol{\sigma}}\right]\hat{\Delta}\left[\hat{\sigma}_0 - \frac{i}{2}\delta\phi\tilde{\boldsymbol{n}}\cdot\hat{\boldsymbol{\sigma}}\right]^{\mathrm{T}} \\
&= \hat{\Delta} - \hat{\Delta}\left(\frac{i}{2}\delta\phi\tilde{\boldsymbol{n}}\cdot\hat{\boldsymbol{\sigma}}^{\mathrm{T}}\right) - \frac{i}{2}\delta\phi\tilde{\boldsymbol{n}}\cdot\hat{\boldsymbol{\sigma}}\hat{\Delta} + o\left(\delta\phi^2\right) \\
&= \hat{\Delta} - \frac{i}{2}\delta\phi\tilde{\boldsymbol{n}}\cdot\left(\hat{\boldsymbol{\sigma}}\hat{\Delta} - \hat{\Delta}\hat{\sigma}_y\hat{\boldsymbol{\sigma}}\hat{\sigma}_y\right) + o\left(\delta\phi^2\right).
\end{aligned} \tag{A.4}
$$

Here we used the relation $\hat{\boldsymbol{\sigma}}^{\mathrm{T}} = -\hat{\sigma}_y\hat{\boldsymbol{\sigma}}\hat{\sigma}_y$. Hence, it turned out that under rotation in spin space the order parameter is transformed into as follows:

$$
\begin{aligned}
\hat{\Delta}' &= \hat{\mathscr{D}}(\tilde{\boldsymbol{n}}, \delta\phi)\hat{\Delta}\hat{\mathscr{D}}^{\mathrm{T}}(\tilde{\boldsymbol{n}}, \delta\phi) \\
&= \hat{\Delta} - \frac{i}{2}\delta\phi\tilde{\boldsymbol{n}}\cdot\left(\hat{\boldsymbol{\sigma}}\hat{\Delta}\hat{\sigma}_y - \hat{\Delta}\hat{\sigma}_y\hat{\boldsymbol{\sigma}}\right)\hat{\sigma}_y + o\left(\delta\phi^2\right).
\end{aligned} \tag{A.5}
$$

For spin-singlet pair, $\Delta_{\uparrow\uparrow} = \Delta_{\downarrow\downarrow} = 0$ and $\Delta_{\uparrow\downarrow}(\equiv \Delta) = -\Delta_{\downarrow\uparrow}$. Then the pairing state is written as $\hat{\Delta} = \Delta i\hat{\sigma}_y$. The state vector of a spin-singlet pairing is expressed as $|\Psi\rangle = \Delta(|\uparrow\downarrow\rangle - |\downarrow\uparrow\rangle)$. $|ss'\rangle$ represents the spin state of a Cooper pair $(|\uparrow\uparrow\rangle : S_z = 1, |\uparrow\downarrow\rangle, |\downarrow\uparrow\rangle : S_z = 0, |\downarrow\downarrow$

$\rangle : S_z = -1$). Performing the rotation in spin space for the spin-singlet order parameter, we have

$$
\begin{aligned}
\hat{\Delta}' &= \hat{\mathscr{D}}(\tilde{\boldsymbol{n}}, \delta\phi)\hat{\Delta}\hat{\mathscr{D}}^{\mathrm{T}}(\tilde{\boldsymbol{n}}, \delta\phi) \\
&= (\Delta i\hat{\sigma}_y) - \frac{i}{2}\delta\phi\tilde{\boldsymbol{n}} \cdot [\hat{\boldsymbol{\sigma}}\,(\Delta i\hat{\sigma}_y)\,\hat{\sigma}_y - (\Delta i\hat{\sigma}_y)\,\hat{\sigma}_y\hat{\boldsymbol{\sigma}}]\,\hat{\sigma}_y \\
&= \Delta i\hat{\sigma}_y + \frac{1}{2}\delta\phi\Delta\tilde{\boldsymbol{n}} \cdot (\hat{\boldsymbol{\sigma}} - \hat{\boldsymbol{\sigma}})\,\hat{\sigma}_y \\
&= \Delta i\hat{\sigma}_y \\
&= \hat{\Delta}. \qquad (A.6)
\end{aligned}
$$

Therefore, the spin-singlet order parameter is not changed under rotation in spin space.

For spin-triplet pair, $\Delta_{\uparrow\downarrow} = \Delta_{\downarrow\uparrow} \equiv \Delta_0$, $\Delta_{\uparrow\uparrow} = \Delta_{\downarrow\downarrow} \neq 0$. The state vector of a spin-triplet pairing is $|\Psi\rangle = \Delta_{\uparrow\uparrow}|\uparrow\uparrow\rangle + \Delta_0(|\uparrow\downarrow\rangle + |\downarrow\uparrow\rangle) + \Delta_{\downarrow\downarrow}|\downarrow\downarrow\rangle$. We here consider the transformation of the spin quantization axis. It is convenient to express the state vector of the pairing state as the three dimensional vector under rotation in spin space. We consider the following bases:

$$
|S_z = 0\rangle = \frac{1}{\sqrt{2}}(|\uparrow\downarrow\rangle + |\downarrow\uparrow\rangle), \qquad (A.7)
$$

$$
|S_x = 0\rangle = \frac{1}{\sqrt{2}}(-|\uparrow\uparrow\rangle + |\downarrow\downarrow\rangle), \qquad (A.8)
$$

$$
|S_y = 0\rangle = \frac{i}{\sqrt{2}}(|\uparrow\uparrow\rangle + |\downarrow\downarrow\rangle). \qquad (A.9)
$$

Using these bases, the state vector of a spin-triplet pairing is written as

$$
|\Psi\rangle = \sqrt{2}\left[-\frac{\Delta_{\uparrow\uparrow} - \Delta_{\downarrow\downarrow}}{2}|S_x = 0\rangle + \frac{\Delta_{\uparrow\uparrow} + \Delta_{\downarrow\downarrow}}{2i}|S_y = 0\rangle + \Delta_0|S_z = 0\rangle\right], \qquad (A.10)
$$

$$
\equiv \sqrt{2}\left[d_x|S_x = 0\rangle + d_y|S_y = 0\rangle + d_z|S_z = 0\rangle\right], \qquad (A.11)
$$

$$
= \sqrt{2}\boldsymbol{d} \qquad (A.12)
$$

Here we define $\Delta_{\uparrow\uparrow} = -d_x + id_y$, $\Delta_{\downarrow\downarrow} = d_x + id_y$, $\Delta_0 = d_z$. The vector $\boldsymbol{d}$, which is called d vector, is often used as the vector order parameter instead of $\boldsymbol{\Delta}$. Using the d vector, the spin-triplet order parameter is expressed as $\hat{\Delta} = (\boldsymbol{d} \cdot \hat{\boldsymbol{\sigma}})i\hat{\sigma}_y$. Under the rotation in spin space, the vector order parameter $\boldsymbol{\Delta} = (\Delta_x, \Delta_y, \Delta_z)$ for a spin-triplet pair is transformed as

$$
\begin{aligned}
\hat{\Delta}' &= \hat{\mathscr{D}}(\tilde{\boldsymbol{n}}, \delta\phi)\hat{\Delta}\hat{\mathscr{D}}^{\mathrm{T}}(\tilde{\boldsymbol{n}}, \delta\phi) \\
&= (\boldsymbol{\Delta} \cdot \hat{\boldsymbol{\sigma}}i\hat{\sigma}_y) - \frac{i}{2}\delta\phi\tilde{\boldsymbol{n}} \cdot [\hat{\boldsymbol{\sigma}}\,(\boldsymbol{\Delta} \cdot \hat{\boldsymbol{\sigma}}i\hat{\sigma}_y)\,\hat{\sigma}_y - (\boldsymbol{\Delta} \cdot \hat{\boldsymbol{\sigma}}i\hat{\sigma}_y)\,\hat{\sigma}_y\hat{\boldsymbol{\sigma}}]\,\hat{\sigma}_y + o\left(\delta\phi^2\right) \\
&= \boldsymbol{\Delta} \cdot \hat{\boldsymbol{\sigma}}i\hat{\sigma}_y - \frac{i}{2}\delta\phi\tilde{\boldsymbol{n}} \cdot [\hat{\boldsymbol{\sigma}}\,(\boldsymbol{\Delta} \cdot \hat{\boldsymbol{\sigma}}) - (\boldsymbol{\Delta} \cdot \hat{\boldsymbol{\sigma}})\,\hat{\boldsymbol{\sigma}}]\,i\hat{\sigma}_y + o\left(\delta\phi^2\right) \\
&= \boldsymbol{\Delta} \cdot \hat{\boldsymbol{\sigma}}i\hat{\sigma}_y - \frac{i}{2}\delta\phi\tilde{\boldsymbol{n}} \cdot 2i\boldsymbol{\Delta} \times \hat{\boldsymbol{\sigma}}i\hat{\sigma}_y + o\left(\delta\phi^2\right) \\
&= \boldsymbol{\Delta} \cdot \hat{\boldsymbol{\sigma}}i\hat{\sigma}_y + \delta\phi\tilde{\boldsymbol{n}} \cdot \boldsymbol{\Delta} \times \hat{\boldsymbol{\sigma}}i\hat{\sigma}_y + o\left(\delta\phi^2\right) \\
&= \boldsymbol{\Delta} \cdot \hat{\boldsymbol{\sigma}}i\hat{\sigma}_y + \delta\phi\,(\tilde{\boldsymbol{n}} \times \boldsymbol{\Delta}) \cdot \hat{\boldsymbol{\sigma}}i\hat{\sigma}_y + o\left(\delta\phi^2\right) \\
&= [\boldsymbol{\Delta} + \delta\phi\,(\tilde{\boldsymbol{n}} \times \boldsymbol{\Delta})] \cdot \hat{\boldsymbol{\sigma}}i\hat{\sigma}_y + o\left(\delta\phi^2\right). \qquad (A.13)
\end{aligned}
$$

Thus, the vector order parameter $\boldsymbol{\Delta}$ certainly behaves as the three dimensional vector under the transformation of the spin quantization axis.

Appendix B

Moyal Product

We would like to obtain the Wigner representation of the following quantity:

$$\check{C}(\boldsymbol{r}, \boldsymbol{r}', i\omega_n) = \int d\boldsymbol{r}'' \check{A}(\boldsymbol{r}, \boldsymbol{r}'', i\omega_n) \check{B}(\boldsymbol{r}'', \boldsymbol{r}', i\omega_n). \tag{B.1}$$

Here, $\check{X}$ indicates the Green's function in Numbu space. To obtain the Wigner representation $\check{C}(\boldsymbol{R}, \bar{\boldsymbol{k}}, i\omega_n)$, we first write $\check{A}(\boldsymbol{r}, \boldsymbol{r}'', i\omega_n)$ and $\check{B}(\boldsymbol{r}'', \boldsymbol{r}', i\omega_n)$ in the Wigner representation.

$$
\begin{aligned}
\check{C}(\boldsymbol{r}, \boldsymbol{r}', i\omega_n) &= \int d\boldsymbol{r}'' \check{A}\left(\boldsymbol{R}' = \frac{\boldsymbol{r} + \boldsymbol{r}''}{2}, \bar{\boldsymbol{r}}' = \boldsymbol{r} - \boldsymbol{r}'', i\omega_n\right) \check{B}\left(\boldsymbol{R}'' = \frac{\boldsymbol{r}'' + \boldsymbol{r}'}{2}, \bar{\boldsymbol{r}}'' = \boldsymbol{r}'' - \boldsymbol{r}', i\omega_n\right) \\
&= \int d\boldsymbol{r}'' \int \frac{d\bar{\boldsymbol{k}}'}{(2\pi)^3} \int \frac{d\bar{\boldsymbol{k}}''}{(2\pi)^3} e^{i\bar{\boldsymbol{k}}' \cdot (\boldsymbol{r} - \boldsymbol{r}'')} e^{i\bar{\boldsymbol{k}}'' \cdot (\boldsymbol{r}'' - \boldsymbol{r}')} \check{A}\left(\boldsymbol{R}', \bar{\boldsymbol{k}}', i\omega_n\right) \check{B}\left(\boldsymbol{R}'', \bar{\boldsymbol{k}}'', i\omega_n\right) \\
&= \int d\boldsymbol{r}'' \int \frac{d\bar{\boldsymbol{k}}'}{(2\pi)^3} \int \frac{d\bar{\boldsymbol{k}}''}{(2\pi)^3} e^{i\bar{\boldsymbol{k}}' \cdot (\boldsymbol{r} - \boldsymbol{r}'')} e^{i\bar{\boldsymbol{k}}'' \cdot (\boldsymbol{r}'' - \boldsymbol{r}')} \\
&\quad \times \check{A}\left(\boldsymbol{R} + \frac{\boldsymbol{r}'' - \boldsymbol{r}'}{2}, \bar{\boldsymbol{k}}', i\omega_n\right) \check{B}\left(\boldsymbol{R} - \frac{\boldsymbol{r} - \boldsymbol{r}''}{2}, \bar{\boldsymbol{k}}'', i\omega_n\right)
\end{aligned} \tag{B.2}
$$

Here $\boldsymbol{R} = (\boldsymbol{r} + \boldsymbol{r}')/2$ and we decomposed the arguments of $\check{A}$ and $\check{B}$ as $\check{A}(\boldsymbol{R}') = \check{A}(\boldsymbol{R} + (\boldsymbol{R}' - \boldsymbol{R}))$ and $\check{B}(\boldsymbol{R}'') = \check{B}(\boldsymbol{R} + (\boldsymbol{R}'' - \boldsymbol{R}))$, respectively. Then, we expand $\check{A}$ and $\check{B}$ in the vicinity of $\boldsymbol{R}$.

$$
\begin{aligned}
\check{C}(\boldsymbol{r}, \boldsymbol{r}', i\omega_n) &= \int d\boldsymbol{r}'' \int \frac{d\bar{\boldsymbol{k}}'}{(2\pi)^3} \int \frac{d\bar{\boldsymbol{k}}''}{(2\pi)^3} e^{i\bar{\boldsymbol{k}}' \cdot (\boldsymbol{r} - \boldsymbol{r}'')} e^{i\bar{\boldsymbol{k}}'' \cdot (\boldsymbol{r}'' - \boldsymbol{r}')} \\
&\quad \times \sum_{n=0}^{\infty} \frac{1}{n!} \left.\frac{\partial^n \check{A}(\boldsymbol{R}', \bar{\boldsymbol{k}}', i\omega_n)}{\partial \boldsymbol{R}'^n}\right|_{\boldsymbol{R}'=\boldsymbol{R}} (\boldsymbol{R}' - \boldsymbol{R})^n \\
&\quad \times \sum_{m=0}^{\infty} \frac{1}{m!} \left.\frac{\partial^m \check{B}(\boldsymbol{R}'', \bar{\boldsymbol{k}}'', i\omega_n)}{\partial \boldsymbol{R}''^m}\right|_{\boldsymbol{R}''=\boldsymbol{R}} (\boldsymbol{R}'' - \boldsymbol{R})^m
\end{aligned} \tag{B.3}
$$

Using the following relations

$$e^{i\bar{\boldsymbol{k}}'' \cdot (\boldsymbol{r}'' - \boldsymbol{r}')} (\boldsymbol{R}' - \boldsymbol{R})^n = \left(\frac{1}{2i}\right)^n \frac{\partial^n}{\partial \bar{\boldsymbol{k}}''^n} e^{i\bar{\boldsymbol{k}}'' \cdot (\boldsymbol{r}'' - \boldsymbol{r}')}, \tag{B.4}$$

$$e^{i\bar{\boldsymbol{k}}' \cdot (\boldsymbol{r} - \boldsymbol{r}'')} (\boldsymbol{R}'' - \boldsymbol{R})^m = \left(\frac{-1}{2i}\right)^m \frac{\partial^m}{\partial \bar{\boldsymbol{k}}'^m} e^{i\bar{\boldsymbol{k}}' \cdot (\boldsymbol{r} - \boldsymbol{r}'')}, \tag{B.5}$$

we obtain

$$
\check{C}(\boldsymbol{r}, \boldsymbol{r}', i\omega_n) = \int d\boldsymbol{r}'' \int \frac{d\bar{\boldsymbol{k}}'}{(2\pi)^3} \int \frac{d\bar{\boldsymbol{k}}''}{(2\pi)^3}
$$

$$
\times \sum_{n=0}^{\infty} \frac{1}{n!} \left.\frac{\partial^n \check{A}(\boldsymbol{R}', \bar{\boldsymbol{k}}', i\omega_n)}{\partial \boldsymbol{R}'^n}\right|_{\boldsymbol{R}'=\boldsymbol{R}} \left(\frac{1}{2i}\right)^n \frac{\partial^n}{\partial \bar{\boldsymbol{k}}''^n} e^{i\bar{\boldsymbol{k}}''\cdot(\boldsymbol{r}''-\boldsymbol{r}')}
$$

$$
\times \sum_{m=0}^{\infty} \frac{1}{m!} \left.\frac{\partial^m \check{B}(\boldsymbol{R}'', \bar{\boldsymbol{k}}'', i\omega_n)}{\partial \boldsymbol{R}''^m}\right|_{\boldsymbol{R}''=\boldsymbol{R}} \left(\frac{-1}{2i}\right)^m \frac{\partial^m}{\partial \bar{\boldsymbol{k}}'^m} e^{i\bar{\boldsymbol{k}}'\cdot(\boldsymbol{r}-\boldsymbol{r}'')}
$$

$$
= \int d\boldsymbol{r}'' \sum_{n=0}^{\infty} \sum_{m=0}^{\infty} \frac{1}{n!}\frac{1}{m!} \left(\frac{1}{2i}\right)^n \left(\frac{-1}{2i}\right)^m
$$

$$
\times \int \frac{d\boldsymbol{k}'}{(2\pi)^3} \left.\frac{\partial^n}{\partial \boldsymbol{R}'^n} \check{A}(\boldsymbol{R}', \bar{\boldsymbol{k}}', i\omega_n)\right|_{\boldsymbol{R}'=\boldsymbol{R}} \frac{\partial^m}{\partial \bar{\boldsymbol{k}}'^m} e^{i\bar{\boldsymbol{k}}'\cdot(\boldsymbol{r}-\boldsymbol{r}'')} \tag{B.6}
$$

$$
\times \int \frac{d\boldsymbol{k}''}{(2\pi)^3} \left.\frac{\partial^m}{\partial \boldsymbol{R}''^m} \check{B}(\boldsymbol{R}'', \bar{\boldsymbol{k}}'', i\omega_n)\right|_{\boldsymbol{R}''=\boldsymbol{R}} \frac{\partial^n}{\partial \bar{\boldsymbol{k}}''^n} e^{i\bar{\boldsymbol{k}}''\cdot(\boldsymbol{r}''-\boldsymbol{r}')}. \tag{B.7}
$$

Using the integration by parts, we observe

$$
\text{Eq. (B.6)} = \frac{\partial^n}{\partial \boldsymbol{R}'^n}(-1)^m \int \frac{d\bar{\boldsymbol{k}}'}{(2\pi)^3} e^{i\bar{\boldsymbol{k}}'\cdot(\boldsymbol{r}-\boldsymbol{r}'')} \frac{\partial^m}{\partial \bar{\boldsymbol{k}}'^m} \check{A}(\boldsymbol{R}', \bar{\boldsymbol{k}}', i\omega_n)\Bigg|_{\boldsymbol{R}'=\boldsymbol{R}} \tag{B.8}
$$

$$
\text{Eq. (B.7)} = \frac{\partial^m}{\partial \boldsymbol{R}''^m}(-1)^n \int \frac{d\bar{\boldsymbol{k}}''}{(2\pi)^3} e^{i\bar{\boldsymbol{k}}''\cdot(\boldsymbol{r}''-\boldsymbol{r}')} \frac{\partial^n}{\partial \bar{\boldsymbol{k}}''^n} \check{B}(\boldsymbol{R}'', \bar{\boldsymbol{k}}'', i\omega_n)\Bigg|_{\boldsymbol{R}''=\boldsymbol{R}}. \tag{B.9}
$$

Note that the terms proportional to $(\boldsymbol{R}'-\boldsymbol{R})^n$ and $(\boldsymbol{R}''-\boldsymbol{R})^m$ vanish in the integration by parts at $\boldsymbol{R}'=\boldsymbol{R}$ and $\boldsymbol{R}''=\boldsymbol{R}$, respectively. Hence, we obtain

$$
\check{C}(\boldsymbol{r}, \boldsymbol{r}', i\omega_n) = \int d\boldsymbol{r}'' \int \frac{d\bar{\boldsymbol{k}}'}{(2\pi)^3} \int \frac{d\bar{\boldsymbol{k}}''}{(2\pi)^3} e^{i\bar{\boldsymbol{k}}'\cdot(\boldsymbol{r}-\boldsymbol{r}'')} e^{i\bar{\boldsymbol{k}}''\cdot(\boldsymbol{r}''-\boldsymbol{r}')}
$$

$$
\times \sum_{n=0}^{\infty} \sum_{m=0}^{\infty} \frac{1}{n!}\frac{1}{m!} \left(\frac{-1}{2i}\right)^n \left(\frac{1}{2i}\right)^m \left.\frac{\partial^n \partial^m \check{A}(\boldsymbol{R}', \bar{\boldsymbol{k}}', i\omega_n)}{\partial \boldsymbol{R}'^n \partial \bar{\boldsymbol{k}}'^m}\right|_{\boldsymbol{R}'=\boldsymbol{R}} \cdot \left.\frac{\partial^m \partial^n \check{B}(\boldsymbol{R}'', \bar{\boldsymbol{k}}'', i\omega_n)}{\partial \boldsymbol{R}''^m \partial \bar{\boldsymbol{k}}''^n}\right|_{\boldsymbol{R}''=\boldsymbol{R}}
$$

$$
= \int \frac{d\bar{\boldsymbol{k}}'}{(2\pi)^3} \int \frac{d\bar{\boldsymbol{k}}''}{(2\pi)^3} (2\pi)^3 \delta(\bar{\boldsymbol{k}}''-\bar{\boldsymbol{k}}') e^{i\bar{\boldsymbol{k}}'\cdot\boldsymbol{r}} e^{i\bar{\boldsymbol{k}}''\cdot\boldsymbol{r}'}
$$

$$
\times \sum_{n=0}^{\infty} \sum_{m=0}^{\infty} \frac{1}{n!}\frac{1}{m!} \left(\frac{-1}{2i}\right)^n \left(\frac{1}{2i}\right)^m \left.\frac{\partial^n \partial^m \check{A}(\boldsymbol{R}', \bar{\boldsymbol{k}}', i\omega_n)}{\partial \boldsymbol{R}'^n \partial \bar{\boldsymbol{k}}'^m}\right|_{\boldsymbol{R}'=\boldsymbol{R}} \cdot \left.\frac{\partial^m \partial^n \check{B}(\boldsymbol{R}'', \bar{\boldsymbol{k}}'', i\omega_n)}{\partial \boldsymbol{R}''^m \partial \bar{\boldsymbol{k}}''^n}\right|_{\boldsymbol{R}''=\boldsymbol{R}}
$$

$$
= \int \frac{d\bar{\boldsymbol{k}}'}{(2\pi)^3} e^{i\bar{\boldsymbol{k}}'\cdot(\boldsymbol{r}-\boldsymbol{r}')}
$$

$$
\times \exp\left[\frac{i}{2}\left(\frac{\partial}{\partial \boldsymbol{R}'}\frac{\partial}{\partial \bar{\boldsymbol{k}}''} - \frac{\partial}{\partial \bar{\boldsymbol{k}}'}\frac{\partial}{\partial \boldsymbol{R}''}\right)\right] \check{A}(\boldsymbol{R}', \bar{\boldsymbol{k}}', i\omega_n)\check{B}(\boldsymbol{R}'', \bar{\boldsymbol{k}}'', i\omega_n)\Bigg|_{\boldsymbol{R}'=\boldsymbol{R}''=\boldsymbol{R}, \bar{\boldsymbol{k}}''=\bar{\boldsymbol{k}}'}. \tag{B.10}
$$

Therefore, the Wigner representation for $\check{C}(\boldsymbol{r}, \boldsymbol{r}', i\omega_n) = \check{C}(\boldsymbol{R} = (\boldsymbol{r} + \boldsymbol{r}')/2, \bar{\boldsymbol{r}} = \boldsymbol{r} - \boldsymbol{r}', i\omega_n)$ is obtained as

$$
\begin{aligned}
\check{C}(\boldsymbol{R}, \bar{\boldsymbol{k}}, i\omega_n) &= \int d\bar{\boldsymbol{r}} e^{-i\bar{\boldsymbol{k}}\cdot\bar{\boldsymbol{r}}} \check{C}(\boldsymbol{R}, \bar{\boldsymbol{r}}, i\omega_n) \\
&= \int d\bar{\boldsymbol{r}} e^{-i\bar{\boldsymbol{k}}\cdot\bar{\boldsymbol{r}}} \int \frac{d\bar{\boldsymbol{k}}'}{(2\pi)^3} e^{i\bar{\boldsymbol{k}}'\cdot(\boldsymbol{r}-\boldsymbol{r}')} \\
&\quad \times \exp\left[\frac{i}{2}\left(\frac{\partial}{\partial \boldsymbol{R}'}\frac{\partial}{\partial \bar{\boldsymbol{k}}''} - \frac{\partial}{\partial \bar{\boldsymbol{k}}'}\frac{\partial}{\partial \boldsymbol{R}''}\right)\right] \check{A}(\boldsymbol{R}', \bar{\boldsymbol{k}}', i\omega_n)\check{B}(\boldsymbol{R}'', \bar{\boldsymbol{k}}'', i\omega_n)\bigg|_{\boldsymbol{R}'=\boldsymbol{R}''=\boldsymbol{R}, \bar{\boldsymbol{k}}''=\bar{\boldsymbol{k}}'} \\
&= \int \frac{d\bar{\boldsymbol{k}}'}{(2\pi)^3}(2\pi)^3\delta(\bar{\boldsymbol{k}}' - \bar{\boldsymbol{k}}) \\
&\quad \times \exp\left[\frac{i}{2}\left(\frac{\partial}{\partial \boldsymbol{R}'}\frac{\partial}{\partial \bar{\boldsymbol{k}}''} - \frac{\partial}{\partial \bar{\boldsymbol{k}}'}\frac{\partial}{\partial \boldsymbol{R}''}\right)\right] \check{A}(\boldsymbol{R}', \bar{\boldsymbol{k}}', i\omega_n)\check{B}(\boldsymbol{R}'', \bar{\boldsymbol{k}}'', i\omega_n)\bigg|_{\boldsymbol{R}'=\boldsymbol{R}''=\boldsymbol{R}, \bar{\boldsymbol{k}}''=\bar{\boldsymbol{k}}'} \\
&= \exp\left[\frac{i}{2}\left(\frac{\partial}{\partial \boldsymbol{R}'}\frac{\partial}{\partial \bar{\boldsymbol{k}}''} - \frac{\partial}{\partial \bar{\boldsymbol{k}}'}\frac{\partial}{\partial \boldsymbol{R}''}\right)\right] \check{A}(\boldsymbol{R}', \bar{\boldsymbol{k}}', i\omega_n)\check{B}(\boldsymbol{R}'', \bar{\boldsymbol{k}}'', i\omega_n)\bigg|_{\boldsymbol{R}'=\boldsymbol{R}''=\boldsymbol{R}, \bar{\boldsymbol{k}}'=\bar{\boldsymbol{k}}''=\bar{\boldsymbol{k}}} \\
&\equiv \check{A}(\boldsymbol{R}, \bar{\boldsymbol{k}}, i\omega_n) \circ \check{B}(\boldsymbol{R}, \bar{\boldsymbol{k}}, i\omega_n). \quad\quad\quad (B.11)
\end{aligned}
$$

This product is called the circle product or Moyal product.

Appendix C

Matrix Riccati Equation for a Noncentrosymmetric Superconductor with Impurities

In this appendix, we describe briefly the derivation of the matrix Riccati equation including the Rashba-type spin-orbit coupling term and the impurity self-energy by means of the projection method [112, 10, 113]. We introduce the projecters:

$$\check{P}_{\pm} = \frac{1}{2}\left(\check{\tau}_0 \pm \frac{1}{-i\pi}\check{g}\right). \tag{C.1}$$

These projectors satisfy the relations:

$$\check{P}_{\pm} \cdot \check{P}_{\pm} = \check{P}_{\pm}, \tag{C.2}$$

$$\check{P}_{+} + \check{P}_{-} = \check{\tau}_0, \tag{C.3}$$

$$\check{P}_{+} \cdot \check{P}_{-} = \check{P}_{-} \cdot \check{P}_{+} = \check{0}. \tag{C.4}$$

We can confirm the following relation: $\check{P}_{+} - \check{P}_{-} = \check{g}/(-i\pi)$. Then, the quasiclassical Green's function is obtained as $\check{g} = -i\pi\left(\check{P}_{+} - \check{P}_{-}\right)$. Substituting this Green's function into Eq. (4.2), we have the equation for the projectors $\check{P}_{\pm}$:

$$-i\boldsymbol{v}_{\mathrm{F}} \cdot \boldsymbol{\nabla}\check{P}_{\pm} = \left[i\omega_n\check{\tau}_3 - \check{\Delta} - \check{\Sigma} - \alpha\check{\boldsymbol{g}}_k \cdot \check{S}, \check{P}_{\pm}\right]. \tag{C.5}$$

We define the projectors as

$$\check{P}_{+} = \begin{pmatrix} \hat{\sigma}_0 \\ -i\hat{b} \end{pmatrix}\left(\hat{\sigma}_0 + \hat{a}\hat{b}\right)^{-1}\begin{pmatrix} \hat{\sigma}_0 & i\hat{a} \end{pmatrix}, \tag{C.6}$$

$$\check{P}_{-} = \begin{pmatrix} -i\hat{a} \\ \hat{\sigma}_0 \end{pmatrix}\left(\hat{\sigma}_0 + \hat{b}\hat{a}\right)^{-1}\begin{pmatrix} i\hat{b} & \hat{\sigma}_0 \end{pmatrix}, \tag{C.7}$$

which satisfy Eq. (C.2) and (C.4). To satisfy Eq. (C.3), we need the following relations between $\hat{a}$ and $\hat{b}$: $(\hat{\sigma}_0 + \hat{a}\hat{b})^{-1}\hat{a} = \hat{a}(\hat{\sigma}_0 + \hat{b}\hat{a})^{-1}$, $\hat{b}(\hat{\sigma}_0 + \hat{a}\hat{b})^{-1} = (\hat{\sigma}_0 + \hat{b}\hat{a})^{-1}\hat{b}$. Using these relations, the quasiclassical Green's function is obtained as

$$\check{g} = -i\pi\begin{pmatrix} \left(\hat{\sigma}_0 + \hat{a}\hat{b}\right)^{-1}\left(\hat{\sigma}_0 - \hat{a}\hat{b}\right) & 2i\left(\hat{\sigma}_0 + \hat{a}\hat{b}\right)^{-1}\hat{a} \\ -2i\hat{b}\left(\hat{\sigma}_0 + \hat{a}\hat{b}\right)^{-1} & -\left(\hat{\sigma}_0 + \hat{b}\hat{a}\right)^{-1}\left(\hat{\sigma}_0 - \hat{b}\hat{a}\right) \end{pmatrix}. \tag{C.8}$$

Substituting Eq. (C.6) and (C.7) into Eq. (C.5) and calculating with respect to each component, we obtaine the matrix Riccati equations:

$$\boldsymbol{v}_{\mathrm{F}} \cdot \boldsymbol{\nabla}\hat{a}_0 + 2\omega_n\hat{a}_0 + \hat{a}_0\left(\hat{\Delta}_0^\dagger - \hat{\Sigma}_{21}^0\right)\hat{a}_0 - \left(\hat{\Delta}_0 + \hat{\Sigma}_{12}^0\right)$$
$$+ i\alpha\boldsymbol{g}_k \cdot (\hat{\boldsymbol{\sigma}}\hat{a}_0 - \hat{a}_0\hat{\boldsymbol{\sigma}}) + i\left(\hat{\Sigma}_{11}^0\hat{a}_0 + \hat{a}_0\hat{\Sigma}_{22}^0\right) = \hat{0}, \qquad (\mathrm{C.9})$$

$$\boldsymbol{v}_{\mathrm{F}} \cdot \boldsymbol{\nabla}\hat{b}_0 - 2\omega_n\hat{b}_0 - \hat{b}_0\left(\hat{\Delta}_0 + \hat{\Sigma}_{12}^0\right)\hat{b}_0 + \left(\hat{\Delta}_0^\dagger - \hat{\Sigma}_{21}^0\right)$$
$$+ i\alpha\boldsymbol{g}_k \cdot \left(\hat{b}_0\hat{\boldsymbol{\sigma}} - \hat{\boldsymbol{\sigma}}\hat{b}_0\right) - i\left(\hat{b}_0\hat{\Sigma}_{11}^0 + \hat{\Sigma}_{22}^0\hat{b}_0\right) = \hat{0}. \qquad (\mathrm{C.10})$$

Here, we define $\hat{a} = \hat{a}_0 i\hat{\sigma}_y, \hat{b} = -i\hat{\sigma}_y\hat{b}_0, \hat{\Sigma}_{11} = \hat{\Sigma}_{11}^0, \hat{\Sigma}_{12} = \hat{\Sigma}_{12}^0 i\hat{\sigma}_y, \hat{\Sigma}_{21} = -i\hat{\sigma}_y\hat{\Sigma}_{21}^0, \hat{\Sigma}_{22} = -\hat{\sigma}_y\hat{\Sigma}_{22}^0\hat{\sigma}_y, \hat{\Delta} = \hat{\Delta}_0 i\hat{\sigma}_y, \hat{\Delta}^\dagger = -i\hat{\sigma}_y\hat{\Delta}_0^\dagger$. The impurity self-energies in which $i\hat{\sigma}_y$ is factored out are defined by

$$\hat{\Sigma}_{11}^0 = -i\Gamma_{\mathrm{n}}\langle\hat{g}_0\rangle_{\tilde{\boldsymbol{k}}} = -i\Gamma_{\mathrm{n}}\left\langle\left(\hat{\sigma}_0 + \hat{a}_0\hat{b}_0\right)^{-1}\left(\hat{\sigma}_0 - \hat{a}_0\hat{b}_0\right)\right\rangle_{\tilde{\boldsymbol{k}}}, \qquad (\mathrm{C.11})$$

$$\hat{\Sigma}_{12}^0 = \Gamma_{\mathrm{n}}\langle\hat{f}_0\rangle_{\tilde{\boldsymbol{k}}} = \Gamma_{\mathrm{n}}\left\langle 2\left(\hat{\sigma}_0 + \hat{a}_0\hat{b}_0\right)^{-1}\hat{a}_0\right\rangle_{\tilde{\boldsymbol{k}}}, \qquad (\mathrm{C.12})$$

$$\hat{\Sigma}_{21}^0 = -\Gamma_{\mathrm{n}}\langle\hat{\tilde{f}}_0\rangle_{\tilde{\boldsymbol{k}}} = -\Gamma_{\mathrm{n}}\left\langle 2\hat{b}_0\left(\hat{\sigma}_0 + \hat{a}_0\hat{b}_0\right)^{-1}\right\rangle_{\tilde{\boldsymbol{k}}}, \qquad (\mathrm{C.13})$$

$$\hat{\Sigma}_{22}^0 = i\Gamma_{\mathrm{n}}\langle\hat{\tilde{g}}_0\rangle_{\tilde{\boldsymbol{k}}} = i\Gamma_{\mathrm{n}}\left\langle -\left(\hat{\sigma}_0 + \hat{b}_0\hat{a}_0\right)^{-1}\left(\hat{\sigma}_0 - \hat{b}_0\hat{a}_0\right)\right\rangle_{\tilde{\boldsymbol{k}}}. \qquad (\mathrm{C.14})$$

Here we used the definition $\hat{g} = \hat{g}_0, \hat{f} = \hat{f}_0 i\hat{\sigma}_y, \hat{\tilde{f}} = -i\hat{\sigma}_y\hat{\tilde{f}}_0, \hat{\tilde{g}} = -\hat{\sigma}_y\hat{\tilde{g}}_0\hat{\sigma}_y$.

Appendix D

Bulk Impurity Effect in Noncentrosymmetric Superconductors

D.1 Eilenberger equation

The quasiclassical Green's function is defined as

$$\check{g}(\boldsymbol{r}, \tilde{\boldsymbol{k}}, i\omega_n) = -i\pi \begin{pmatrix} \hat{g} & i\hat{f} \\ -i\hat{\bar{f}} & -\hat{\bar{g}} \end{pmatrix}. \tag{D.1}$$

The Eilenberger equation with the impurity self-energy is

$$i\boldsymbol{v}_{\mathrm{F}}(\tilde{\boldsymbol{k}}) \cdot \boldsymbol{\nabla} \check{g}(\boldsymbol{r}, \tilde{\boldsymbol{k}}, i\omega_n) + \left[i\omega_n \check{\tau}_3 - \check{\Delta} - \check{\Sigma} - \alpha \check{\boldsymbol{g}}_k \cdot \check{\boldsymbol{S}}, \ \check{g}(\boldsymbol{r}, \tilde{\boldsymbol{k}}, i\omega_n) \right] = \check{0}. \tag{D.2}$$

$\hat{\Sigma}$ is the impurity self-energy,

$$\check{\Sigma}(i\omega_n, \boldsymbol{r}, \tilde{\boldsymbol{k}}) = \begin{pmatrix} \Sigma_{11} & \Sigma_{12} \\ \Sigma_{21} & \Sigma_{22} \end{pmatrix}. \tag{D.3}$$

Calculating the Eilenberger equation with respect to each component in Nambu space, we obtain

$$\partial \hat{g}_0 + i\alpha \boldsymbol{g}_k \cdot (\hat{\boldsymbol{\sigma}} \hat{g}_0 - \hat{g}_0 \hat{\boldsymbol{\sigma}}) + i\hat{\Sigma}_{11}^0 \hat{g}_0 - i\hat{g}_0 \hat{\Sigma}_{11}^0 + (\hat{\Delta}_0 + \hat{\Sigma}_{12}^0)\hat{\bar{f}}_0 - \hat{f}_0(\hat{\Delta}_0^\dagger - \hat{\Sigma}_{21}^0) = \hat{0}, \tag{D.4}$$

$$\partial \hat{f}_0 + 2\omega_n \hat{f}_0 + i\alpha \boldsymbol{g}_k \cdot (\hat{\boldsymbol{\sigma}} \hat{f}_0 - \hat{f}_0 \hat{\boldsymbol{\sigma}}) + i\hat{\Sigma}_{11}^0 \hat{f}_0 + i\hat{f}_0 \hat{\Sigma}_{22}^0 + (\hat{\Delta}_0 + \hat{\Sigma}_{12}^0)\hat{\bar{g}}_0 - \hat{g}_0(\hat{\Delta}_0 + \hat{\Sigma}_{12}^0) = \hat{0}, \tag{D.5}$$

$$\partial \hat{\bar{f}}_0 - 2\omega_n \hat{\bar{f}}_0 + i\alpha \boldsymbol{g}_k \cdot (\hat{\boldsymbol{\sigma}} \hat{\bar{f}}_0 - \hat{\bar{f}}_0 \hat{\boldsymbol{\sigma}}) - i\hat{\Sigma}_{22}^0 \hat{\bar{f}}_0 - i\hat{\bar{f}}_0 \hat{\Sigma}_{11}^0 + (\hat{\Delta}_0^\dagger - \hat{\Sigma}_{21}^0)\hat{g}_0 - \hat{\bar{g}}_0(\hat{\Delta}_0^\dagger - \hat{\Sigma}_{21}^0) = \hat{0}, \tag{D.6}$$

$$\partial \hat{\bar{g}}_0 + i\alpha \boldsymbol{g}_k \cdot (\hat{\boldsymbol{\sigma}} \hat{\bar{g}}_0 - \hat{\bar{g}}_0 \hat{\boldsymbol{\sigma}}) - i\hat{\Sigma}_{22}^0 \hat{\bar{g}}_0 + i\hat{\bar{g}}_0 \hat{\Sigma}_{22}^0 + (\hat{\Delta}_0^\dagger - \hat{\Sigma}_{21}^0)\hat{f}_0 - \hat{\bar{f}}_0(\hat{\Delta}_0 + \hat{\Sigma}_{12}^0) = \hat{0}, \tag{D.7}$$

where we have defined $\partial = \boldsymbol{v}_{\mathrm{F}} \cdot \boldsymbol{\nabla}$ and

$$\hat{g} = \hat{g}_0, \quad \hat{f} = \hat{f}_0 i\hat{\sigma}_y, \quad \hat{\bar{f}} = -i\hat{\sigma}_y \hat{\bar{f}}_0, \quad \hat{\bar{g}} = -\hat{\sigma}_y \hat{\bar{g}}_0 \hat{\sigma}_y, \tag{D.8}$$

$$\hat{\Sigma}_{11} = \hat{\Sigma}_{11}^0, \quad \hat{\Sigma}_{12} = \hat{\Sigma}_{12}^0 i\hat{\sigma}_y, \quad \hat{\Sigma}_{21} = -i\hat{\sigma}_y \hat{\Sigma}_{21}^0, \quad \hat{\Sigma}_{22} = -\hat{\sigma}_y \hat{\Sigma}_{22}^0 \hat{\sigma}_y, \tag{D.9}$$

$$\hat{\Delta} = \hat{\Delta}_0 i\hat{\sigma}_y, \quad \hat{\Delta}^\dagger = -i\hat{\sigma}_y \hat{\Delta}_0^\dagger. \tag{D.10}$$

D.2 Impurity self-energy in the Born limit

In this appendix, we describe the non-magnetic impurity scattering in the bulk. We assume the s-wave scattering in the Born limit. The impurity self-energy is given by

$$\check{\Sigma}(\boldsymbol{r}, i\omega_n) = \frac{\Gamma_n}{\pi} \left\langle \check{g}(\boldsymbol{r}, \tilde{\boldsymbol{k}}, i\omega_n) \right\rangle_{\tilde{\boldsymbol{k}}} \tag{D.11}$$

$$= \Gamma_n \begin{pmatrix} -i\langle \hat{g}(\boldsymbol{r}, \tilde{\boldsymbol{k}}, i\omega_n)\rangle_{\tilde{\boldsymbol{k}}} & \langle \hat{f}(\boldsymbol{r}, \tilde{\boldsymbol{k}}, i\omega_n)\rangle_{\tilde{\boldsymbol{k}}} \\ -\langle \hat{\bar{f}}(\boldsymbol{r}, \tilde{\boldsymbol{k}}, i\omega_n)\rangle_{\tilde{\boldsymbol{k}}} & i\langle \hat{\bar{g}}(\boldsymbol{r}, \tilde{\boldsymbol{k}}, i\omega_n)\rangle_{\tilde{\boldsymbol{k}}} \end{pmatrix} \tag{D.12}$$

where the brackets $\langle \cdots \rangle_{\tilde{\boldsymbol{k}}}$ indicate average over the Fermi surface and $\Gamma_n = \pi n_{\mathrm{imp}} N_F v^2$ is the impurity scattering rate in the normal state. n_{imp} is the density of impurities, $N_F [= (N_I + N_{II})/2]$ is the density of states at the Fermi level in the normal state, v is the impurity potential for s-wave scattering.

At least in spatially uniform systems or in spatially inhomogeneous systems in the clean limit (e.g., clean vortex states), we can separate the Green's functions with respect to each band split due to the spin-orbit coupling using the band basis (see the appendix of Ref. [29] and see also Refs. [30, 28]). Then transforming to the orbital basis the Green's functions are expressed as [29, 28]

$$\hat{g} = g_I \hat{\sigma}_I + g_{II} \hat{\sigma}_{II}, \quad \hat{f} = (f_I \hat{\sigma}_I + f_{II} \hat{\sigma}_{II}) i\hat{\sigma}_y, \tag{D.13}$$

$$\hat{\bar{f}} = -i\hat{\sigma}_y \left(\bar{f}_I \hat{\sigma}_I + \bar{f}_{II} \hat{\sigma}_{II} \right), \quad \hat{\bar{g}} = -\hat{\sigma}_y \left(\bar{g}_I \hat{\sigma}_I + \bar{g}_{II} \hat{\sigma}_{II} \right) i\hat{\sigma}_y, \tag{D.14}$$

with $\hat{\sigma}_{I,II} = \left(\hat{\sigma}_0 \pm \bar{\boldsymbol{g}}_k \cdot \hat{\boldsymbol{\sigma}} \right)/2$ and $\bar{\boldsymbol{g}}_k = \boldsymbol{g}_k/|\boldsymbol{g}_k|$. Provided the Green's functions are invariant under $\boldsymbol{k} \to -\boldsymbol{k}$ [37], then

$$\langle \hat{g} \rangle_{\tilde{\boldsymbol{k}}} = \frac{1}{2}\langle g_I + g_{II}\rangle_{\tilde{\boldsymbol{k}}}\hat{\sigma}_0, \quad \langle \hat{f} \rangle_{\tilde{\boldsymbol{k}}} = \frac{1}{2}\langle f_I + f_{II}\rangle_{\tilde{\boldsymbol{k}}}\hat{\sigma}_0 i\hat{\sigma}_y, \tag{D.15}$$

$$\langle \hat{\bar{f}} \rangle_{\tilde{\boldsymbol{k}}} = -i\hat{\sigma}_y \frac{1}{2}\langle \bar{f}_I + \bar{f}_{II}\rangle_{\tilde{\boldsymbol{k}}}\hat{\sigma}_0, \quad \langle \hat{\bar{g}} \rangle_{\tilde{\boldsymbol{k}}} = -\hat{\sigma}_y \frac{1}{2}\langle \bar{g}_I + \bar{g}_{II}\rangle_{\tilde{\boldsymbol{k}}}\hat{\sigma}_0\hat{\sigma}_y, \tag{D.16}$$

because $\bar{\boldsymbol{g}}_{-k} = -\bar{\boldsymbol{g}}_k$. Thus,

$$\langle \hat{g}_0 \rangle_{\tilde{\boldsymbol{k}}} = \frac{1}{2}\langle g_I + g_{II}\rangle_{\tilde{\boldsymbol{k}}}\hat{\sigma}_0, \quad \langle \hat{f}_0 \rangle_{\tilde{\boldsymbol{k}}} = \frac{1}{2}\langle f_I + f_{II}\rangle_{\tilde{\boldsymbol{k}}}\hat{\sigma}_0, \tag{D.17}$$

$$\langle \hat{\bar{f}}_0 \rangle_{\tilde{\boldsymbol{k}}} = \frac{1}{2}\langle \bar{f}_I + \bar{f}_{II}\rangle_{\tilde{\boldsymbol{k}}}\hat{\sigma}_0, \quad \langle \hat{\bar{g}}_0 \rangle_{\tilde{\boldsymbol{k}}} = \frac{1}{2}\langle \bar{g}_I + \bar{g}_{II}\rangle_{\tilde{\boldsymbol{k}}}\hat{\sigma}_0. \tag{D.18}$$

Therefore,

$$\hat{\Sigma}_{11}^0 = -i\Gamma_n\langle \hat{g}_0 \rangle_{\tilde{\boldsymbol{k}}} = -i\Gamma_n\frac{1}{2}\langle g_I + g_{II}\rangle_{\tilde{\boldsymbol{k}}}\hat{\sigma}_0, \quad \hat{\Sigma}_{12}^0 = \Gamma_n\langle \hat{f}_0 \rangle_{\tilde{\boldsymbol{k}}} = \Gamma_n\frac{1}{2}\langle f_I + f_{II}\rangle_{\tilde{\boldsymbol{k}}}\hat{\sigma}_0, \tag{D.19}$$

$$\hat{\Sigma}_{21}^0 = -\Gamma_n\langle \hat{\bar{f}}_0 \rangle_{\tilde{\boldsymbol{k}}} = -\Gamma_n\frac{1}{2}\langle \bar{f}_I + \bar{f}_{II}\rangle_{\tilde{\boldsymbol{k}}}\hat{\sigma}_0, \quad \hat{\Sigma}_{22}^0 = i\Gamma_n\langle \hat{\bar{g}}_0 \rangle_{\tilde{\boldsymbol{k}}} = i\Gamma_n\frac{1}{2}\langle \bar{g}_I + \bar{g}_{II}\rangle_{\tilde{\boldsymbol{k}}}\hat{\sigma}_0. \tag{D.20}$$

We notice that the impurity self-energies are proportional to the unit matrix $\hat{\sigma}_0$ in the bulk. In the bulk uniform system, the spatial derivative term in the Eilenberger equation (D.7) is neglected. Using the obtained impurity self-energy (D.20), we have

$$i\hat{\Sigma}_{11}^0\hat{g}_0 - i\hat{g}_0\hat{\Sigma}_{11}^0 = \hat{0}, \tag{D.21}$$

$$2\omega_n\hat{f}_0 + i\hat{\Sigma}_{11}^0\hat{f}_0 + i\hat{f}_0\hat{\Sigma}_{22}^0 = \begin{pmatrix} 2(\omega_n + \sigma_g) & 0 \\ 0 & 2(\omega_n + \sigma_g) \end{pmatrix}\hat{f}_0, \tag{D.22}$$

$$-2\omega_n\hat{\bar{f}}_0 - i\hat{\Sigma}_{22}^0\hat{\bar{f}}_0 - i\hat{\bar{f}}_0\hat{\Sigma}_{11}^0 = -\begin{pmatrix} 2(\omega_n + \sigma_g) & 0 \\ 0 & 2(\omega_n + \sigma_g) \end{pmatrix}\hat{\bar{f}}_0, \tag{D.23}$$

$$-i\hat{\Sigma}_{22}^0\hat{\bar{g}}_0 + i\hat{\bar{g}}_0\hat{\Sigma}_{22}^0 = \hat{0}, \tag{D.24}$$

where

$$\sigma_g \equiv \frac{\Gamma_{\rm n}}{2}(1+\delta)\frac{1}{2}\langle(g_{\rm I}-\bar{g}_{\rm I})\rangle_{\tilde{\boldsymbol{k}}} + \frac{\Gamma_{\rm n}}{2}(1-\delta)\frac{1}{2}\langle(g_{\rm II}-\bar{g}_{\rm II})\rangle_{\tilde{\boldsymbol{k}}}. \tag{D.25}$$

A parameter $\delta = (N_{\rm I} - N_{\rm II})/2N_{\rm F}$ $(-1 < \delta < 1)$ characterizes the the difference in the density of states. The rotation in spin space, which is represented by the unitary matrix $\hat{U}_k$, yields

$$\hat{U}_k^\dagger i\alpha\boldsymbol{g}_k \cdot (\hat{\boldsymbol{\sigma}}\hat{A}_0 - \hat{A}_0\hat{\boldsymbol{\sigma}})\hat{U}_k = i\alpha' \begin{pmatrix} 0 & -2\sin\theta_k A_b \\ 2\sin\theta_k A_c & 0 \end{pmatrix}, \tag{D.26}$$

$$\hat{U}_k^\dagger(\hat{\Delta}_0 + \hat{\Sigma}_{12}^0)\hat{U}_k = \begin{pmatrix} \Delta_{\rm II} + \sigma_f & 0 \\ 0 & \Delta_{\rm I} + \sigma_f \end{pmatrix}, \tag{D.27}$$

$$\hat{U}_k^\dagger(\hat{\Delta}_0^{\,\dagger} - \hat{\Sigma}_{21}^0)\hat{U}_k = \begin{pmatrix} \Delta_{\rm II}^* + \bar{\sigma}_f & 0 \\ 0 & \Delta_{\rm I}^* + \bar{\sigma}_f \end{pmatrix}, \tag{D.28}$$

where

$$\hat{U}_k^\dagger\hat{A}_0\hat{U}_k \equiv \begin{pmatrix} A_a & A_b \\ A_c & A_d \end{pmatrix}, \quad \alpha' \equiv \sqrt{3/2}\alpha, \quad \Delta_{\rm I,II} \equiv \Delta_{\rm s} \pm d_{\rm t}|\boldsymbol{g}_k|, \tag{D.29}$$

$$\sigma_f \equiv \Gamma_{\rm n}(1+\delta)\frac{1}{2}\langle f_{\rm I}\rangle_{\tilde{\boldsymbol{k}}} + \Gamma_{\rm n}(1-\delta)\frac{1}{2}\langle f_{\rm II}\rangle, \quad \bar{\sigma}_f \equiv \Gamma_{\rm n}(1+\delta)\frac{1}{2}\langle\bar{f}_{\rm I}\rangle_{\tilde{\boldsymbol{k}}} + \Gamma_{\rm n}(1-\delta)\frac{1}{2}\langle\bar{f}_{\rm II}\rangle. \tag{D.30}$$

Hence, the impurity effect in the bulk appears only in the replacement of the Matsubara frequency and the order parameter.

$$\omega_n \to \omega_n + \sigma_g, \quad \Delta_{\rm I,II} \to \Delta_{\rm I,II} + \sigma_f, \quad \Delta_{\rm I,II}^* \to \Delta_{\rm I,II} + \bar{\sigma}_f. \tag{D.31}$$

D.3   Gap equation

In the same way as Ref. [29], the Eilenberger equations in the band basis in the presence of impurities are obtained for the suffix a,

$$(\Delta_{\rm II} + \sigma_f)\bar{f}_a - (\Delta_{\rm II}^* + \bar{\sigma}_f)f_a = 0, \tag{D.32}$$
$$2(\omega_n + \sigma_g)f_a + (\Delta_{\rm II} + \sigma_f)\bar{g}_a - (\Delta_{\rm II} + \sigma_f)g_a = 0, \tag{D.33}$$
$$-2(\omega_n + \sigma_g)\bar{f}_a + (\Delta_{\rm II}^* + \bar{\sigma}_f)g_a - (\Delta_{\rm II}^* + \bar{\sigma}_f)\bar{g}_a = 0, \tag{D.34}$$
$$(\Delta_{\rm II}^* + \bar{\sigma}_f)f_a - (\Delta_{\rm II} + \sigma_f)\bar{f}_a = 0. \tag{D.35}$$

For b,

$$-2i\alpha'\sin\theta_k g_b + (\Delta_{\rm II} + \sigma_f)\bar{f}_b - (\Delta_{\rm I}^* + \bar{\sigma}_f)f_b = 0, \tag{D.36}$$
$$2(\omega_n + \sigma_g)f_b - 2i\alpha'\sin\theta_k f_b + (\Delta_{\rm II} + \sigma_f)\bar{g}_b - (\Delta_{\rm I} + \sigma_f)g_b = 0, \tag{D.37}$$
$$-2(\omega_n + \sigma_g)\bar{f}_b - 2i\alpha'\sin\theta_k\bar{f}_b + (\Delta_{\rm II}^* + \bar{\sigma}_f)g_b - (\Delta_{\rm I}^* + \bar{\sigma}_f)\bar{g}_b = 0, \tag{D.38}$$
$$-2i\alpha'\sin\theta_k\bar{g}_b + (\Delta_{\rm II}^* + \bar{\sigma}_f)f_b - (\Delta_{\rm I} + \sigma_f)\bar{f}_b = 0. \tag{D.39}$$

For c,

$$2i\alpha'\sin\theta_k g_c + (\Delta_{\rm I} + \sigma_f)\bar{f}_c - (\Delta_{\rm II}^* + \bar{\sigma}_f)f_c = 0, \tag{D.40}$$
$$2(\omega_n + \sigma_g)f_c + 2i\alpha'\sin\theta_k f_c + (\Delta_{\rm I} + \sigma_f)\bar{g}_c - (\Delta_{\rm II} + \sigma_f)g_c = 0, \tag{D.41}$$
$$-2(\omega_n + \sigma_g)\bar{f}_c + 2i\alpha'\sin\theta_k\bar{f}_c + (\Delta_{\rm I}^* + \bar{\sigma}_f)g_c - (\Delta_{\rm II}^* + \bar{\sigma}_f)\bar{g}_c = 0, \tag{D.42}$$
$$2i\alpha'\sin\theta_k\bar{g}_c + (\Delta_{\rm I}^* + \bar{\sigma}_f)f_c - (\Delta_{\rm II} + \sigma_f)\bar{f}_c = 0. \tag{D.43}$$

For d,

$$(\Delta_{\rm I} + \sigma_f)\bar{f}_d - (\Delta_{\rm I}^* + \bar{\sigma}_f)f_d = 0, \tag{D.44}$$
$$2(\omega_n + \sigma_g)f_d + (\Delta_{\rm I} + \sigma_f)\bar{g}_d - (\Delta_{\rm I} + \sigma_f)g_d = 0, \tag{D.45}$$
$$-2(\omega_n + \sigma_g)\bar{f}_d + (\Delta_{\rm I}^* + \bar{\sigma}_f)g_d - (\Delta_{\rm I}^* + \bar{\sigma}_f)\bar{g}_d = 0, \tag{D.46}$$
$$(\Delta_{\rm I}^* + \bar{\sigma}_f)f_d - (\Delta_{\rm I} + \sigma_f)\bar{f}_d = 0. \tag{D.47}$$

With use of the same consideration as the appendix in Ref. [29], we can obtaine the following Green's functions in spatially uniform systems,

$$g_{\mathrm{I,II}}(i\omega_n, \tilde{\boldsymbol{k}}) = \frac{\omega_n + \sigma_g(i\omega_n)}{B_{\mathrm{I,II}}(i\omega_n, \tilde{\boldsymbol{k}})}, \quad f_{\mathrm{I,II}}(i\omega_n, \tilde{\boldsymbol{k}}) = \frac{\Delta_{\mathrm{I,II}}(\tilde{\boldsymbol{k}}) + \sigma_f(i\omega_n)}{B_{\mathrm{I,II}}(i\omega_n, \tilde{\boldsymbol{k}})}, \tag{D.48}$$

$$\bar{f}_{\mathrm{I,II}}(i\omega_n, \tilde{\boldsymbol{k}}) = \frac{\Delta_{\mathrm{I,II}}^*(\tilde{\boldsymbol{k}}) + \bar{\sigma}_f(i\omega_n)}{B_{\mathrm{I,II}}(i\omega_n, \tilde{\boldsymbol{k}})}, \quad \bar{g}_{\mathrm{I,II}}(i\omega_n, \tilde{\boldsymbol{k}}) = \frac{-\omega_n - \sigma_g(i\omega_n)}{B_{\mathrm{I,II}}(i\omega_n, \tilde{\boldsymbol{k}})}, \tag{D.49}$$

with $B_{\mathrm{I,II}}(i\omega_n, \tilde{\boldsymbol{k}}) = \sqrt{(\omega_n + \sigma_g(i\omega_n))^2 + |\Delta_{\mathrm{I,II}}(\tilde{\boldsymbol{k}}) + \sigma_f(i\omega_n)|^2}$. The gap equations are

$$\Delta_{\mathrm{s}} = \pi T \sum_{|\omega_n| < \omega_{\mathrm{c}}} \left[\lambda_{\mathrm{s}} \left\{ \langle f_+ \rangle_{\tilde{\boldsymbol{k}}} + \delta \langle f_- \rangle_{\tilde{\boldsymbol{k}}} \right\} + \lambda_{\mathrm{m}} \left\{ \langle |\boldsymbol{g}_k| f_- \rangle_{\tilde{\boldsymbol{k}}} + \delta \langle |\boldsymbol{g}_k| f_+ \rangle_{\tilde{\boldsymbol{k}}} \right\} \right], \tag{D.50}$$

$$d_{\mathrm{t}} = \pi T \sum_{|\omega_n| < \omega_{\mathrm{c}}} \left[\lambda_{\mathrm{t}} \left\{ \langle |\boldsymbol{g}_k| f_- \rangle_{\tilde{\boldsymbol{k}}} + \delta \langle |\boldsymbol{g}_k| f_+ \rangle_{\tilde{\boldsymbol{k}}} \right\} + \lambda_{\mathrm{m}} \left\{ \langle f_+ \rangle_{\tilde{\boldsymbol{k}}} + \delta \langle f_- \rangle_{\tilde{\boldsymbol{k}}} \right\} \right], \tag{D.51}$$

where we have defined $\lambda_{\mathrm{s}} = -e_{\mathrm{s}} N_{\mathrm{F}} V$, $\lambda_{\mathrm{t}} = -e_{\mathrm{t}} N_{\mathrm{F}} V$ and $\lambda_{\mathrm{m}} = e_{\mathrm{m}} N_{\mathrm{F}} V$ (see Appendix F). $f_{\pm} \equiv (f_{\mathrm{I}} \pm f_{\mathrm{II}})/2$ and ω_{c} is the cut-off frequency. The parameters in the gap equations are defined in the clean limit as follows [29].

$$\nu = \left. \frac{\psi_{\mathrm{s}}}{d_{\mathrm{t}}} \right|_{T \to T_{\mathrm{c0}} - 0^+}, \tag{D.52}$$

$$w = \ln \left(\frac{T}{T_{\mathrm{c0}}} \right) + \sum_{0 \leq n < n_{\mathrm{c}}(T)} \frac{2}{2n+1}, \tag{D.53}$$

$$n_{\mathrm{c}}(T) = \frac{1}{2} \left(\frac{\omega_{\mathrm{c}}}{\pi T} - 1 \right), \tag{D.54}$$

$$\lambda_{\mathrm{s}} = \frac{1}{\nu + \delta \langle |\boldsymbol{g}_k| \rangle_{\tilde{\boldsymbol{k}}}} \left[\frac{\nu}{w} - \lambda_{\mathrm{m}} \left(1 + \delta \nu \langle |\boldsymbol{g}_k| \rangle_{\tilde{\boldsymbol{k}}} \right) \right], \tag{D.55}$$

$$\lambda_{\mathrm{t}} = \frac{1}{1 + \delta \nu \langle |\boldsymbol{g}_k| \rangle_{\tilde{\boldsymbol{k}}}} \left[\frac{1}{w} - \lambda_{\mathrm{m}} \left(\nu + \delta \langle |\boldsymbol{g}_k| \rangle_{\tilde{\boldsymbol{k}}} \right) \right]. \tag{D.56}$$

Appendix E

Impurity Self Energies around a Vortex Core in Noncentrosymmetric Superconductors: $s + p$-wave case

In this appendix, we show the normal and the anomalous self-energies in the bare Born approximation for $s + p$-wave pair.
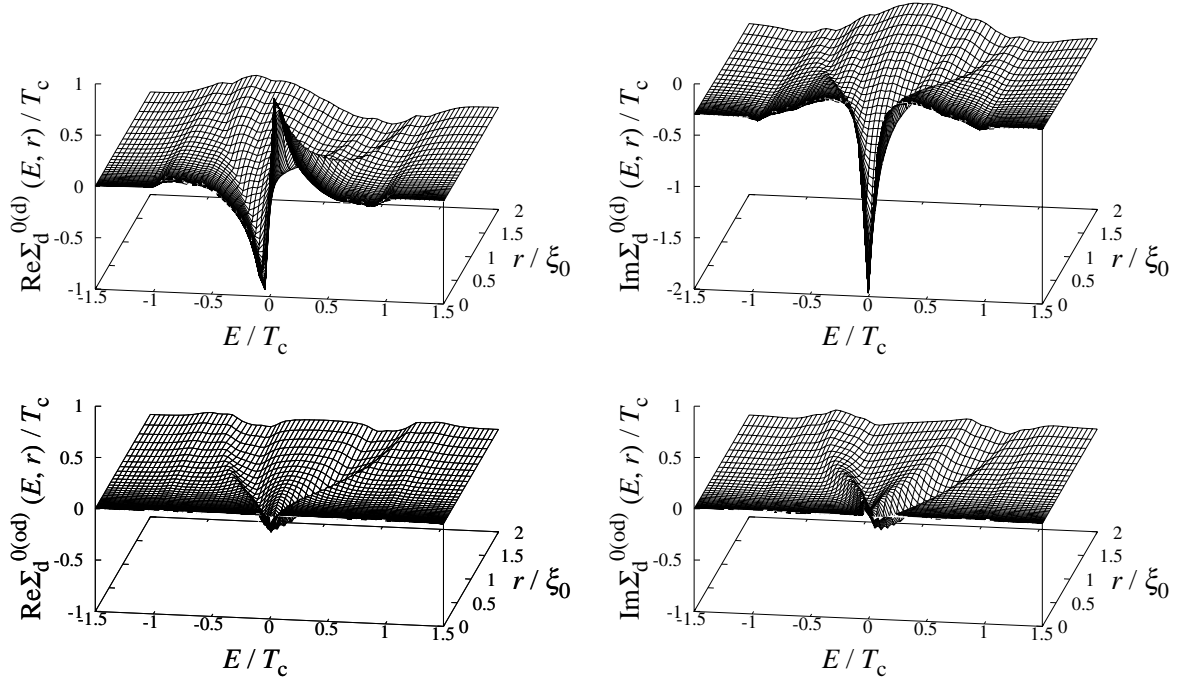

Figure E.1: The normal self energies around a vortex core for $s + p$-wave case ($\Psi/T_c : \Delta/T_c = 0.2 : 0.8$). The impurity scattering rate is set to $\Gamma_n/T_c = 0.3$. Other parameters are $\alpha'/T_c = 1$, $\eta/T_c = 0.05$. The index (d) and (od) mean the diagonal and off-diagonal components in spin space, respectively.
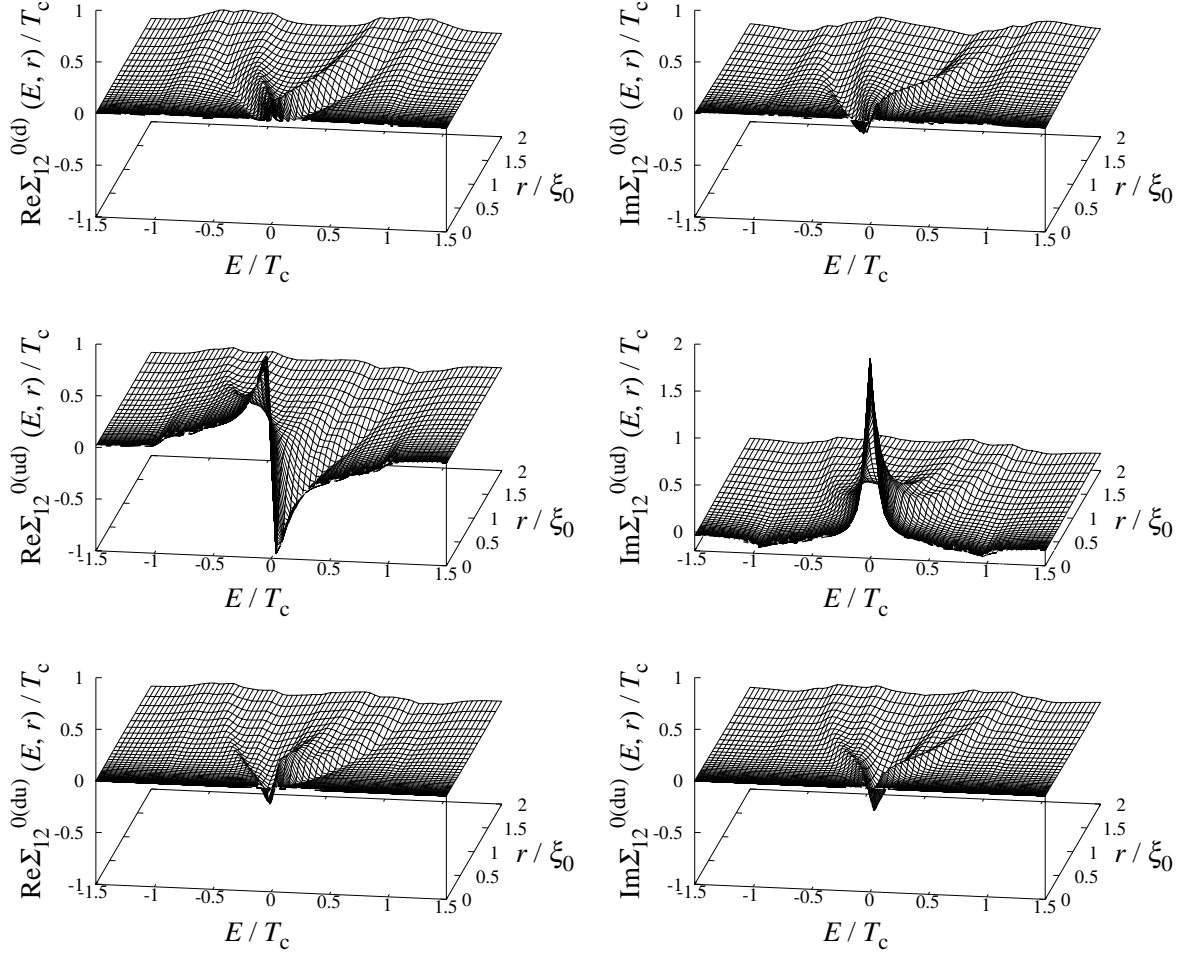
Figure E.2: The anomalous self energies around a vortex core for $s + p$-wave case ($\Psi/T_\mathrm{c} : \Delta/T_\mathrm{c} = 0.2 : 0.8$). The impurity scattering rate is set to $\varGamma_\mathrm{n}/T_\mathrm{c} = 0.3$. Other parameters are $\alpha'/T_\mathrm{c} = 1$, $\eta/T_\mathrm{c} = 0.05$. The index (d), (ud) and (du) mean the diagonal, $\uparrow\downarrow$ and $\downarrow\uparrow$ components in spin space, respectively.

Appendix F

Gap Equation for Inhomogeneous Situation in Noncentrosymmetric Superconductors

F.1 The general gap equation with spin degree of freedom

According to Sigrist and Ueda [1], the gap equation is defined by

$$\Delta_{s_1 s_2}(\boldsymbol{k}, \boldsymbol{q}) = - \sum_{\boldsymbol{k}', s_1', s_2'} V_{s_1 s_2 s_2' s_1'}(\boldsymbol{k}, \boldsymbol{k}') \left\langle a_{\boldsymbol{q}/2 + \boldsymbol{k}', s_1'} a_{\boldsymbol{q}/2 - \boldsymbol{k}', s_2'} \right\rangle, \tag{F.1}$$

where the relative momentum $\boldsymbol{k} = \boldsymbol{k}_2 - \boldsymbol{k}_1$ and the center of mass momentum $\boldsymbol{q} = (\boldsymbol{k}_1 + \boldsymbol{k}_2)/2$. The anomalous Green's function is given by

$$F_{s_1' s_2'}(\boldsymbol{k}, \boldsymbol{k}'; \tau) = \frac{1}{\beta} \sum_n F_{s_1' s_2'}(\boldsymbol{k}, \boldsymbol{k}'; i\omega_n) e^{-i\omega_n \tau}$$

$$= \langle T_\tau [a_{\boldsymbol{k}s}(\tau) a_{\boldsymbol{k}'s'}(0)] \rangle . \tag{F.2}$$

Here $\beta = T^{-1}$. We use a unit system in which $\hbar = k_{\mathrm{B}} = 1$. Then,

$$\left\langle a_{\boldsymbol{q}/2 + \boldsymbol{k}', s_1'} a_{\boldsymbol{q}/2 - \boldsymbol{k}', s_2'} \right\rangle = F_{s_1' s_2'}\left(\frac{\boldsymbol{q}}{2} + \boldsymbol{k}', \frac{\boldsymbol{q}}{2} - \boldsymbol{k}'; \tau \to 0^+\right). \tag{F.3}$$

Therefore,

$$\Delta_{s_1 s_2}(\boldsymbol{k}, \boldsymbol{q}) = - \sum_{\boldsymbol{k}', s_1', s_2'} V_{s_1 s_2 s_2' s_1'}(\boldsymbol{k}, \boldsymbol{k}') F_{s_1', s_2'}\left(\frac{\boldsymbol{q}}{2} + \boldsymbol{k}', \frac{\boldsymbol{q}}{2} - \boldsymbol{k}'; \tau \to 0^+\right)$$

$$= -\frac{1}{\beta} \sum_n \sum_{\boldsymbol{k}'} \sum_{s_1', s_2'} V_{s_1 s_2 s_2' s_1'}(\boldsymbol{k}, \boldsymbol{k}') F_{s_1' s_2'}\left(\frac{\boldsymbol{q}}{2} + \boldsymbol{k}', \frac{\boldsymbol{q}}{2} - \boldsymbol{k}'; i\omega_n\right) e^{-i\omega_n 0^+} \tag{F.4}$$

Performing the Fourier transformation with respect to the center of mass momentum $\boldsymbol{q}$,

$$\Delta_{s_1 s_2}(\boldsymbol{k}, \boldsymbol{R}) = \int \frac{d\boldsymbol{q}}{(2\pi)^3} e^{i\boldsymbol{q}\cdot\boldsymbol{R}} \Delta_{s_1 s_2}(\boldsymbol{k}, \boldsymbol{q})$$

$$= -\frac{1}{\beta} \sum_n \sum_{\boldsymbol{k}'} \sum_{s_1' s_2'} V_{s_1 s_2 s_2' s_1'}(\boldsymbol{k}, \boldsymbol{k}') \int \frac{d\boldsymbol{q}}{(2\pi)^3} e^{i\boldsymbol{q}\cdot\boldsymbol{R}} F_{s_1' s_2'}\left(\frac{\boldsymbol{q}}{2} + \boldsymbol{k}', \frac{\boldsymbol{q}}{2} - \boldsymbol{k}'; i\omega_n\right). \tag{F.5}$$

Here,

$$\sum_{\boldsymbol{k}'} \to \int \frac{d\boldsymbol{k}'}{(2\pi)^3}$$

$$= \int \frac{k'^2 dk'}{2\pi^2} \int \frac{d\boldsymbol{\Omega}_{k'}}{4\pi}. \tag{F.6}$$

We assume spherical Fermi surface.

$$\int \frac{d\boldsymbol{q}}{(2\pi)^3} e^{i\boldsymbol{q}\cdot\boldsymbol{R}} F_{s_1' s_2'}\left(\frac{\boldsymbol{q}}{2}+\boldsymbol{k}', \frac{\boldsymbol{q}}{2}-\boldsymbol{k}'; i\omega_n\right) = F_{s_1 s_2}(\boldsymbol{k}', \boldsymbol{R}; i\omega_n) \tag{F.7}$$

Then, the gap equation becomes

$$\Delta_{s_1 s_2}(\boldsymbol{k}, \boldsymbol{R}) = -T \sum_n \int \frac{k'^2 dk'}{2\pi^2} \int \frac{d\boldsymbol{\Omega}_{k'}}{4\pi} \sum_{s_1' s_2'} V_{s_1 s_2 s_2' s_1'}(\boldsymbol{k}, \boldsymbol{k}') F_{s_1' s_2'}(\boldsymbol{k}', \boldsymbol{R}; i\omega_n) \tag{F.8}$$

We perform the quasiclassical approximation, namely we put $k' = |\boldsymbol{k}'| \to k_{\mathrm{F}}'$:

$$\int \frac{k'^2 dk'}{2\pi^2} \int \frac{d\boldsymbol{\Omega}_{k'}}{4\pi} \to \int \frac{k_{\mathrm{F}}'(mv_{\mathrm{F}}')dk'}{2\pi^2} \int \frac{d\boldsymbol{\Omega}_{k'}}{4\pi}$$

$$= \frac{mk_{\mathrm{F}}'}{2\pi^2} \int v_{\mathrm{F}}' dk' \int \frac{d\boldsymbol{\Omega}_{k'}}{4\pi}$$

$$= N_{\mathrm{F}} \int \int \frac{d\boldsymbol{\Omega}_{k'}}{4\pi} \int d\xi_{k'}. \tag{F.9}$$

We define the quasiclassical anomalous Green's function following Schopohl [88],

$$f_{s_1' s_2'}(\hat{k}', \boldsymbol{R}; i\omega_n) \equiv \frac{1}{\pi} \int_{-\infty}^{+\infty} d\xi_{k'} F_{s_1' s_2'}(\boldsymbol{k}', \boldsymbol{R}; i\omega_n). \tag{F.10}$$

Hence,

$$\Delta_{s_1 s_2}(\hat{\boldsymbol{k}}, \boldsymbol{R}) = -\pi T N_{\mathrm{F}} \sum_n \sum_{s_1' s_2'} \left\langle V_{s_1 s_2 s_2' s_1'}(\hat{\boldsymbol{k}}, \hat{\boldsymbol{k}}') f_{s_1' s_2'}(\hat{k}', \boldsymbol{R}; i\omega_n) \right\rangle_{\hat{\boldsymbol{k}}'}, \tag{F.11}$$

where a Fermi surface average $\int \frac{d\boldsymbol{\Omega}_{\boldsymbol{k}}'}{4\pi} = \langle \cdots \rangle_{\hat{\boldsymbol{k}}'}$.

F.2 Pairing interaction

We start with the following pairing interaction [28]:

$$V_{s_1 s_2 s_2' s_1'} = \frac{V}{2}\left[e_{\mathrm{s}} \hat{\tau}_{s_1 s_2} \hat{\tau}_{s_2' s_1'}^\dagger + e_{\mathrm{t}}\left\{ (\boldsymbol{g}_{\boldsymbol{k}} \cdot \hat{\boldsymbol{\tau}})_{s_1 s_2} (\boldsymbol{g}_{\boldsymbol{k}'} \cdot \hat{\boldsymbol{\tau}})_{s_2' s_1'}^\dagger \right\} \right.$$

$$\left. + e_{\mathrm{m}}\left\{ (\boldsymbol{g}_{\boldsymbol{k}} \cdot \hat{\boldsymbol{\tau}})_{s_1 s_2} \hat{\tau}_{s_2' s_1'}^\dagger + \hat{\tau}_{s_1 s_2} (\boldsymbol{g}_{\boldsymbol{k}'} \cdot \hat{\boldsymbol{\tau}})_{s_2' s_1'}^\dagger \right\} \right], \tag{F.12}$$

where $\hat{\tau}_{s_1 s_2} = (i\hat{\sigma}_y)_{s_1 s_2}$ and $\hat{\boldsymbol{\tau}}_{s_1 s_2} = (\boldsymbol{\sigma} i\hat{\sigma}_y)_{s_1 s_2}$. We set $V > 0$ and $e_{\mathrm{s}}^2 + e_{\mathrm{t}}^2 + e_{\mathrm{m}}^2 = 1$. Note that

$$V_{s_1 s_2 s_2' s_1'}(\boldsymbol{k}, \boldsymbol{k}') = \hat{\tau}_{s_1 s_2}\left[\frac{V}{2} e_{\mathrm{s}} \hat{\tau}_{s_2' s_1'}^\dagger + \frac{V}{2} e_{\mathrm{m}} (\boldsymbol{g}_{\boldsymbol{k}'} \cdot \hat{\boldsymbol{\tau}})_{s_2' s_1'}^\dagger \right]$$

$$+ (\boldsymbol{g}_{\boldsymbol{k}} \cdot \hat{\boldsymbol{\tau}})_{s_1 s_2}\left[\frac{V}{2} e_{\mathrm{t}} (\boldsymbol{g}_{\boldsymbol{k}'} \cdot \hat{\boldsymbol{\tau}})_{s_2' s_1'}^\dagger + \frac{V}{2} e_{\mathrm{m}} \hat{\tau}_{s_2' s_1'}^\dagger \right]. \tag{F.13}$$

Then, the gap equation becomes

$$
\Delta_{s_1 s_2}(\hat{\boldsymbol{k}}, \boldsymbol{R}) = \hat{\tau}_{s_1 s_2}\left[-\pi T N_{\mathrm{F}}\frac{V}{2}e_{\mathrm{s}}\sum_n \sum_{s_1' s_2'} \left\langle \hat{\tau}_{s_2' s_1'}^{\dagger} f_{s_1' s_2'}(\hat{\boldsymbol{k}}', \boldsymbol{R}; i\omega_n) \right\rangle_{\hat{\boldsymbol{k}}'} \right.
$$

$$
\left. -\pi T N_{\mathrm{F}}\frac{V}{2}\sqrt{\frac{3}{2}}e_{\mathrm{m}}\sum_n \sum_{s_1' s_2'} \left\langle (\bar{\boldsymbol{g}}_{\boldsymbol{k}'}\cdot\hat{\boldsymbol{\tau}})_{s_2' s_1'}^{\dagger} f_{s_1' s_2'}(\hat{\boldsymbol{k}}', \boldsymbol{R}; i\omega_n) \right\rangle_{\hat{\boldsymbol{k}}'} \right]
$$

$$
+ (\bar{\boldsymbol{g}}_{\boldsymbol{k}}\cdot\hat{\boldsymbol{\tau}})_{s_1 s_2}\left[-\pi T N_{\mathrm{F}}\frac{V}{2}\frac{3}{2}e_{\mathrm{t}}\sum_n \sum_{s_1' s_2'} \left\langle (\bar{\boldsymbol{g}}_{\boldsymbol{k}'}\cdot\hat{\boldsymbol{\tau}})_{s_2' s_1'}^{\dagger} f_{s_1' s_2'}(\hat{\boldsymbol{k}}', \boldsymbol{R}; i\omega_n) \right\rangle_{\boldsymbol{k}'} \right.
$$

$$
\left. -\pi T N_{\mathrm{F}}\frac{V}{2}\sqrt{\frac{3}{2}}e_{\mathrm{m}}\sum_n \sum_{s_1' s_2'} \left\langle \hat{\tau}_{s_2' s_1'}^{\dagger} f_{s_1' s_2'}(\hat{\boldsymbol{k}}', \boldsymbol{R}; i\omega_n) \right\rangle_{\boldsymbol{k}'} \right] \tag{F.14}
$$

where $\boldsymbol{g}_{\boldsymbol{k}} = \sqrt{3/2}(-\tilde{k}_y, \tilde{k}_x, 0) = \sqrt{3/2}\bar{\boldsymbol{g}}_{\boldsymbol{k}}$. We assume the following parity mixing form of the pair potential:

$$
\Delta_{s_1 s_2}(\hat{\boldsymbol{k}}, \boldsymbol{R}) = \hat{\tau}_{s_1 s_2}\Psi(\boldsymbol{R}) + (\bar{\boldsymbol{g}}_{\boldsymbol{k}}\cdot\hat{\boldsymbol{\tau}})_{s_1 s_2}\Delta(\boldsymbol{R}) \tag{F.15}
$$

Finally, we obtain the two gap equation.

$$
\Psi(\boldsymbol{R}) = g_{\mathrm{s}}\pi T\frac{1}{2}\sum_n \sum_{s_1' s_2'} \hat{\tau}_{s_2' s_1'}^{\dagger} \left\langle f_{s_1' s_2'}(\hat{\boldsymbol{k}}', \boldsymbol{R}; i\omega_n) \right\rangle_{\hat{\boldsymbol{k}}'}
$$

$$
- g_{\mathrm{m}}\pi T\frac{1}{2}\sum_n \sum_{s_1' s_2'} \left\langle (\bar{\boldsymbol{g}}_{\boldsymbol{k}'}\cdot\hat{\boldsymbol{\tau}})_{s_2' s_1'}^{\dagger} f_{s_1' s_2'}(\hat{\boldsymbol{k}}', \boldsymbol{R}; i\omega_n) \right\rangle_{\hat{\boldsymbol{k}}'}, \tag{F.16}
$$

$$
\Delta(\boldsymbol{R}) = g_{\mathrm{t}}\pi T\frac{1}{2}\sum_n \sum_{s_1' s_2'} \left\langle (\bar{\boldsymbol{g}}_{\boldsymbol{k}'}\cdot\hat{\boldsymbol{\tau}})_{s_2' s_1'}^{\dagger} f_{s_1' s_2'}(\hat{\boldsymbol{k}}', \boldsymbol{R}; i\omega_n) \right\rangle_{\boldsymbol{k}'}
$$

$$
- g_{\mathrm{m}}\pi T\frac{1}{2}\sum_n \sum_{s_1' s_2'} \hat{\tau}_{s_2' s_1'}^{\dagger} \left\langle f_{s_1' s_2'}(\hat{\boldsymbol{k}}', \boldsymbol{R}; i\omega_n) \right\rangle_{\boldsymbol{k}'}, \tag{F.17}
$$

where we define the coupling constant as follows: $g_{\mathrm{s}} \equiv -e_{\mathrm{s}}N_{\mathrm{F}}V$, $g_{\mathrm{m}} \equiv \sqrt{3/2}e_{\mathrm{m}}N_{\mathrm{F}}V$, $g_{\mathrm{t}} \equiv -(3/2)e_{\mathrm{t}}N_{\mathrm{F}}V$.